



UNIVERSIDADE FEDERAL DE SANTA CATARINA
CENTRO TECNOLÓGICO
PROGRAMA DE PÓS-GRADUAÇÃO EM ENGENHARIA MECÂNICA

Luiz Delagnelo Barbeta

**Application of the High-Current Spray Transfer Buried Arc in Hybrid Laser-Arc
Welding**

Florianópolis

2019

Luiz Delagnelo Barbetta

**Application of the High-Current Spray Transfer Buried Arc in Hybrid Laser-Arc
Welding**

Tese submetida ao Programa de Pós-Graduação em Engenharia Mecânica
da Universidade Federal de Santa Catarina para a obtenção do Grau de
Doutor em Engenharia Mecânica.

Orientador: Prof. Dr.-Ing. Walter Lindolfo Weingaertner

Coorientador: Prof. Regis Henrique Gonçalves e Silva, Dr. Eng.

Florianópolis
2019

Ficha de identificação da obra elaborada pelo autor,
através do Programa de Geração Automática da Biblioteca Universitária da UFSC.

Barbetta, Luiz

Application of the High-Current Spray Transfer Buried
Arc in Hybrid Laser-Arc Welding / Luiz Barbetta ;
orientador, Walter Weingaertner, coorientador, Regis
Silva, 2019.

146 p.

Tese (doutorado) - Universidade Federal de Santa
Catarina, Centro Tecnológico, Programa de Pós-Graduação em
Engenharia Mecânica, Florianópolis, 2019.

Inclui referências.

1. Engenharia Mecânica. 2. Soldagem Híbrida Laser-Arco.
3. Arco Enterrado. 4. Alta Corrente. 5. GMAW. I.
Weingaertner, Walter. II. Silva, Regis. III. Universidade
Federal de Santa Catarina. Programa de Pós-Graduação em
Engenharia Mecânica. IV. Título.

Luiz Delagnelo Barbeta

**Application of the High-Current Spray Transfer Buried Arc c in Hybrid Laser Arc
Welding**

O presente trabalho em nível de doutorado foi avaliado e aprovado por banca examinadora composta pelos seguintes membros:

Prof. Louriel Oliveira Vilarinho, Dr. Eng.
Universidade Federal de Uberlândia

Prof. Mateus Barancelli Schwedersky, Dr. Eng.
Universidade Federal de Santa Catarina

Prof. Carlos Enrique Niño Bohórquez, Dr. Eng.
Universidade Federal de Santa Catarina

Certificamos que esta é a **versão original e final** do trabalho de conclusão que foi julgado adequado para obtenção do título de doutor em Engenharia Mecânica.

Prof. Jonny Carlos da Silva, Dr. Eng.
Coordenador do Programa

Prof. Dr.-Ing. Walter Lindolfo Weingaertner
Orientador

Florianópolis, 2019.

Este trabalho é dedicado à minha família.

AGRADECIMENTOS

Agradeço ao professor Walter Lindolfo Weingaertner e ao professor Regis Henrique Gonçalves e Silva pela orientação neste trabalho e na maior parte da minha vida acadêmica.

Sou grato à Universidade Federal de Santa Catarina pela excelente formação que tive, desde a graduação até o doutorado.

Meus agradecimentos à Coordenação de Aperfeiçoamento de Pessoal de Nível Superior (CAPES) pelo financiamento na forma de bolsa durante o curso de doutorado.

Agradeço ao Instituto SENAI de Inovação em Sistemas de Manufatura e Processamento a Laser por disponibilizar a infraestrutura necessária para a execução dos experimentos e por acreditar em meu trabalho.

Agradeço a toda a equipe envolvida na realização deste trabalho, em especial à Natália Wendt Dreveck, ao Oberdan Vinícius Theves de Castro e ao Marcos Pereira Campos. Nenhum trabalho é feito sozinho e um bom trabalho depende de uma boa equipe.

Não há universidade capaz de formar um bom profissional se este não trazer uma boa educação na bagagem, por isso, sou extremamente grato à minha família, que sempre me forneceu um ambiente de amor, carinho e aprendizagem.

Agradeço também à pessoa que mais me ajudou e me aguentou durante esse desafio que é o doutorado, minha esposa, Paola Bez Goulart Barbeta. Sou muito grato por todo seu companheirismo, carinho, amor e suporte.

Por fim, gostaria de agradecer também a todos os meus amigos que me acompanharam ao longo da vida. Uma vida sem amizades é uma vida vazia.

RESUMO

A condição de arco enterrado utilizada em algumas variantes recentes do processo GMAW é caracterizada pela formação de uma acentuada depressão na superfície da poça fundida, dentro da qual se encontra a maior parte do comprimento do arco elétrico. Soldagem sob esta condição possui algumas vantagens, como aumento da penetração, redução de respingos, regularidade a maiores velocidades de soldagem e soldabilidade de juntas mais estreitas. O arco enterrado pode ser aplicado com os modos de transferência metálica globular, curto-circuito (forçado), pulsado e goticular. Quando aplicado na soldagem híbrida laser-arco (HLAW), a profunda depressão da poça reduz a espessura efetiva da chapa a ser penetrada pelo feixe laser, permitindo o uso de fontes laser de menor potência e mais baratas ou, reciprocamente, realizar soldagem mais profunda ou veloz com a mesma potência do feixe laser. Apesar dessa vantagem, a aplicação do arco enterrado no HLAW foi pouco estudada, especialmente no modo de transferência goticular, que pode permitir maiores correntes e poças de fusão mais estáveis, potencializando o efeito do arco enterrado. O presente trabalho estudou a aplicabilidade do arco enterrado com transferência goticular de alta corrente no HLAW, encontrando claros ganhos de penetração quando comparado com o processo em condições mais convencionais. Foram observadas outras possíveis vantagens que o HLAW nessa condição pode propiciar, principalmente relacionadas com o perfil da seção transversal da solda, que apresentou um “formato de V”, diferente do “formato de taça” da condição convencional do processo. Algumas dificuldades no trabalho com o HLAW de alta corrente com transferência goticular e arco enterrado foram encontradas, notadamente a tendência à formação de *humping* com a tocha na posição puxando e de um fenômeno de acúmulo de material à frente da poça de fusão com a tocha empurrando. Apesar dessas, foram obtidos bons cordões na soldagem de juntas de topo com preparo em V no aço ASTM A709 HPS 70W com 9,5 mm de espessura com velocidade de soldagem de 1,5 m/min.

Palavras-chave: soldagem híbrida laser-arco, arco enterrado, alta corrente, GMAW, MIG/MAG.

RESUMO EXPANDIDO

Introdução

Na soldagem híbrida laser-arco (HLAW), a profunda depressão na superfície da poça fundida formada pelo arco enterrado permite o aumento da penetração da solda, ou, reciprocamente, a redução da potência do feixe laser ou o aumento da velocidade de soldagem (GOOK; GUMENYUK; RETHMEIER, 2014; PAN et al., 2016a; WAHBA; MIZUTANI; KATAYAMA, 2015). A redução do requisito de potência do laser para uma mesma aplicação pode reduzir o custo de aquisição de um sistema de soldagem HLAW, tornando o processo mais atrativo para a indústria. As características do arco enterrado podem trazer também outras vantagens, como menor tendência à formação de trincas de solidificação, melhor diluição do metal de adição no interior da solda, maior taxa de deposição de material e menor tendência à formação de *humping* de raiz.

Apesar das possíveis vantagens, o HLAW com arco enterrado ainda foi pouco estudado na literatura, com poucos exemplos de soldagem com transferência globular ou pulsada (GOOK; GUMENYUK; RETHMEIER, 2014; PAN et al., 2016a; WAHBA; MIZUTANI; KATAYAMA, 2015). A transferência goticular, que pode permitir o uso de correntes médias mais elevadas e maior estabilidade da poça fundida, ainda não foi estudada no HLAW com arco enterrado.

Objetivos

Este trabalho avaliará a aplicação do GMAW com arco enterrado e alta corrente no HLAW, estudando os possíveis ganhos e dificuldades do processo. O primeiro objetivo do presente trabalho é adequar o GMAW com transferência goticular e arco enterrado com alta corrente para hibridização com o laser. O segundo é verificar se o GMAW goticular enterrado se mantém estável com a adição de um feixe laser ao processo. Estudar a interação entre as duas fontes de calor na condição de arco enterrado com transferência goticular é o terceiro objetivo do trabalho. Por fim, será avaliado o potencial de aplicação da soldagem HLA goticular enterrado com alta corrente, considerando-se os ganhos de penetração, outros possíveis pontos positivos e as dificuldades.

Metodologia

O trabalho foi desenvolvido utilizando-se uma fonte laser de disco Trumpf TruDisk 10002 com 10 kW de potência máxima e feixe com 600 μm de diâmetro focal e uma fonte de soldagem IMC Digiplus A7 multi-processos transistorizada operando como fonte de tensão constante. As soldas foram monitoradas utilizando-se um sistema de filmagem de alta velocidade com 20.000 quadros por segundo e com aquisição de corrente e de tensão instantâneos pela própria fonte de soldagem.

Utilizaram-se cordões sobre chapa de aço SAE 1020 com 16 mm de espessura para as três primeiras etapas e soldagem em junta V em aço A709 HPS 70W com 9,5 mm de espessura para a última etapa. A junta V foi usinada com nariz de 2 mm de altura, ângulo do bisel de 6° de inclinação e abertura de raiz de 0,2 mm. AWS A5.18 ER 70S-6 com 1,2 mm de diâmetro foi usado como metal de adição e a proteção gasosa se deu com Ar+18 % CO₂ a 20 l/min.

A primeira etapa do trabalho foi adequar o GMAW goticular enterrado com alta corrente para hibridização com o laser. A tocha foi inclinada 40° para a frente (puxando) e para trás (empurrando) para permitir a passagem do feixe laser na perpendicular e elevadas velocidades de soldagem (1,0; 1,5 e 2,0 m/min) foram utilizadas. Foram encontrados parâmetros de soldagem para o GMAW goticular enterrado com alta corrente e para o GMAW goticular arco longo com alta corrente para ambas as posições da tocha.

Na segunda etapa, as condições desenvolvidas na etapa anterior foram reproduzidas sem e com a presença do feixe laser (10 kW), fazendo-se ajustes se necessário.

Comparou-se a penetração do HLAW com arco enterrado goticular, do HLAW com arco longo e alta corrente e do HLAW convencional variando-se o posicionamento relativo entre as fontes de calor na terceira etapa. A distância entre laser e arco (D_{LA}) foi variada de -1 a 6 mm e a posição do foco de -8 a 2 mm. Esses ensaios foram restritos à velocidade de soldagem de 1,5 m/min e foi utilizada a metodologia de superfície de resposta com planejamento composto central para planejamento e análise dos experimentos.

A quarta etapa consistiu em trazer o processo desenvolvido nas etapas anteriores a um exemplo de aplicação industrial, no aço A709 HPS 70W. Foram feitos, inicialmente, ensaios de cordão sobre chapa para encontrar a potência do laser necessária para atingir a penetração total da chapa. Essa potência foi então utilizada para soldar a junta Y e o perfil do cordão foi analisado.

Resultados e Discussão

Foi possível obter o GMAW com arco enterrado e transferência goticular nas condições definidas para hibridização. Os parâmetros desenvolvidos para as posições puxando e empurrando com arco enterrado e longo são apresentadas na tabela abaixo. Ausência ou pequena quantidade de instabilidades foi observada para a maior parte das condições, mas percebeu-se maior ocorrência para a condição empurrando enterrado com 2 m/min. Na tabela, U é a tensão, V_w é a taxa de alimentação do arame, $DBCP$ é a distância bico de contato-peça e θ é o ângulo de inclinação da tocha em relação à normal.

Tocha	Arco	U (V)	V_w (m/min)	$DBCP$ (mm)	θ
Puxando	Enterrado	35	18	15	40°
	Longo	40	14	15	40°
Empurrando	Enterrado	37	18	15	-40°
	Longo	42	14	15	-40°

Os cordões feitos com o arco puxando enterrado apresentaram *humping* com morfologia de cilindro com contas (BCM de acordo com Soderstrom e Eagar (2006)) para velocidade de 1,5 e 2,0 m/min. O arco puxando longo resultou em *humping* com morfologia de região de goivagem (GRM de acordo com Soderstrom e Eagar (2006)) e cordões divididos para todas as velocidades. No GMAW com arco empurrando enterrado, notou-se um acúmulo de material na região à frente da poça fundida, ao qual deu-se o nome de acúmulo frontal, que é formado pelo fluxo frontal de material na região de goivagem por conta do jato de plasma do arco. O jato de plasma frontal com maior intensidade na condição empurrando com arco longo levou à formação de respingos.

Ao adicionar-se o feixe laser ao processo, observou-se a redução da tendência à formação de *humping* BCM, principalmente no caso de D_{LA} com 5 mm ou mais. Esse fenômeno foi atribuído à poça de fusão mais profunda onde normalmente haveria um estrangulamento da mesma, permitindo a recirculação do fluxo para trás em alta velocidade de material causado pelo jato de plasma. A recirculação desse fluxo traseiro também foi considerada a causa da supressão do *humping* GRM e dos cordões divididos no arco puxando longo.

O feixe laser ajudou também a suprimir a formação do acúmulo frontal para a soldagem com arco empurrando enterrado para D_{LA} de 5 e 6 mm, possivelmente por permitir que o fluxo frontal de material pudesse recircular para o interior da peça através da profunda poça de fusão formada pelo laser. Para distâncias menores, entretanto, o acúmulo se mostrou maior no HLAW do que no GMAW e foi observado que o mesmo cruza o caminho do feixe laser durante a solda, reduzindo consideravelmente a penetração nesses eventos, de forma aleatória.

Não se observou influência significativa do laser no arco elétrico, sem variação significativa de corrente e tensão entre o GMAW e o HLAW. Todavia, as instabilidades (possivelmente curto-circuitos) foram suprimidas na soldagem com tocha empurrando e arco enterrado, enquanto oscilações cíclicas da tensão foram percebidas quando da utilização do processo híbrido.

A penetração (*PD*) obtida pelo HLAW convencional ($I = 250$ A; $V_w = 8.0$ m/min), pelo HLAW empurrando com arco enterrado, pelo HLAW puxando com arco enterrado e pelo HLAW puxando com arco longo em suas condições de posicionamento aproximadamente ótimas estão presentes na tabela a seguir, juntamente com o desvio padrão dos quatro ensaios efetuados para cada uma dessas condições.

Condição de Soldagem	<i>PD</i> Média (mm)	σ <i>PD</i> (mm)
Convencional	8,62	0,65
Empurrando Enterrado	10,55	1,80
Puxando Enterrado	12,37	0,25
Puxando Longo	11,27	0,91

Comparando as condições por meio do Teste-T entre Duas Amostras de Welch (MONTGOMERY, 2013) podem-se chegar às seguintes conclusões:

- Ambos o HLAW puxando com arco enterrado e com arco longo resultam em cordões significativamente mais profundos do que o HLAW convencional, com grau de confiança de 99,95 % e de 99,58 % respectivamente. Isso indica que o aumento da corrente de 250 A para 470 A leva ao aumento da penetração.
- Na soldagem HLAW com alta corrente e tocha puxando, há uma grande probabilidade (90,93 %) de o arco enterrado atingir penetração ainda maior do que o arco longo.
- Nenhuma conclusão pode ser tirada do processo HLAW empurrando com arco enterrado devido à sua grande variabilidade.

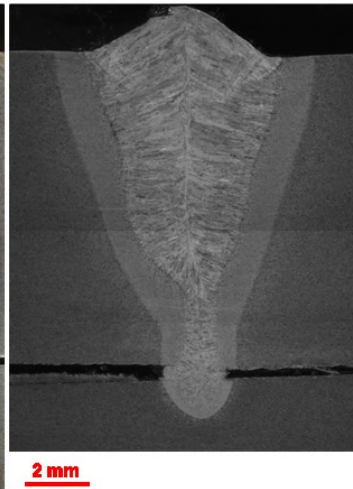
Na soldagem das chapas de A709 HPS 70W, foi necessário o uso de apenas 4,8 kW para atingir a penetração total dos 9,5 mm com o HLAW puxando com arco enterrado, enquanto a soldagem HLAW convencional (250 A) precisou de 7,7 kW, demonstrando a possibilidade de uso de lasers de menores potências e mais baratos para o processo desenvolvido. Na junta, a mordedura e o *humping*, que eram observados no HLAW enterrado, não ocorreram, resultando em um cordão livre de descontinuidades.

Uma outra vantagem observada foi o perfil do cordão, com 6,9 mm de penetração da zona do arco no HLAW enterrado contra 2,4 mm no HLAW convencional, como pode ser visto na figura abaixo. Dessa forma, espera-se que o HLAW enterrado resulte em melhor distribuição do metal de adição ao longo da profundidade da solda. A geometria em “V” do cordão é benéfica também do ponto de vista de trincas de solidificação, evitando-se a região de solidificação tardia no interior do cordão, podendo ser observado um caso de trinca de solidificação na solda HLAW convencional. Entre as possíveis vantagens, podem ser incluídos também a alta taxa de deposição de material, permitindo o preenchimento de juntas de maior volume, e a provável menor propensão ao *humping* de raiz, pelo fato de a espessura efetiva da chapa ser menor para o laser.

HLAW convencional



HLAW puxando enterrado



Considerações Finais

Demonstrou-se neste trabalho a viabilidade de aplicação do arco enterrado com transferência goticular na soldagem HLAW, com provável ganho de penetração, redução de potência (custo) do laser e/ou ganho de velocidade de soldagem. O processo se mostrou estável com a tocha na posição puxando e cordões de qualidade e com alta penetração da zona do arco foram produzidos.

ABSTRACT

The buried arc condition used in some GMAW process variants is characterized by a steep molten pool surface depression, within which most of the electric arc length can be found. Welding under this condition has some advantages, such as increased penetration, reduced spatter, regularity at higher welding speeds and welding of narrower grooves, and it can be applied for globular, (forced) short-circuiting, pulsed and spray transfer modes. When applied to Hybrid Laser-Arc Welding (HLAW), the deep pool depression decreases the effective plate thickness to be penetrated by the laser beam, allowing lower power cheaper laser sources to be used or, conversely, to perform deeper or faster welds with the same laser power output. Despite this advantage, the application of the buried arc in HLAW has been poorly studied, especially in the spray transfer mode, which would allow higher currents and a more stable molten pool, improving the buried arc effect. The present work has studied the applicability of the high-current spray transfer buried arc in HLAW, finding clear penetration gains when compared to the same process under more typical conditions. Other possible advantages for the HLAW in the studied condition were also observed, mainly related to the weld cross-section profile, which presented a V-shape instead of the typical wine cup shape. Some difficulties when working with the high current spray transfer buried arc HLAW were also found, notably the humping formation tendency with pulling torch and the buildup of material ahead of the molten pool with pushing torch. Despite these, good welds were obtained in V butt joints on 9.5 mm thick ASTM A709 HPS 70W steel plates at 1.5 m/min welding speed.

Keywords: hybrid laser-arc welding, buried arc, high-current, GMAW, MIG/MAG.

LIST OF FIGURES

Figure 1.1: HLAW application in shipbuilding.....	23
Figure 2.1: Disk laser working concept.....	27
Figure 2.2: LBW transitioning from conduction mode (a) and (b) to penetration mode (d)....	30
Figure 2.3: Depth of penetration as a function of welding speed and laser power.	31
Figure 2.4: Reduced penetration due to a too narrow beam.....	32
Figure 2.5: Examples of Hermite- and Laguerre-Gaussian modes.	35
Figure 2.6: TEM modes ranging from pure Hermite-Gaussian to pure Laguerre-Gaussian....	35
Figure 2.7: Interference fringes on a laser focal spot.	36
Figure 2.8: Actual beam compared to a theoretical diffraction limited beam.....	37
Figure 2.9: BPP and M^2 comparison for different laser sources.	38
Figure 2.10: Typical power and beam quality in different laser material processes and the evolution of diode lasers.....	39
Figure 2.11: Absorption of aluminum calculated by Drude theory and experimental data.	40
Figure 2.12: Plume and smoke during high power fiber LBW (a) and the collected particles observed through a TEM (b).	43
Figure 2.13: Spectral index of absorption for different metals and typical lasers wavelength.	44
Figure 2.14: Reflectivity behavior as a function of the angle of incidence for two different materials.	45
Figure 2.15: Observation of a buried arc in the SpeedArc process.	46
Figure 2.16: Radial distribution of plasma stagnation pressure and plasma shear stress.....	47
Figure 2.17: Pool depression development with increasing current in GTAW.....	48
Figure 2.18: The three penetration regions observed in GTAW.	49
Figure 2.19: Schematics of the gouging region observed in 500 A GTAW.	49
Figure 2.20: Arc force (a) and depth/width ratio (b) as functions of the current at different electrode positions in GTAW.....	51
Figure 2.21: GMAW processes classification according to DVS 0973 information sheet.	53
Figure 2.22: Welding of thick plates using the modified spray arc with narrower joint preparation (left) and conventional spray arc (right).....	54
Figure 2.23: Appropriate I/V ratio for buried arc.....	55
Figure 2.24: Alternated projected and rotating spray buried arc current and voltage evolution and high-speed imaging.....	55
Figure 2.25: Single pass GMAW of 19 mm thick ASTM A36 steel with alternated projected and rotating spray buried arc.	56
Figure 2.26: Hybrid laser-GMA welding of 10 mm thick API 5L X52 steel with 2 mm misalignment.	57
Figure 2.27: Arc zone and laser zone in a hybrid laser-GMA weld.....	58
Figure 2.28: Example of a coaxial HLAW head solution.	59
Figure 2.29: Arc impedance reduction and stabilization in HLAW.....	60
Figure 2.30: Arc anchoring effect in HLAW.	60
Figure 2.31: Ionization grade as a function of temperature for Al, Fe, Ar and He.	61
Figure 2.32: Weld penetration variation at different beam interaction points within the pool depression.....	62
Figure 2.33: Arc voltage reduction due to the optogalvanic effect as a function of laser wavelength.....	65
Figure 2.34: Multiphoton ionization guiding electric arcs in different beam configuration. ...	66
Figure 2.35: Plasma in short-circuiting GMAW (a) and HLAW (b).	67
Figure 2.36: Electromagnetic force in short-circuiting GMAW (a, b and c) and in HLAW (d, e and f).....	67

Figure 2.37: Electromagnetic force in globular GMAW (a, b and c) and in HLAW (d, e and f).	68
Figure 2.38: Molten pool shape and flow for (a) 304L stainless steel, (b) Ti-6Al-4V, (c) vanadium and (d) tantalum.	70
Figure 2.39: Fluid flow in fully penetrating welds (a) and necking and bulging regions on the pool (b).	70
Figure 2.40: Pool behavior inside the vapor capillary.	71
Figure 2.41: Capillary front wall downward flow speed at different positions.	71
Figure 2.42: Driving forces in HLAW for arc leading (a) and laser leading (b) with 2 % O ₂ content in shielding gas.	72
Figure 2.43: Schematics of LBW most common defects.	73
Figure 2.44: Humping and undercut critical speeds for different welding currents.	74
Figure 2.45: Examples of BCM humping.	75
Figure 2.46: Numerical simulated hump formation due to backward flow.	76
Figure 2.47: Examples of GRM humping, tunnel porosity and parallel humping.	77
Figure 2.48: Solidified gouging region leading to hump formation.	78
Figure 2.49: Undercutting in high-speed LBW.	79
Figure 2.50: Solidification sequence in LBW with a bulging region.	81
Figure 3.1: Laser processing machine SL8600 from Preco Inc.	83
Figure 3.2: Process arrangement and positioning variables.	84
Figure 3.3: a) Joint preparation; b) Plate dimensions.	86
Figure 3.4: Arc length measurement	89
Figure 3.5: Plasma jets speed and inclination measurement.	90
Figure 3.6: Alternating GMAW and HLAW on a single bead.	91
Figure 4.1: Bead appearance for GMAW and HLAW.	98
Figure 4.2: Response surface for the pulling buried arc HLAW.	100
Figure 4.3: Response surface for the pulling long arc HLAW.	102
Figure 4.4: Response surface for the pushing buried arc HLAW.	104
Figure 4.5: Conventional spray HLAW and pulling buried spray HLAW macrographs.	106
Figure 5.1: Current and voltage oscillogram for pulling buried GMAW at three welding speeds.	108
Figure 5.2: Current and voltage oscillogram for pushing buried GMAW at three welding speeds.	109
Figure 5.3: High-speed imaging of a short-circuiting event.	109
Figure 5.4: Bead appearance for pulling buried spray arc GMAW.	110
Figure 5.5: Bead appearance for pulling long spray arc GMAW.	111
Figure 5.6: Cross section of a gouging region with three rims.	112
Figure 5.7: Bead appearance for pushing buried spray arc GMAW.	113
Figure 5.8: Bead appearance for pushing long spray arc GMAW.	113
Figure 5.9: Frontal buildup formation.	114
Figure 5.10: Frontal buildup at 1.5 m/min and 2.0 m/min for pushing buried arc.	114
Figure 5.11: Tracking of two droplets being ejected from the pool.	115
Figure 5.12: Stretched frontal buildup in the pushing long arc GMAW crater.	115
Figure 5.13: Average current as a function of laser-arc distance for the pushing buried, pulling buried and pulling long arc.	117
Figure 5.14: Current and voltage oscillogram for pushing buried arc GMAW and HLAW.	118
Figure 5.15: High-speed imaging of the pushing buried arc condition in GMAW (a) and in HLAW (b) showing metal transfer.	119
Figure 5.16: Bead appearance for pulling buried spray arc GMAW and HLAW at different D_{LA}	120

Figure 5.17: High speed imaging comparing GMAW to HLAW at 0 and 6 mm D_{LA}	120
Figure 5.18: Bead appearance for pulling long arc GMAW and HLAW at different welding speeds.	122
Figure 5.19: Bead appearance for pulling long arc GMAW and HLAW at different D_{LA}	122
Figure 5.20: Fluid flow in the gouging region for GMAW and HLAW with high-current long arc.	123
Figure 5.21: High-speed imaging frames for GMAW and HLAW at 1.5 m/min.	123
Figure 5.22: Frontal buildup under different welding conditions at 1.5 m/min welding speed.	124
Figure 5.23: Downward recirculation for pushing buried arc at long D_{LA}	125
Figure 5.24: High-speed imaging of a frontal buildup ejection and the resulting bead.	126
Figure 5.25: Penetration longitudinal profile for pushing buried (a), pulling buried (b) and pulling long (c) arcs at 2.5 mm D_{LA} and -3 mm f	126
Figure 5.26: Pushing long arc GMAW and HLAW spatter.	127

LIST OF TABLES

Table 2.1: Heat flux from different fusion welding processes.	29
Table 2.2: Weld penetration increase by decreasing voltage.	52
Table 3.1: Laser and optical system characteristics.	84
Table 3.2: High-speed imaging parameters.	85
Table 3.3: SAE 1020 steel composition.	85
Table 3.4: ASTM A709 HPS 70W composition.	85
Table 3.5: CCD points for D_{LA} and f	92
Table 3.6: CCD experiments order.	93
Table 4.1: Defined GMAW parameters.	95
Table 4.2: Summarized GMAW results.	96
Table 4.3: High-speed imaging measured arc characteristics.	96
Table 4.4: Average current, voltage and arc length for GMAW and HLAW.	97
Table 4.5: Conventional spray arc HLAW penetration depth.	99
Table 4.6: Natural and coded factors and response for the pulling buried arc HLAW.	99
Table 4.7: Average current, voltage and arc length for each pulling buried arc HLAW run.	101
Table 4.8: Natural and coded factors and response for the pulling long arc HLAW.	102
Table 4.9: Average current, voltage and arc length for each pulling long arc HLAW run.	103
Table 4.10: Natural and coded factors and response for the pushing buried arc HLAW.	104
Table 4.11: Average current, voltage and arc length for each pushing buried arc HLAW run.	105
Table 5.1: Pool depression and arc length at different welding speeds.	107
Table 5.2: Average current, voltage and arc length difference between HLAW and GMAW.	116
Table 5.3: Main arc properties.	118
Table 5.4: Mean and standard deviation of penetration depth for all four welding conditions reproductions at the central point.	128
Table 5.5: Results of each comparison pair.	128

LIST OF ABBREVIATIONS

LBW	Laser Beam Welding
HLAW	Hybrid Laser-Arc Welding
GMAW	Gas Metal Arc Welding
YAG	Yttrium Aluminum Garnet
EBW	Electron Beam Welding
HAZ	Heat Affected Zone
PAW	Plasma Arc Welding
TEM	Transverse Electromagnetic Mode
BPP	Beam Parameter Product
GTAW	Gas Tungsten Arc Welding
SAW	Submerged Arc Welding
GMAW	Gas Metal Buried Arc Welding
GRM	Gouging Region Morphology (Hum- ping)
BCM	Beaded Cylinder Morphology (Hum- ping)
CTWD	Contact-Tip-to-Work Distance
EDS	Energy-Dispersive X-Ray Spectros- copy

LIST OF SYMBOLS

Latin Alphabet:

A_R	[A/m ² K ²]	Richardson's constant
BPP	[mm.mrad]	Beam parameter product
$CTWD$	[mm]	Contact-tip-to-work distance
d_{min}	[mm]	Theoretical minimal beam diameter
D_L	[mm]	Beam width at the focusing lens
D_{LA}	[mm]	Laser-arc distance
e	[-]	Euler's number
f	[mm]	Focal position
F	[mm]	Focal distance
h	[m ² kg/s]	Planck's constant
I_m	[A]	Average current
k_B	[m ² kg/s ² K]	Boltzmann's constant
K_D	[-]	Current drop factor
K_S	[-]	Current rise factor
l	[-]	Number of angular nodes (Laguerre-Gaussian TEM)
L	[mm]	Arc length
m	[-]	Number of nodes in the vertical direction (Hermite-Gaussian TEM)
M^2	[-]	Beam quality factor
n	[-]	Number of nodes in the horizontal direction (Hermite-Gaussian TEM)
p	[-]	Number of radial nodes (Laguerre-Gaussian TEM)
P	[W]	Laser beam power
P_A	[W]	Average arc power
PD	[mm]	Penetration depth
PD_{max}	[mm]	Maximum penetration depth
P_F	[W/mm]	Power factor
q	[-]	Number of longitudinal nodes (Laguerre-Gaussian and Hermite-Gaussian TEM)
R_P	[-]	Reflectivity for the parallel component
R_S	[-]	Reflectivity for the perpendicular component
t_i	[s]	Interaction time
T	[K]	Temperature
U_m	[V]	Average voltage
v_B	[m/s]	Backward plasma jet speed
v_F	[m/s]	Forward plasma jet speed
V	[m/min]	Welding speed
V_w	[m/min]	Wire feed rate
w_0	[mm]	Beam waist width at focal position
W_e	[eV]	Work function

Greek Alphabet:

α_B	[°]	Backward plasma jet inclination
α_F	[°]	Forward plasma jet inclination
η	[-]	Index of refraction real part
θ	[°]	Torch inclination angle
Θ_{Actual}	[rad]	Divergence angle of an actual laser beam
Θ_{Gauss}	[rad]	Divergence angle of a theoretical diffraction limited laser beam with same origin as actual beam
Θ_R	[rad]	Divergence angle of a theoretical diffraction limited laser beam with the same initial beam waist as the actual beam
κ	[-]	Index of refraction imaginary part
λ	[μm]	Wavelength
σ	[-]	Standard deviation
ϕ	[rad]	Angle of incidence

SUMMARY

1	INTRODUCTION	23
1.1	OBJECTIVES	25
1.1.1	Main Objective.....	25
1.1.2	Specific Objectives	25
2	BIBLIOGRAPHIC REVIEW.....	27
2.1	LASER BEAM WELDING	27
2.1.1	Power, Speed and Beam Width	30
2.1.2	Laser Sources	33
2.1.3	Laser-Matter Interaction	39
2.2	BURIED ARC	45
2.2.1	Pool Depression	47
2.2.2	Buried Spray Arc GMAW	51
2.3	HYBRID LASER-GMA WELDING	56
2.3.1	Laser-Arc Interaction.....	59
2.3.1.1	<i>Metallic Vapors</i>	<i>61</i>
2.3.1.2	<i>Pool Depression.....</i>	<i>62</i>
2.3.1.3	<i>Arc Plasma Heating.....</i>	<i>63</i>
2.3.1.4	<i>Thermionic Emission</i>	<i>63</i>
2.3.1.5	<i>Pre-Heating</i>	<i>64</i>
2.3.1.6	<i>Optogalvanic Effect</i>	<i>64</i>
2.3.1.7	<i>Other Phenomena</i>	<i>65</i>
2.3.2	Metal Transfer in Hybrid Laser-GMA Welding	66
2.3.2.1	<i>Short-Circuit.....</i>	<i>66</i>
2.3.2.2	<i>Globular.....</i>	<i>68</i>
2.3.2.3	<i>Spray.....</i>	<i>68</i>
2.3.3	Pool Dynamics	69
2.3.4	Discontinuities and Defects	73
2.3.4.1	<i>Humping and Undercutting</i>	<i>74</i>
2.3.4.2	<i>Other Discontinuities.....</i>	<i>80</i>
2.3.5	Hybrid Laser-Buried Arc GMA Welding	81
3	METHODOLOGY	83
3.1	EQUIPMENT	83

3.2	MATERIALS	85
3.2.1	Base Metal	85
3.2.2	Filler Metal.....	86
3.2.3	Shielding Gas.....	87
3.3	METHODS	87
3.3.1	Buried Spray Arc GMAW Preparation	87
3.3.2	Application of the Buried Spray Arc in HLAW	90
3.3.3	Comparison between Buried and Conventional Arc HLAW	91
3.3.4	HPS 70W Steel Application Example	93
4	RESULTS	95
4.1	BURIED SPRAY ARC GMAW PREPARATION.....	95
4.2	APPLICATION OF THE BURIED SPRAY ARC IN HLAW	97
4.3	COMPARISON BETWEEN BURIED AND CONVENTIONAL ARC HLAW...	98
4.3.1	Conventional HLAW.....	98
4.3.2	Pulling Buried Arc HLAW	99
4.3.3	Pulling Long Arc HLAW	101
4.3.4	Pushing Buried Arc HLAW.....	103
4.4	HPS 70W STEEL APPLICATION EXAMPLE	105
5	DISCUSSION.....	107
5.1	BURIED SPRAY ARC GMAW	107
5.1.1	Buried Spray Arc Condition.....	107
5.1.1.1	<i>Arc Length</i>	<i>107</i>
5.1.1.2	<i>Metal Transfer</i>	<i>108</i>
5.1.2	Pulling and Pushing Configurations	110
5.1.2.1	<i>Pulling Torch.....</i>	<i>110</i>
5.1.2.2	<i>Pushing Torch.....</i>	<i>112</i>
5.2	LASER INTERACTIONS WITH A BURIED SPRAY ARC	115
5.2.1	Laser Effects on Arc Electric Properties	115
5.2.2	Laser Effects on Pool Flow and Discontinuities.....	119
5.2.2.1	<i>BCM Humping.....</i>	<i>119</i>
5.2.2.2	<i>Gouging Related Discontinuities.....</i>	<i>121</i>
5.2.2.3	<i>Frontal Buildup and Forward Spatter.....</i>	<i>124</i>
5.3	BURIED SPRAY ARC HLAW PROCESS	127
5.3.1	Penetration	127

5.3.2	Other Advantages	129
5.3.3	Discontinuities and Difficulties	130
6	CONCLUSIONS AND SUGGESTIONS FOR FUTURE WORKS	131
6.1	CONCLUSIONS	131
6.2	SUGGESTIONS FOR FUTURE WORKS	132
	REFERENCES	134

1 INTRODUCTION

Laser beam welding (LBW) is a highly productive process, which allows the joining of thick plates in a single high penetration pass at high welding speeds, producing narrow welds with reduced heat input. These advantages are due to the high focusability of laser light, allowing high amounts of heat to be delivered to a very small area. This characteristic allied to the limited applicability of filler metal brings one of the main disadvantages of the LBW process, its poor gap bridgeability and low tolerance to misalignment. This disadvantage limits LBW application for joining of thick plates, as the high precision requirement of the LBW are often-times economically and technically unreachable in industrial environment.

Hybridizing the LBW with a conventional arc welding process, most often gas metal arc welding (GMAW), alleviates this problem. The resulting hybrid laser-arc welding (HLAW) process is then more robust, being preferable for most heavy welding applications. For example, it has been successfully used in the shipbuilding industry for assembling ship blocks, as depicted in Figure 1.1.

Figure 1.1: HLAW application in shipbuilding.



Source: Meyer Werft GmbH

The HLAW process offers other advantages compared to LBW, including reduced porosity, reduced crack sensitivity and improved penetration. The latter is due to synergetic effects between both heat sources, including: metallic vapors generated inside the vapor capillary, pool depression induced by arc pressure, direct heating of the arc plasma, pre-heating of the work-piece and other phenomena (AKSELSEN; REN; AAS, 2014; BAGGER; OLSEN, 2005; KAH, 2012; RIBIC; PALMER; DEBROY, 2009).

Despite the HLAW good characteristics, its applications are still limited in the industry due to its high initial capital investment, especially due to the still expensive laser sources (KAH, 2012).

During the last three decades, new variants of the GMAW process were developed using high current levels (over 200 A) and very short arc length, in such a manner that most of the arc remains buried inside the pool surface depression, leading to welds with higher penetration. Different metal transfer modes can be applied with the buried arc, including spray, globular, pulsed and short-circuiting. Some examples of buried arc processes are: RapidArc, RapidMelt, ForceArc, ForceArc Puls, DeepArc, FocusArc, RapidWeld, SpeedArc and Focus Puls.

The increased pool depression provided by these processes could prove advantageous for HLAW. The deeper depression could reduce the effective plate thickness the laser beam has to penetrate, which might allow the usage of cheaper less powerful laser sources for welding the same thickness. Conversely, higher penetration or higher welding speed could be obtained for the same beam power, improving productivity.

Increased penetration might not be the only advantage in using a buried arc. The high filler metal feed rate typical of buried arc processes means bigger gaps and malalignments might be able to be welded properly. The filler metal is also delivered directly into a deeper part of the weld and the high electromagnetic forces might help to achieve a more homogeneous filler metal distribution along the weld depth, which is a common difficulty in HLAW of thick sections (CHEN et al., 2017; CHO et al., 2010; LIU; KUTSUNA; XU, 2006; ZHAO et al., 2009). It has been shown that increased arc-laser power ratio can reduce the incidence of solidification cracking (GEBHARDT; GUMENYUK; RETHMEIER, 2014), so the usage of the high power buried arc processes allied with a reduced laser power need might improve solidification cracking resistance. The weld shape might also result in a reduced solidification cracking tendency, since the necking and bulging areas, often associated with that discontinuity (ARTINOV et al., 2018; BAKIR et al., 2018; BARBETTA, 2014), could be overridden by the arc region. The reduction in laser power requirement and changes to the molten metal flow might also beneficially impact root humping formation.

Despite all the possible benefits, very little research has been done on the applicability and the effects of the buried arc in HLAW. The buried globular arc has been applied to HLAW by Wahba *et al.* (2015) and by Pan *et al.* (2016a), and the buried pulsed arc by Gook *et al.* (2014). However, no studies were found explicitly analyzing the effects of a buried spray arc on HLAW. The author believes that the spray transfer would be the most adequate for many applications, as higher average currents are attainable (over 400 A) and pool depression and metal transfer should be more constant and stable.

Applying the buried spray arc at high currents for HLAW might pose some difficulties, however. Firstly, in buried arc GMAW, the torch is usually held orthogonally to the welding

direction, so it is not clear how the process will behave when the torch is inclined to allow the laser beam passage. It is also not clear whether it should be inclined forwards (pulling) or backwards (pushing) and how that will affect the hybrid process.

Humping and undercutting are common problems when GMA welding with high currents and welding speeds (SODERSTROM; MENDEZ, 2006; WEI, 2010). Although HLAW is less prone to these discontinuities (ONO et al., 2002; SUGINO et al., 2005), no studies were found evaluating these discontinuities at so high currents.

Studying of the arc-laser interaction under such conditions (high current and high confinement) is also unprecedented, so it is even unknown how the heat sources will interact and if the buried arc will remain stable.

1.1 OBJECTIVES

1.1.1 Main Objective

The thesis of this work is that the hybrid process of LBW and buried spray arc GMAW is an advantageous process variant for industrial applications of HLAW. To demonstrate this thesis, it is necessary to determine a range of feasible process parameters and if there are economic advantages, in the form of increased penetration or weld quality. The interaction of both heat sources in a buried arc condition has to be evaluated, especially related to arc properties and to pool flow and the discontinuities linked to it.

1.1.2 Specific Objectives

- The buried spray arc GMAW process must be developed to a stable condition with tilted torch and higher welding speed in order to the hybridization with the LBW process to be feasible.
- Verify if the buried spray arc remains stable as the laser beam is added to the process and if any adjustments are needed to the arc parameters.

Analyze the laser-arc interactions regarding arc properties and molten pool dynamics related discontinuities at different heat sources arrangement.

- Establish a condition or a range of conditions where stable metal transfer, weld penetration and absence of discontinuities are attainable.
- Evaluate possible penetration gains or reduction of required laser power by employing a buried spray arc in place of conventional spray arc in HLAW.

- Apply the developed process in a possible industrial application and evaluate the bead quality and geometrical characteristics of the weld.

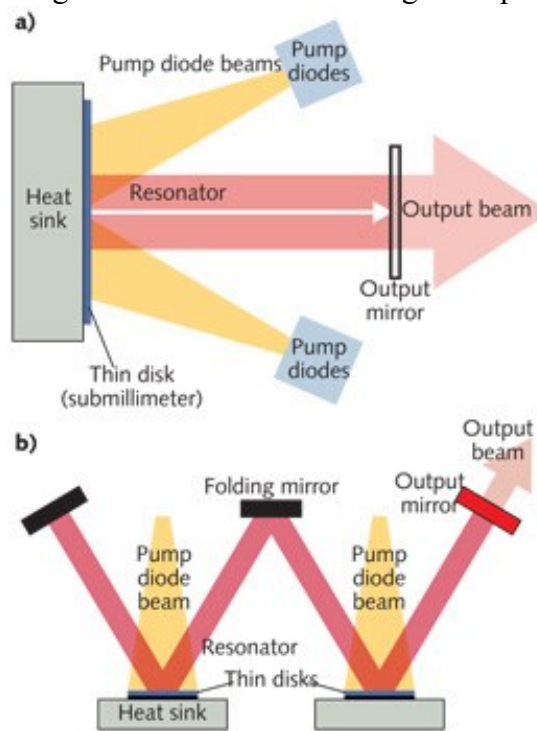
2 BIBLIOGRAPHIC REVIEW

In order to give a better understanding of the hybrid laser-buried arc GMA welding process, this chapter first disserts on the separated processes of laser beam welding (LBW) and buried arc GMAW. A subchapter about hybrid laser-arc welding (HLAW) follows. The little bibliography available about the hybrid laser-buried arc GMA welding process is also presented within that subchapter as well.

2.1 LASER BEAM WELDING

A laser is a machine capable of generating highly coherent and nearly monochromatic light and it is composed of three basic components: active medium, pumping source and resonator. The schematics in Figure 2.1 depict the working concept for single thin disk lasers (a) and multiple thin disks lasers (b), the later representing the laser used in the present work.

Figure 2.1: Disk laser working concept.



Source: LaserFocusWorld.

The active medium (or laser medium) is a material used for light amplification through the stimulated emission phenomenon, as described by Albert Einstein (EINSTEIN, 1916). The stimulated emission happens when a photon disturbs a specimen (atom, molecule, ion, etc.) in an excited state, causing it to emit a new photon in the same direction, phase and wavelength as the disturbing photon. If a medium has a gain higher than 1, that is, more photons are emitted

by stimulated emission than photons are lost by other effects (absorption, scattering, etc.), it can be used for light amplification and might be suitable for a laser (STEEN; MAZUMDER, 2010). In the case of disk lasers, the thin crystal disk is the active medium, which is usually composed of an yttrium aluminum garnet (YAG) crystal doped with ytterbium.

The purpose of a pumping source is to pump the active medium into an energetic state to keep the stimulated emission phenomenon going. In fact, population inversion (more specimens in an excited state than in ground state) is needed to keep the active medium gain above 1 for lasers. Typical pumping sources include flash lamps, diode lasers and electrons (STEEN; MAZUMDER, 2010). Most high-power solid-state lasers nowadays, including disk lasers, are pumped with diode lasers.

An optical resonator, usually composed of two mirrors, is used to reflect the light back and forth through the active medium, leading to repeated light amplifications in one direction. One of the mirrors is partially transparent to allow a small part of the light to leave the resonator and be used in a myriad of applications as a laser beam, including welding (STEEN; MAZUMDER, 2010).

Due to its high coherency and monochromatic quality, the laser beam is a very interesting heat source for fusion welding. Its main aspect is the ability to focus all its power into a very small area, resulting in heat fluxes¹ comparable to electron beam welding (EBW) and much higher than arc processes. It is also a very stable and controllable heat source. Table 2.1 shows a heat flux comparison for different welding heat sources.

When the intensity is on the lower side, be it due to low power or due to a too wide beam, the laser energy is absorbed by the material surface and the heat is transferred to the bulk material by conduction and convection (RAI et al., 2008). This results in a shallow weld with small aspect ratio. Welding in this condition is commonly called Conduction Mode (POPRAWA, 2011; STEEN; MAZUMDER, 2010).

LBW in the conduction mode is a very stable process with good heat input control that can easily result in high quality welds free of pores and spatter. Due to the relatively wider beam used in this mode, there are less fit-up problems and cheaper lasers with lower beam quality can be used (POPRAWA, 2011; QUINTINO; ASSUNÇÃO, 2013).

¹ Heat (or energy) flux is the quantity of heat (or energy) flowing through a surface (LIENHARD; LIENHARD, 2011). For a laser beam, the terms “intensity” and “irradiance” can also be used, where intensity is the energy flux through an imaginary orthogonal surface (a beam characteristic) and irradiance is the radiant energy flux to a real surface (ROHSENOW; HARTNETT; CHO, 1998). In this work, those nomenclatures will be preferred over “power density”, which is common in the welding literature.

Table 2.1: Heat flux from different fusion welding processes.

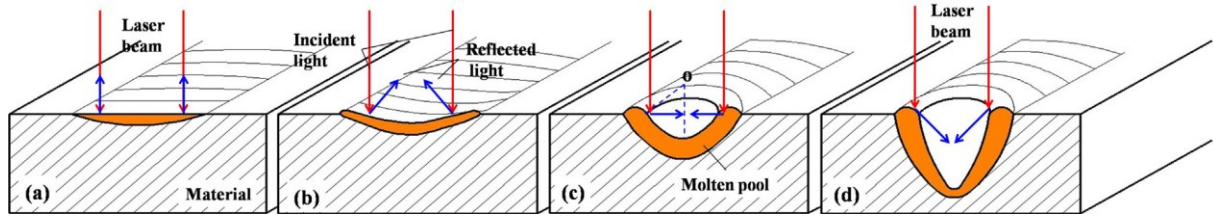
Process	Heat Flux (W/m ²)	Fusion Zone Profile
Shielded Metal Arc Welding	$5 \times 10^6 - 10^8$	
Gas Metal Arc Welding	$5 \times 10^6 - 10^8$	 low
		 high
Plasma Arc Welding	$5 \times 10^6 - 10^{10}$	 low
		 high
Laser and Electron Beam Welding	$1 \times 10^{10} - 10^{12}$	 defocus
		 focus

Adapted from: (STEEN; MAZUMDER, 2010).

If intensity is increased, vaporization becomes more prominent and the recoil pressure it exerts on the liquid surface rises. A deep and narrow depression on the surface develops after a threshold. What defines that threshold is still up to debate. It is common to consider it the point at which surface temperature reaches the vaporization temperature, but experiments have shown that even higher surface temperatures might be needed, because of the higher pressure found locally on the surface (HIRANO; FABBRO; MULLER, 2011). It is also not clear if irradiance is the governing parameter, as some authors have found better correlation between the threshold with the power to spot diameter ratio (or power factor) than with irradiance (ZOU et al., 2015). The deep and narrow depression is called a vapor capillary (POPRAWA, 2011) or a keyhole (STEEN; MAZUMDER, 2010).

As the depression develops, the laser beam reflection on the molten pool surface changes from an outward reflection under conduction mode (Figure 2.2 (a) and (b)) to an inward reflection when the vapor capillary has developed (Figure 2.2 (c) and (d)), leading to heat transport to the inside of the material and an increase to perceived absorptance (ZOU et al., 2015). Welding under this condition results in a high penetration and highly productive process with narrow heat affected zone (HAZ) and low thermal distortions, typically called Penetration Mode (POPRAWA, 2011) or Keyhole Mode (STEEN; MAZUMDER, 2010).

Figure 2.2: LBW transitioning from conduction mode (a) and (b) to penetration mode (d).



Source: (ZOU et al., 2015)

Since the penetration mode is by far the most prevalent LBW mode used in hybrid laser-arc welding, especially for thick welds, this work will focus on that mode from here on. Whenever laser welding is mentioned, the reader should consider it is referring to the penetration mode.

Regarding the nomenclature, “vapor capillary” and “penetration mode” will be preferred over “keyhole” and “keyhole mode” respectively in this work. Some authors (JARVIS, 2001; PORT et al., 2007) suggest avoiding the later terms, since “keyhole mode” is already used for different welding processes such as PAW or EBW when a through hole is created by welding forces (plasma pressure for PAW or evaporation pressure for LBW and EBW), which is not necessarily the case in LBW, since it is possible to obtain a vapor capillary without full penetration. That way, the depression caused by rapid evaporation will be called “vapor capillary” and welding with a vapor capillary will be called “penetration mode”. “Keyhole” and “keyhole mode” will be specifically used only when the vapor capillary is fully penetrating.

2.1.1 Power, Speed and Beam Width

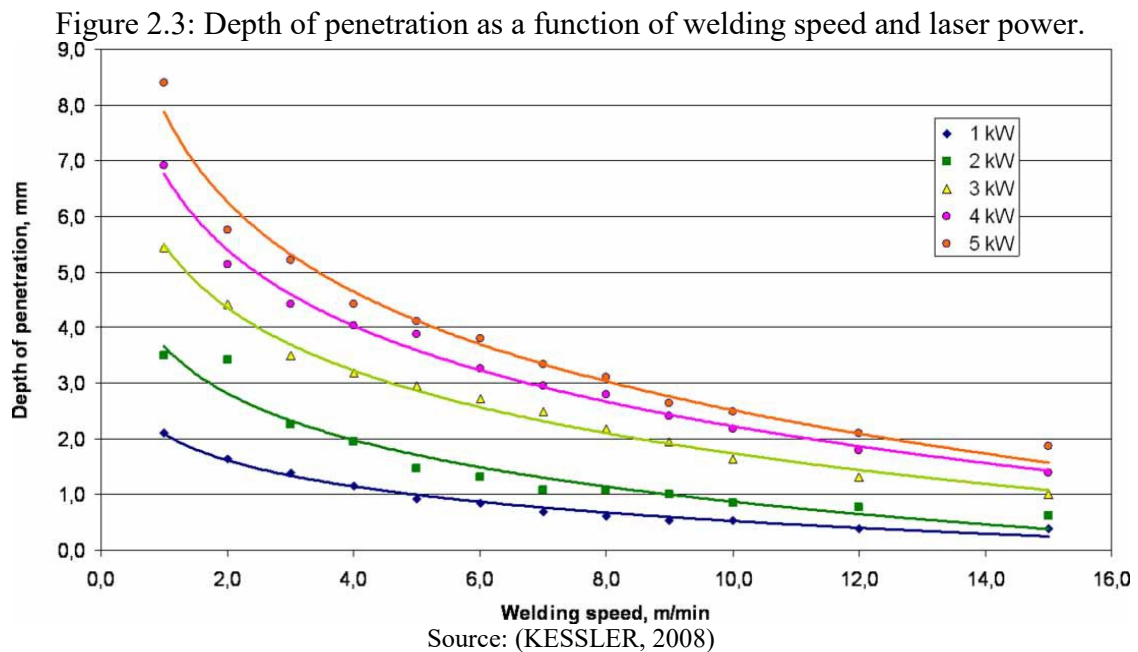
When welding in the penetration mode with a continuous wave laser, there are three main independent parameters that define the weld depth and width: laser beam power, travel speed and beam width. Understanding how each parameter affects the weld geometry is important to be able to predict results and to replicate welds under different machines (KIM; KI, 2014; SUDER; WILLIAMS, 2014).

Laser beam power, as can be expected, has a strong influence on the weld depth: The more powerful the laser, the deeper is the weld. Lienert (2011) presented the following Equation (2.1) for estimating the peak penetration (PD_{max}) of a laser weld, that is, how deep it is possible to reach with a given laser power (P) at very slow travel speeds:

$$PD_{max}(\text{mm}) \cong 2.5 \times 10^{-2} P^{0.7} \quad (2.1)$$

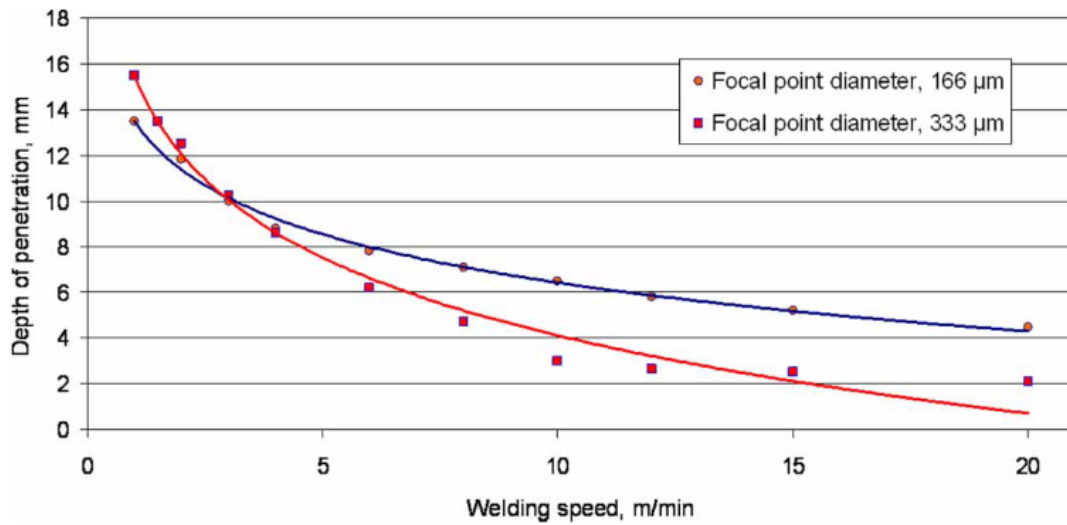
This equation is limited to a very rough estimate though, since it does not consider some important parameters, such as material properties, beam width and laser wavelength.

As the travel speed increases, the amount of energy delivered to each point of the weld (welding energy or line energy) is reduced, thus the weld becomes shallower. Figure 2.3 show the weld penetration behavior as a function of the welding speed at different power levels for fiber laser welding of mild steel (KESSLER, 2008).



The beam width affects the process by changing the beam intensity and the interaction time. A wider beam has reduced heat flux, since the same power is spread through a bigger area, and increased interaction time, as it takes longer for the beam to cross a single point at a given travel speed. Narrower beams lead to deeper welds, although it has been observed that, if the vapor capillary is too narrow at high penetrations, it may become unstable and thus loose penetration (KESSLER, 2008). Figure 2.4 shows that behavior, which can also be explained by stronger interaction of the laser beam with the plasma due to the increased intensity (SALMINEN; PIILI; PURTONEN, 2010).

Figure 2.4: Reduced penetration due to a too narrow beam.



Source: (KESSLER, 2008)

Heat flux, interaction time and welding energy are the three basic laser-material interaction parameters proposed by Suder and Williams (2012), which are related to beam power, travel speed and beam width. Those three basic parameters would define the interaction between laser light and material, while being easily transferrable between different machines with different optical configurations. It was observed that the welding depth is mainly controlled by heat flux and welding energy, while the weld width is controlled by the interaction time. On a later work, Suder and Williams (2014) observed that the weld depth is better correlated to the power factor (laser power per beam width) than to the heat flux. It is interesting to note that some authors also found the power factor to be a better threshold criterion between conduction and penetration modes (ZOU et al., 2015), as discussed previously.

Different authors tried to develop equations to predict the weld penetration under different conditions to avoid unnecessary testing and time-consuming numeric simulations. However, such a simple equation is yet to be developed and extensively tested. Ion *et al.* (1992), for example, created an equation based on a normalized beam power and the Peclet number. Hann *et al.* (2011) developed an empirical equation where a dimensionless depth, defined as the depth divided by the beam width, is a function of a dimensionless enthalpy, calculated as the maximal enthalpy in the weld divided by the melting enthalpy. Kim and Ki (2014) developed a scaling law based on a one-dimensional heat conduction model to predict the penetration as a function of a single parameter. This single parameter is a combination of laser intensity, interaction time and a multiple reflections factor. The proposed scaling law has to be further studied, especially because it was limited to a **2 kW** laser in the experimental work.

A well-known function is the one presented in Equation (2.2), which basically states that the penetration depth (PD) remains constant if the heat input remains unchanged, where V is the welding speed (ERIKSSON; POWELL; KAPLAN, 2011). Although not completely accurate, it can be useful as a first guess if either the laser power or the welding speed must be varied.

$$PD \propto \frac{P}{V} \quad (2.2)$$

One interesting example of a simple equation to determine the weld penetration is the one created by Suder and Williams (2014) in the same work mentioned before. An empirical equation (2.3) was developed to determine the required power factor (P_F in MW/m) to achieve a defined penetration depth (PD in mm) at a given interaction time (t_i in ms). The equation was developed for beam diameters in the range from **0.35 mm** to **1.00 mm** and interaction times between **2.5 ms** and **150 ms** in a low carbon steel. As an empirical equation, its prediction capability is cannot be assured for welding conditions much different from the ones used in its development.

$$P_F = (4.25PD + 17) \times t_i^{(0.045PD-0.782)} \quad (2.3)$$

2.1.2 Laser Sources

A laser is usually known by its active medium. Since the first laser, which had a ruby crystal as its active medium (MAIMAN, 1960), many new kinds of laser have been developed, ranging from gas lasers to solid-state lasers and organic dye lasers. For laser welding, the most common are the carbon dioxide (CO_2) laser, the Nd:YAG laser, the fiber laser, the disc laser and the diode laser, being the first a gas laser, the last a semiconductor laser and the other three solid-state lasers. Each laser has its own set of characteristics, including the laser light wavelength, the beam quality and the efficiency.

The wavelength is a product of the quantum states involved in the laser generation, following Equation (2.4), where E is the difference between higher and lower energy levels, h is Planck's constant and c the speed of light. Usually, long wavelength lasers are related to molecular vibration levels, visible and near infrared lasers to electron orbit levels and ultraviolet

lasers to ionization effects (STEEN; MAZUMDER, 2010). The wavelength defines how the light interacts with matter and will be further discussed in Section 2.1.3.

$$E = \frac{hc}{\lambda} \quad (2.4)$$

Another important beam characteristic is how the power is distributed along its transverse section, that is, the intensity (or beam) profile. The most important factor determining the beam profile are the transverse electromagnetic modes (TEM) generated in the resonator. If the beam emerging from the resonator has peaks distributed in rectangular symmetry, Hermite polynomials in a cartesian coordinates can be used to describe the intensity distribution (Hermite-Gaussian beam). In that case, the notation TEM_{nmq} is used, where n is the number of nodes (zeros) in the horizontal direction, m is the number of nodes in the vertical direction and q is the number of longitudinal nodes. If the peaks are cylindrically symmetric, Laguerre polynomials in polar coordinates can adequately describe the profile (Laguerre-Gaussian beam). The notation TEM_{plq} is then used, with p being the number of radial nodes and l the number of angular nodes. q can be suppressed from the notation in most cases both for Hermite- and Laguerre-Gaussian beams. Examples of Hermite- and Laguerre-Gaussian modes can be seen in Figure 2.5. New studies have reached more general mathematical models where the Hermite- and the Laguerre-Gaussian modes are just specific conditions within a broader spectrum, allowing the characterization of more complex transverse modes (ABRAMOCHKIN; VOLOSTNIKOV, 2004; WANG et al., 2016).

Figure 2.6 shows different TEM modes ranging from a pure Hermite-Gaussian mode to a pure Laguerre-Gaussian mode.

Figure 2.5: Examples of Hermite- and Laguerre-Gaussian modes.

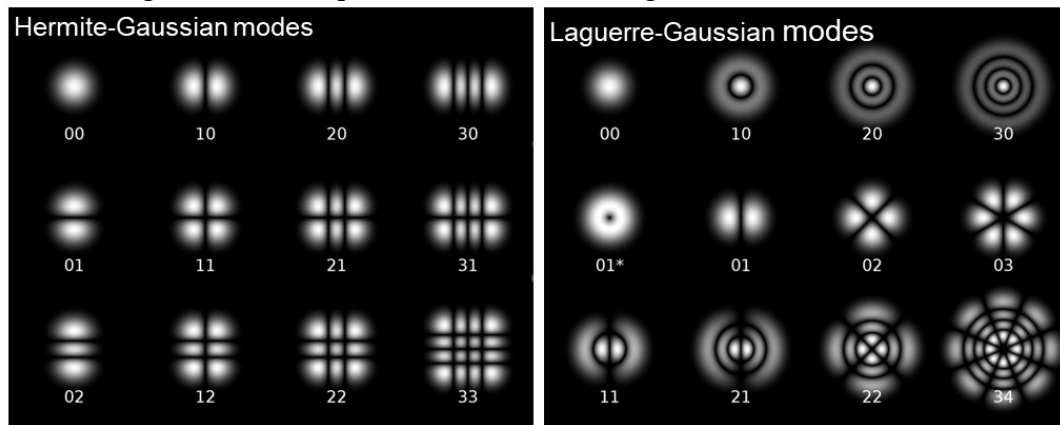
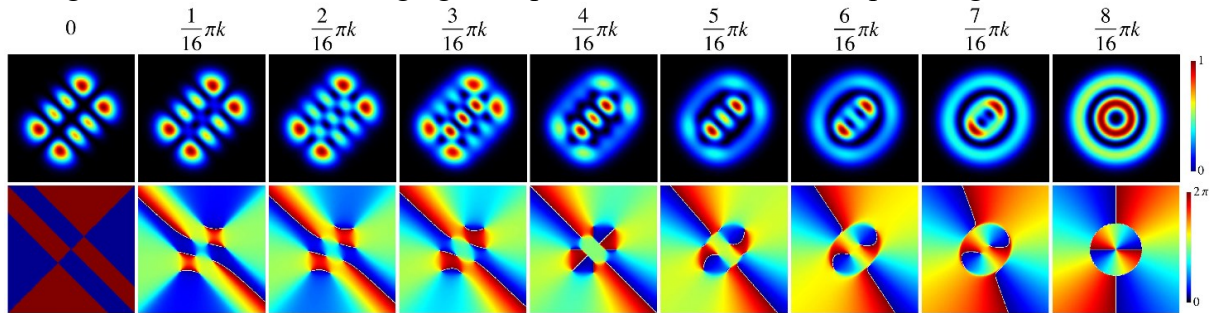
Adapted from: <http://www.optique-ingenieur.org>

Figure 2.6: TEM modes ranging from pure Hermite-Gaussian to pure Laguerre-Gaussian



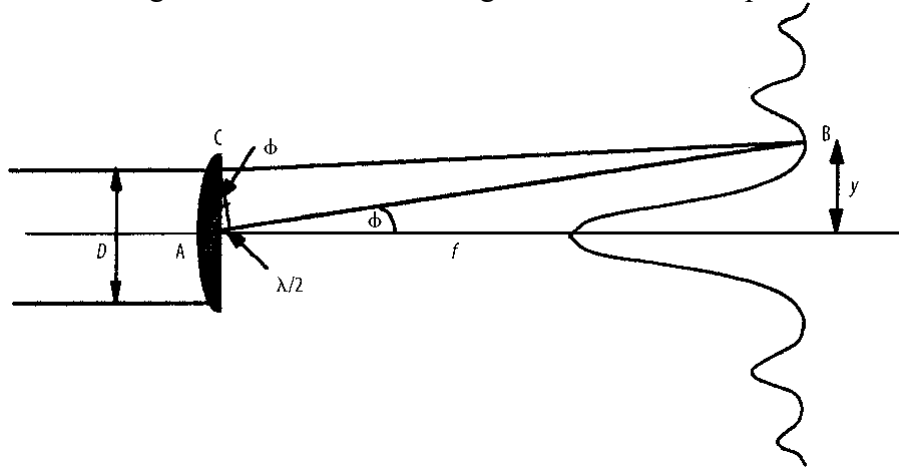
Source: (WANG et al., 2016)

Beam quality is the property of the laser beam to be focused on the smallest spot possible, that is: the better the beam quality, the smaller the laser spot at focus is for the same optical configuration. TEM modes have a big influence on the beam quality, therefore TEM₀₀ mode (gaussian) is preferred if high intensity is desirable. The light wavelength is also of high importance, since there is a theoretical limit to how small the focus spot can be due to diffraction, which is inversely proportional to the wavelength. That phenomenon happens because the rays of light at different portions of the beam travel different distances to the focal spot, leading to different phases interacting and, consequently, to interference fringes, with a maximum at the center (considering a gaussian front), as shown in Figure 2.7. The central peak, composed of approximately **86 %** of the beam power, is then considered the beam diameter, with the outer edges defined as the point at which the power distribution has fallen to $1/e^2$ of the peak, in the first dark fringe. Equation (2.5) represents the theoretical minimal beam diameter (d_{min}) for a circular planar beam, while Equation (2.6) is used for Laguerre-Gaussian beams of mode TEM_{plq} . F is the focal distance, D_L the beam width at the focusing lens and λ is the wavelength (STEEN; MAZUMDER, 2010).

$$d_{min} = \frac{2.44f\lambda}{D_L} \quad (2.5)$$

$$d_{min} = \frac{2.44F\lambda}{D_L} \times (2p + l + q) \quad (2.6)$$

Figure 2.7: Interference fringes on a laser focal spot.



Source: (STEEN; MAZUMDER, 2010)

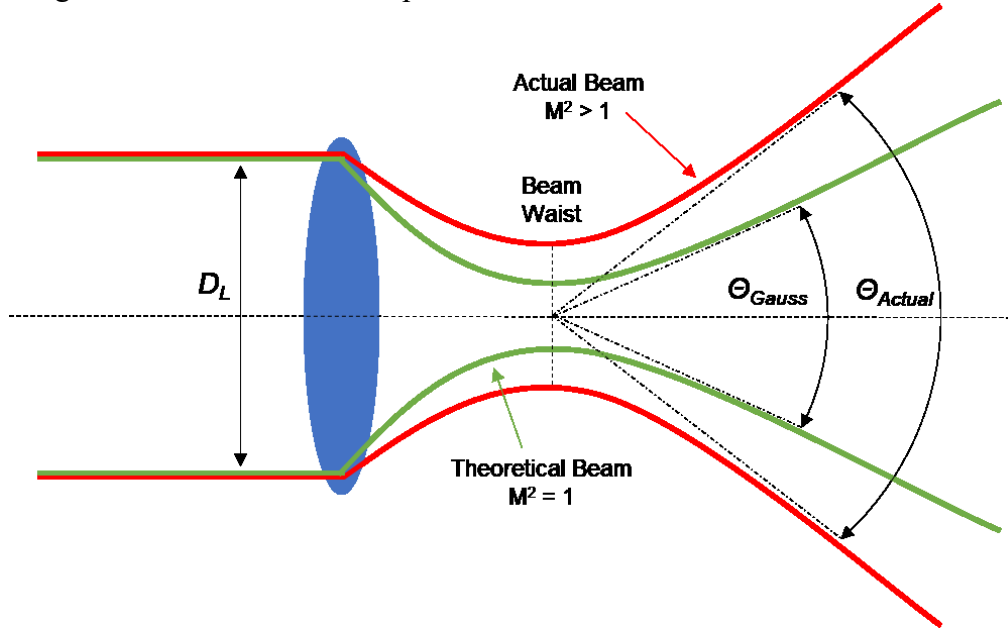
Due to this phenomenon, the solid-state and semiconductor lasers used in laser welding, with wavelengths close to $1 \mu\text{m}$, have the theoretical potential to produce smaller focal spots than the CO_2 lasers, which produce long $10 \mu\text{m}$ infrared light. Actual beams, however, never reach the theoretical limit, although some can get very close to it, like single mode fiber lasers (MASHIKO et al., 2016). High power Nd:YAG for instance were known for their poor quality, worse than the CO_2 lasers, despite the shorter wavelength (YASUI, 1996).

For actual lasers, the beam quality factor (M^2) can be used to quantify their quality. M is defined as the divergence angle of the actual beam (Θ_{Actual}) divided by the divergence of a theoretical diffraction limited beam with the **same origin** as the actual beam (Θ_{Gauss}) (Equation (2.7)). Steen and Mazumder (2010) show in detail how Equation (2.8) can be obtained from Equation (2.7), where Θ_r is the divergence angle of a theoretical diffraction limited beam with the same **initial beam waist** (focal spot width) as the actual beam. Figure 2.8 shows a comparison between an actual beam and a theoretical diffraction limited beam.

$$M = \frac{\Theta_{\text{Actual}}}{\Theta_{\text{Gauss}}} \quad (2.7)$$

$$M^2 = \frac{\Theta_{Actual}}{\Theta_r} \quad (2.8)$$

Figure 2.8: Actual beam compared to a theoretical diffraction limited beam.

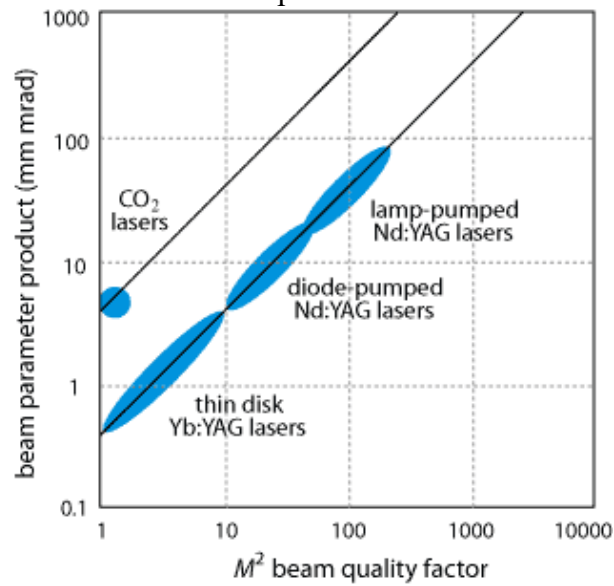


Source: Author

The Beam Parameter Product (BPP) is another beam quality measurement for lasers, which is defined as in the first equality of Equation (2.9) and can be related to the M^2 parameter by the second equality of the same equation. The smaller the BPP , the higher the beam quality, where the smallest BPP possible for a given wavelength is λ/π , when $M^2 = 1$ (LIENERT, 2011). w_0 is the beam waist width at focal position.

$$BPP = w_0 * \Theta_{Actual} = \frac{\lambda M^2}{\pi} \quad (\text{mm*mrad}) \quad (2.9)$$

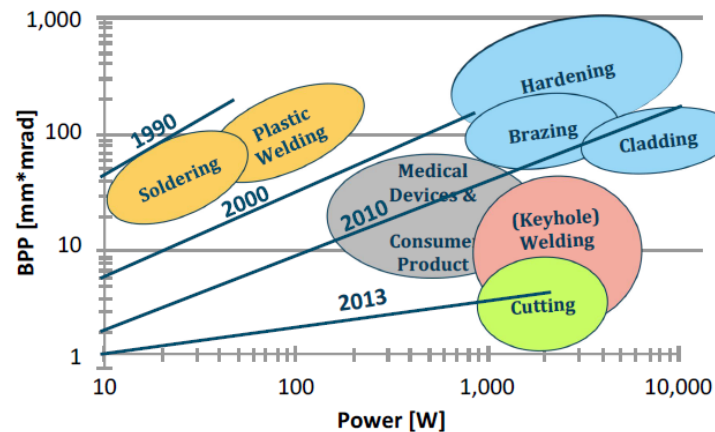
The BPP can be a more practical measure of beam quality than the M^2 as lasers with different wavelengths can be easily compared and as the beam waist and the divergence angle can be quickly calculated for any optical system if the BPP is known and the optics do not cause significant beam degradation (optical aberration). However, some optics do lead to beam degradation, especially optical fibers. The effective BPP for a fiber transported laser beam will be a function of the fiber diameter (LIENERT, 2011). A comparison between M^2 and BPP for different laser sources is shown in Figure 2.9. It is noticeable that, despite having good M^2 (near 1), the CO_2 lasers have worse BPP beam quality than the disk lasers (PASCHOTTA, s.d.).

Figure 2.9: BPP and M^2 comparison for different laser sources.

The first generation of high power lasers (CO₂ and Nd:YAG) have been losing market to the second generation (fiber and disk) steadily during the last and present decades, due to better wall-plug efficiency, to better beam quality and to smaller footprint. Compared to CO₂ lasers, the second generation also has some big advantages in the possibility to have its light transported by optical fiber and not only by hard optics and also in its less frequent maintenance requirement (SALMINEN; PIILI; PURTONEN, 2010).

Diode laser applications in high power laser welding are also growing, as new models are reaching good beam qualities at high powers. With even better wall-plug efficiency (typically, **50 %** compared to **30 %** from fiber and **25 %** from disk), smaller footprint and some wavelength flexibility, the diode lasers are called by some the third high power lasers generation and are becoming viable in applications once limited to fiber and disk lasers (FRITSCHÉ et al., 2015). Figure 2.10 shows the typical powers and beam qualities required for different laser processes (colored areas) and how the diode lasers have evolved through the years (straight lines).

Figure 2.10: Typical power and beam quality in different laser material processes and the evolution of diode lasers.



Source: (FRITSCHKE et al., 2015)

2.1.3 Laser-Matter Interaction

Since light is an electromagnetic wave, composed of perpendicular concomitant oscillations in the electric and in the magnetic field, and since matter is largely composed of charged particles (electrons and protons), light and matter should interact. Interaction will happen whether the particles are free to move or if they are tightly bound together (JORDAN; BALMAIN, 1968) *apud* (MULDERS, 1987).

The interaction processes will vary between dielectric (insulators) and conductor materials. In the first, the oscillating electric and magnetic fields from the electromagnetic wave will induce the formation of dipoles and interact with them, while in the later the interaction happens mostly in free electrons. The dipoles in dielectrics can form due to (POPRAWA, 2011):

- Electronic polarization: the negatively charged electrons are dislocated in relation to the positively charged nucleus, oscillating out of the equilibrium positions.
- Ionic polarization: the differently charged ions oscillate in respect to one another.
- Orientation polarization of permanent dipoles: permanent dipoles, such as H₂O molecules, align with the electric field, leading to vibration and/or rotation of the molecules.

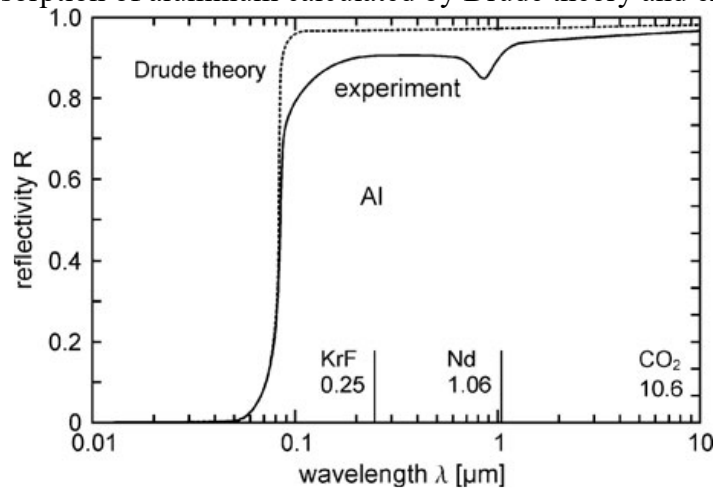
Each dipole under the influence of an electromagnetic wave behaves as a harmonic oscillator, with its eigenfrequency and damping constant. The closer the wave frequency is to the eigenfrequency of the dipole, stronger is the interaction. Therefore, orientation polarization is negligible in laser material processing, as their natural frequencies are far below that of the infrared spectrum due to their high inertia. Ionic polarization dominates in the infrared region, while electronic polarization is the main interaction process in shorter wavelengths, from near-

infrared to X-ray, as electrons have the smallest mass of the charged particles, and thus shorter natural frequencies (POPRAWA, 2011).

In metals and plasmas, the interaction happens mostly with the free electrons (conduction electrons), which are free to move with the electromagnetic field. Differently from the dipoles in dielectric materials, the free electrons can efficiently interact with any wavelength up to the ultraviolet region in metals. For this reason, the absorption spectra of metals are mostly continuous from far-infrared to the ultraviolet region, without discrete absorption bands as in insulators (POPRAWA, 2011).

When the electrons are dislocated due to an electric field, there will be charge imbalances in the material and Coulomb forces will act as restorative force. The natural frequency of that system will be a function of its effective mass and number density of electrons, being called the plasma frequency (ÖZDEMİR; HAN, 2014). When the electromagnetic wave frequency is below the plasma frequency, the wave will be almost entirely reflected at the few first atomic layers, with some absorption due to electron collisions with other particles. The depth the electromagnetic wave penetrates into the material is the skin depth, which is in the order of 10^{-8} m (HOFFMAN; SZYMANSKI, 2002). For this reason, metals appear colorless and shiny. When the frequency of the wave is above the plasma frequency, the material becomes transparent to the wave and transmission is possible. For metals, the plasma frequency is usually in the ultraviolet region (ÖZDEMİR; HAN, 2014). Figure 2.11 shows the reflectivity index of aluminum as calculated treating the conduction electrons of the metal as free electrons in a gas (Drude theory) and comparing it to experimental results.

Figure 2.11: Absorption of aluminum calculated by Drude theory and experimental data.



Source: (POPRAWA, 2011)

Electromagnetic radiation propagating through a medium will cause the charges (free charges or dipoles) to oscillate with it as harmonic oscillators. If the wave frequency is not the same as the oscillator's, the charges will oscillate with the same frequency as the wave, but there will be low interaction. If the frequencies match or are very close, the oscillation amplitude will be higher, leading to high interaction between radiation and matter. The oscillating dipoles and charges will themselves cause fluctuations in the electromagnetic field and reemit waves with a small phase change, that leads to a perceived reduction of propagation speed, the refraction.

In crystalline solids, amorphous solids and liquids, the long-range and short-range order of atoms and molecules will lead to destructive interference of the reemitted radiation in every direction except for the original direction of propagation, similarly to Huygen's principle. In gases and plasmas, every oscillator will act independently, scattering the light. Scattering also happens in liquids and solids due to the presence of defects, inclusions, inhomogeneities, etc. At the interface of solids and liquids, there is also a thin layer (around half of the wavelength) where back reradiation is not completely cancelled by interference, enabling the reflection of light (MULDERS, 1987).

Absorption, on the other hand, happens when the dipoles and charges transform the energy of the wave to kinetic energy of the particles (temperature) instead of reemitting it, as in collision events for example. Light can be absorbed by different phenomena in different materials.

Light propagating through plasma will be mostly absorbed by inverse Brehmsstrahlung and by photoionization (HOFFMAN; SZYMANSKI, 2002), considering that typical plasma frequencies in plasmas are much lower than the infrared, so lasers can propagate through it. The inverse Brehmsstrahlung phenomenon happens when an electron absorbs one or more photons during the collision with another particle, transforming its energy into particle's kinetic energy (DELONE, 1993). However, if the photon was absorbed by a free electron without collision, the electron would reemit the wave and the light would propagate further. Photoionization is the ionization of an atom due to the absorption of one or more photons, which plays a bigger role as the wavelength is reduced (HOFFMAN; SZYMANSKI, 2002).

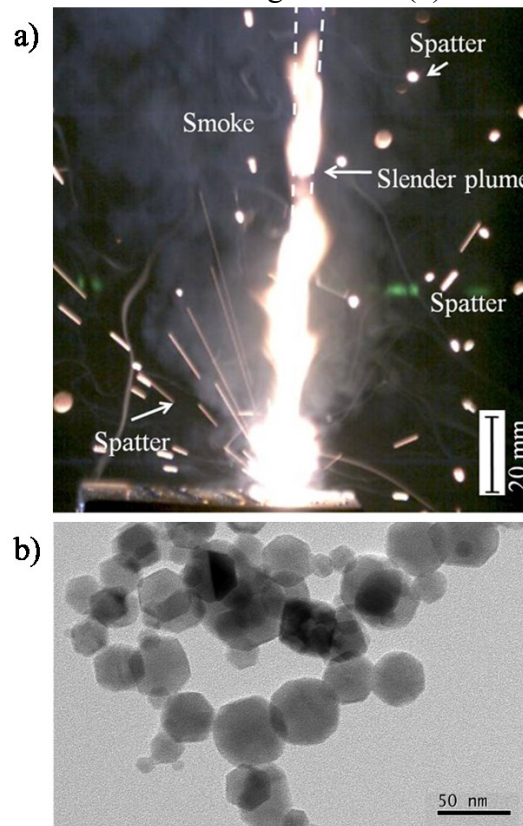
During high power LBW, the high temperature of the process gases and evaporated alloy components can form a plasma inside the vapor capillary, which is ejected and forms a plume above the processing area. The absorption by inverse Brehmsstrahlung is proportional to the wavelength squared, so this absorption process is 100 times more effective for CO₂ lasers

(**10 μm**) than for solid-state lasers (**1 μm**). The difference is actually even higher, as the absorbed power increases the plasma temperature to around **8000 K** and **17000 K**, which increases the absorptivity as well. In some cases, the laser power can be almost completely absorbed by the plasma, resulting in very low penetration (ŠČEGLOV, 2012). Helium is commonly used as the shielding gas for high power CO₂ LBW due to its high ionization potential, mitigating the plasma blocking effect.

The plume temperature during high power solid-state LBW is typically between **3500 K** and **6000 K**, in which case only a weakly ionized plasma is formed (ŠČEGLOV, 2012). The attenuation of the laser beam by inverse Brehmsstrahlung when crossing such a plume is expected to be below **1 %**, so it can be considered negligible (ZOU et al., 2016). However, there is a notable difference in penetration when a plume suppressing jet is used to blow the plume away from the process. The loss of penetration might be due to the Rayleigh scattering effect (KAWAHITO et al., 2008). Rayleigh scattering is an elastic scattering phenomenon which happens when particles smaller than the wavelength interact with the electromagnetic radiation, from free electrons up to around one tenth of the wavelength. Zou *et al.* (2016) analyzed the plume and found round condensed particles with **40 nm** average diameter in the plume and around the process in the form of a white smoke, as depicted in Figure 2.12. Since there is an environment rich in small particles and Rayleigh scattering is inversely proportional to the fourth power of the wavelength, the scattering can be responsible for the **10 %** to **70 %** attenuation observed by Greses *et al.* (2004) or the **9 %** attenuation observed by Ščeglov (2012).

The loss of penetration can also be partly attributed to the high turbulence and high temperature gradients found in the plume, which can randomly refract the laser beam, causing loss of focus, deflection of the beam and even splitting it into separated beams (KATAYAMA; KAWAHITO; MIZUTANI, 2010). This effect should however be negligible if the plume is properly suppressed (KAWAHITO et al., 2008; YOUSUKE et al., 2005; ZOU et al., 2016).

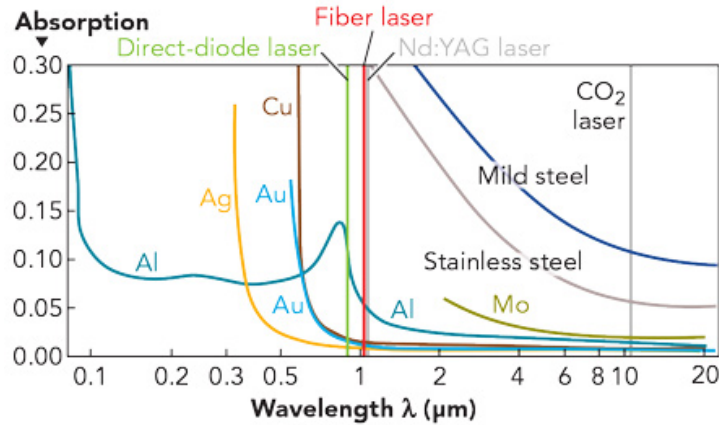
Figure 2.12: Plume and smoke during high power fiber LBW (a) and the collected particles observed through a TEM (b).



Adapted from: (ZOU et al., 2016)

When the laser light meets a metallic surface, its frequency is usually below the plasma frequency of the metal, so the light penetrates just a few nanometers, with most of it being reflected and only a small portion being absorbed by inverse Brehmsstrahlung. For that reason, reflectivity of metals to infrared light is typically between **0.9** and **0.99** and from **0.45** to **0.95** to visible and near ultraviolet light (BÄUERLE, 2011). Therefore, solid-state lasers tend to appreciate a higher absorptivity coefficient than CO₂ lasers in metal processing, which is especially advantageous during conduction mode LBW and heat treating. Figure 2.13 shows the spectral absorptivity coefficient curve for different metals and typical laser wavelengths for a perpendicular light incidence. Due mostly to increased electron-phonon interaction (collision frequency), the reflectivity of metals tends to decrease as temperature rises. At high temperatures, surface contamination (oxidation, nitridation, etc.) and surface deformation (corrugations, ripples, etc.) also increase the surface absorptivity and can have an even higher influence than the material's inherent decrease in reflectivity caused by the increased electron-phonon interaction (BÄUERLE, 2011).

Figure 2.13: Spectral index of absorption for different metals and typical lasers wavelength.



Source: www.industrial-lasers.com

The beam's angle of incidence and polarization also plays a role in light behavior at the gas-solid interface. The electromagnetic wave radiating on a surface can be decomposed into perpendicular and parallel components to the incidence plane. The Fresnel Equations (Equations (2.10) and (2.11)) can be used to calculate the reflectivity of each component (R_s for perpendicular, R_p for parallel) as a function of the real part of the solid's index of refraction² (n), the angle of incidence (ϕ) and the imaginary part of the index of refraction (κ).

$$R_p = \frac{\left[n - \left(\frac{1}{\cos \phi} \right) \right]^2 + \kappa^2}{\left[n + \left(\frac{1}{\cos \phi} \right) \right]^2 + \kappa^2} \quad (2.10)$$

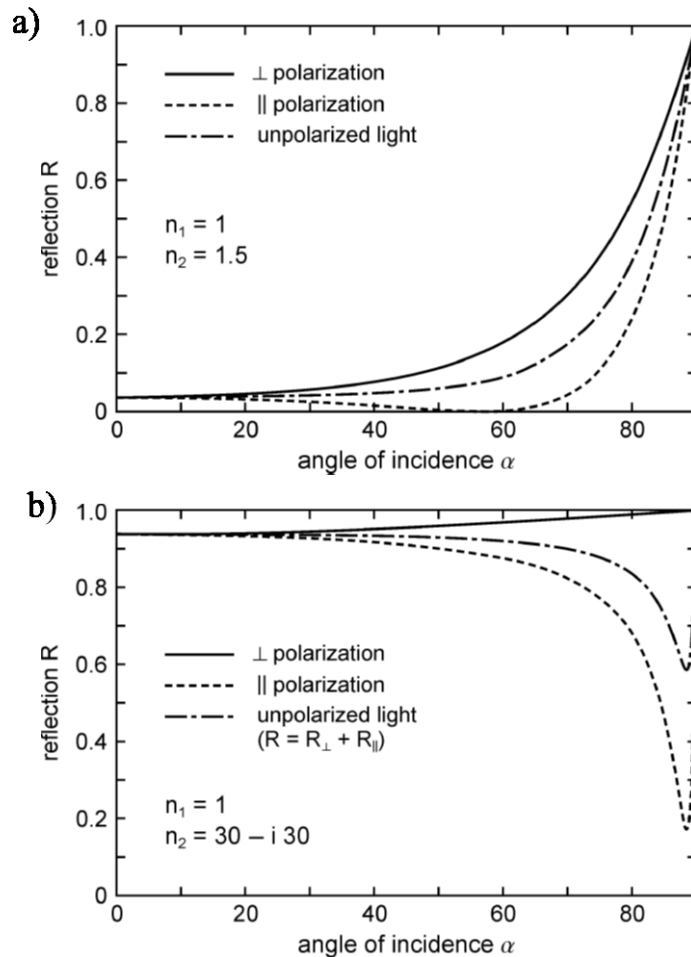
$$R_s = \frac{[n - \cos \phi]^2 + \kappa^2}{[n + \cos \phi]^2 + \kappa^2} \quad (2.11)$$

The behavior of the reflectivity indexes at different incidence angles can be seen in Figure 2.14, where it was considered a ray of light travelling through vacuum ($n_1 = 1$) and hitting a solid with a) low index of refraction without an imaginary part ($n_2 = 1.5$); and b) higher index of refraction with imaginary part ($n_2 = 30 - i30$), which is close to the properties of aluminum. As can be observed, there is an angle where there is a minimum for the parallel polarization, reaching zero if the absorption of the material is not considered. It is called the Brewster angle. At the Brewster angle, the vibration of the electron needed to reflect the parallel polarized

² The real part of the index of refraction describes the phase change of the wave propagating through the material, which causes the perceived reduced propagation speed. The imaginary part indicates the propagation losses or absorption (when negative) or optical gain (when positive).

light is constrained because in doing so would result in the electron leaving the surface (POPRAWA, 2011; STEEN; MAZUMDER, 2010).

Figure 2.14: Reflectivity behavior as a function of the angle of incidence for two different materials.



Adapted from: (POPRAWA, 2011)

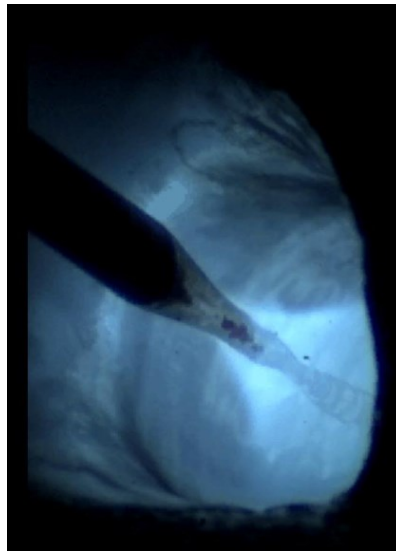
2.2 BURIED ARC

Buried arc is a condition in arc welding under which the arc column is mostly or entirely found beneath the surface of the base metal, buried in a depression on the molten pool. The deep depression is the result of increased arc pressure on the pool surface.

In GMAW, the buried arc has been traditionally used for steel welding with CO_2 shielding gas and repelled globular transfer mode. As the metal transfer happens inside the pool depression, the spatter is confined and a sound bead can be obtained. Higher penetration is another advantage of using the buried arc in repelled globular transfer mode (LIENERT, 2011).

In recent years, a profusion of commercial variants of the GMAW that rely on high plasma pressures to achieve higher penetration in the spray and in the short circuit transfer modes have been developed as well (BENGTSSON; SKARIN, 1991; BUDIG, 2005; DVS, 2015; JAESCHKE; VOLLRATH, 2009; LORCH, 2016; THE LINCOLN ELECTRIC COMPANY, 2005). Although the term “buried arc” is rarely used to describe these variants, one can notice that the higher plasma pressure and penetration result from short arc lengths that are mostly or entirely buried within the molten pool, as can be observed in the SpeedArc process from Lorch, in Figure 2.15.

Figure 2.15: Observation of a buried arc in the SpeedArc process.



Source: (LORCH, 2016)

When applied to the GTAW, the buried arc can extend the applicability of GTAW to joining of thick sections and increase thermal efficiency and welding speed for thinner materials, with typical currents in the range from **500 A** to **1000 A** (ADONYI; RICHARDSON; BAESLACK, 1992). Even keyhole mode welding has become possible due to the increased arc pressure on fully or partially buried arcs (JARVIS, 2001; OLIVARES et al., 2015; PORT et al., 2007). If a fully buried arc is to be used in GTAW, the arc has to be initiated above the surface and then lowered to below the surface once the molten pool has developed (ADONYI; RICHARDSON; BAESLACK, 1992; NORRISH, 2006).

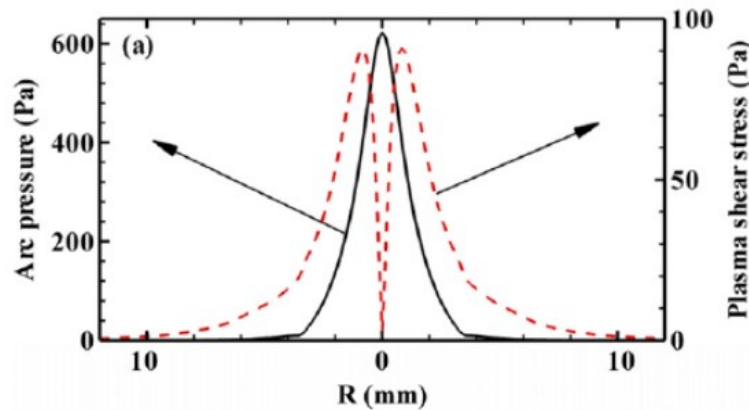
The buried arc condition has also been observed in the SAW process by Mendez *et al.* (2015) by a high-speed imaging technique that gives visual access to the process below the flux. Welding with **500 A** and approximately **1.6 m/min** wire feed rate with a **3.2 mm** wide carbon steel wire resulted in repelled globular metal transfer with the arc above the workpiece surface. As the current increased to **1000 A** and wire feed rate to **4.5 m/min**, the arc was contained

entirely below the workpiece surface (buried arc) and the metal transfer mechanism seemed to become unstable and based on the kink instability. The penetration increased by **140 %** and higher depth to width ratio were appreciated.

2.2.1 Pool Depression

At lower current levels (under **200 A**), the pool dynamics are dominated by the Marangoni forces, with outward surface flow resulting in shallower and wider welds and inward flow resulting in deeper and narrower welds (MENDEZ; EAGAR, 2000). At higher currents, plasma forces become increasingly more important than the Marangoni forces, with the plasma shear stress being typically one order of magnitude higher than any other active force, including the plasma stagnation pressure, while the dominant reactive force is due to viscous effects (MENDEZ; EAGAR, 2000). The plasma stagnation pressure shows a gaussian distribution with its maximum around the center of the cathode and sharply decreases as it moves away from the center, while the plasma shear stress has its maximum at a certain radial distance from the cathode center, as can be seen in the numerical model from Hu and Tsai (2007), presented in Figure 2.16. The increased arc forces at higher currents lead to a depression in the pool.

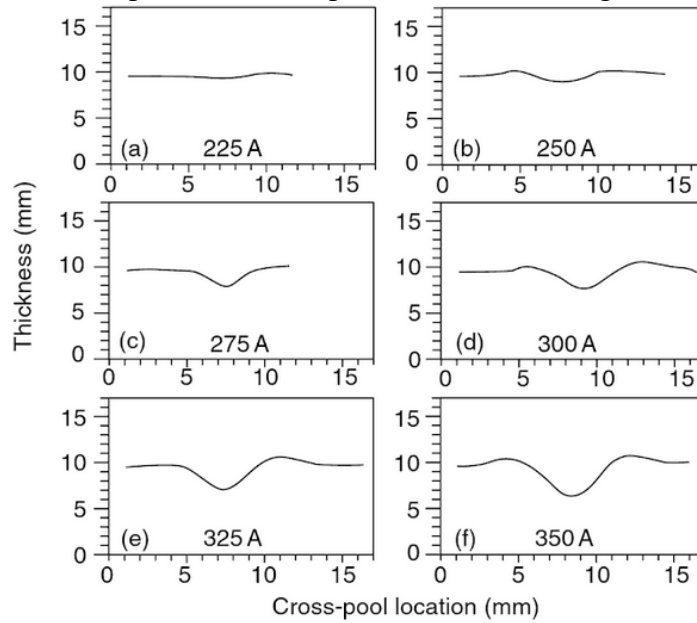
Figure 2.16: Radial distribution of plasma stagnation pressure and plasma shear stress.



Source: (HU; TSAI, 2007)

Using x-ray imaging and a pivoting arm attached to a balance, Rokhlin and Guu (1993) measured the pool depression and the arc force during GTAW. It was observed that both the depression and the force were linearly proportional to the current squared, with **200 A** as the threshold current for depression formation. It was proposed that surface tension also plays an important role as a resisting force, leading to reduced pool depression as the surface tension coefficient increases. The pool surface shape at different current levels is shown in Figure 2.17.

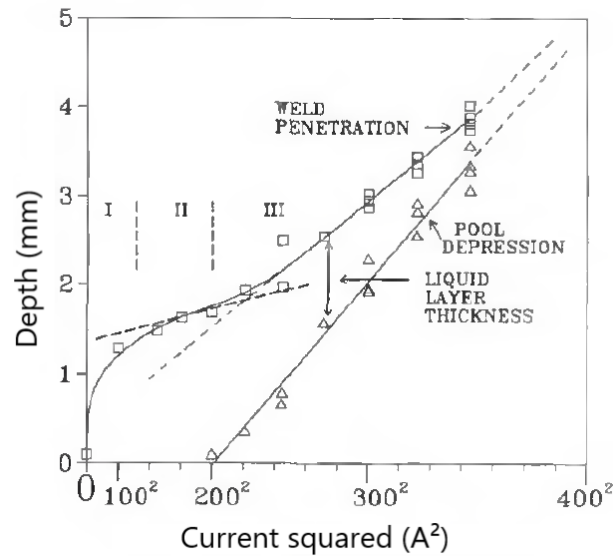
Figure 2.17: Pool depression development with increasing current in GTAW.



Source: (ROKHLIN; GUU, 1993)

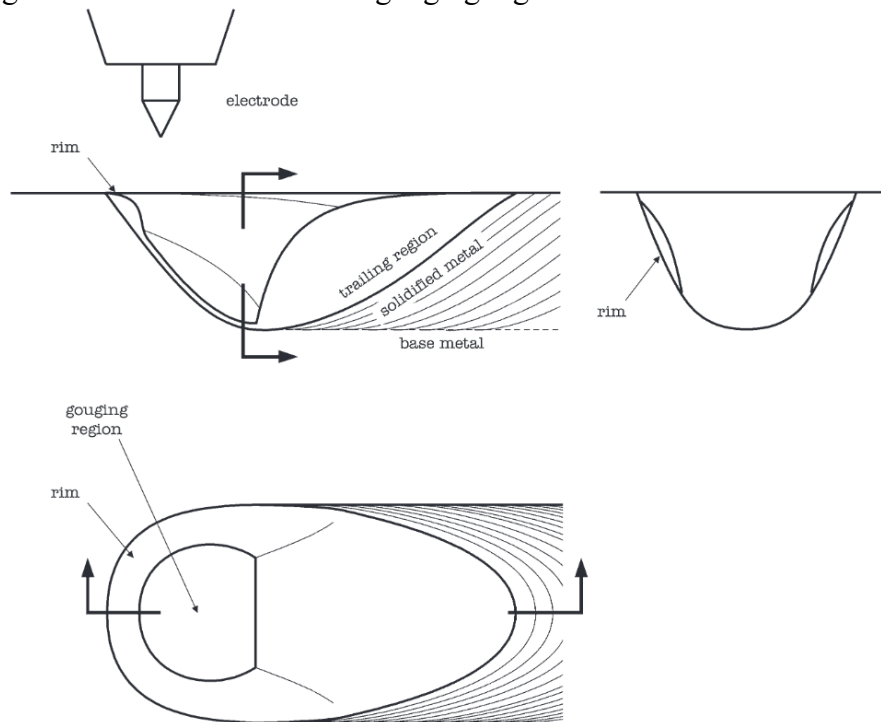
Rokhlin and Guu (1993) observed three process regions with different penetration behavior, as seen in Figure 2.18. At low currents (up to **100 A**) the penetration rapidly increased with the current, as the heat of the arc is almost directly transferred to the base metal. Between **100 A** and **200 A**, the molten pool acts as an insulator between the arc and the base metal, with the heat being transferred to the base metal by conduction and convection through the molten metal. In this region, the penetration rises slowly with the current. After the onset of the pool depression at **200 A** the penetration had a steeper growth, because the liquid layer becomes thinner (around **0.5 mm** at currents above **300 A** was observed in their work), increasing the efficacy of heat transfer from the plasma to the base metal. Mendez and Eagar (2000) found a layer of molten metal as thin as tens of micrometers in high current GTAW. They describe the molten pool as having a gouging region (the depressed thin portion of the pool) with rims at the front and at the sides of the depression with metal flowing backwards to a trailing region, where it builds up, as in Figure 2.19. Similar formations have also been observed in high current GMAW (BRADSTREET, 1968) and in GTAW numerical simulation (MENG; QIN; ZOU, 2016).

Figure 2.18: The three penetration regions observed in GTAW.



Source: (ROKHLIN; GUU, 1993)

Figure 2.19: Schematics of the gouging region observed in 500 A GTAW.



Source: (MENDEZ; EAGAR, 2000)

The deep pool depression in high current arc welding processes can be linked to the occurrence of several weld pool defects, such as humping, undercutting, split bead, parallel humping and tunnel porosity (CHO; FARSON, 2007; MENDEZ; EAGAR, 2003). Interestingly, despite the plasma shear stress dominance, the Marangoni forces seem to be relevant at the rims and at the trailing region. In steels, the usage of low sulfur base metal (AISI 304) showed much better results regarding such defects than higher sulfur contents for both GTAW

and GMAW at high current (from **274 - 500 A**) and travel speed (**10.6 - 15.0 mm/min**) (MENDEZ; EAGAR, 2003). These experiments were carried on AISI 304 base metal with pure argon shielding gas, currents ranging from **274 A** to **500 A** and welding speeds between **10.6 mm/s** and **15.0 mm/s**.

Not only the total amount of current passing through the arc is important to the pool depression effect, its distribution plays an important role as well. It has been observed that the plasma pressure increased when the current flux was enhanced through different means, such as:

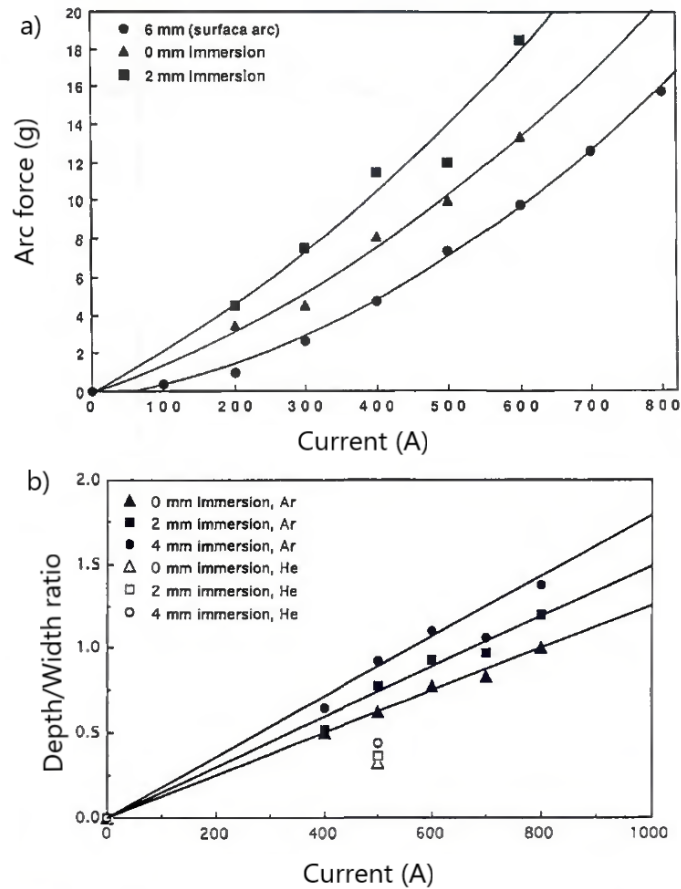
- Different tungsten electrode shapes (FAN; USHIO; MATSUDA, 1986; FAN; SHI, 1996);
- Arc constriction due to high frequency pulsing in GTAW (YANG et al., 2017);
- Increased shielding gas pressure and reduced gas nozzle opening, constricting the arc with a thermal pinching effect (HAM; OH; CHO, 2012).

As expected, the chosen shielding gas also affects the plasma force, with Argon showing higher force and depression than Helium for the same GTAW conditions (ADONYI; RICHARDSON; BAESLACK, 1992; LIN; EAGAR, 1986).

In GMAW, the consumable electrode can also influence the pool depression. It has been shown that the metal droplet flying through the arc can disturb the current flow (HU; TSAI, 2007). The droplets also transfer kinetic energy and momentum during the collision with the molten pool (SCOTTI; RODRIGUES, 2009; WANG; TSAI, 2001). With high speed imaging, Scotti and Rodrigues (2009) measured droplet arrival speeds of up to **2.70 m/s** in aluminum GMAW.

Higher arc forces can also be obtained by reducing the electrode to workpiece distance and the arc length. In fact, subsurface arcs have been shown to result in higher arc forces and deeper welds in GTAW, as presented in Figure 2.20 (ADONYI; RICHARDSON; BAESLACK, 1992; JARVIS, 2001). This is the principle behind the higher penetration in buried arc welding.

Figure 2.20: Arc force (a) and depth/width ratio (b) as functions of the current at different electrode positions in GTAW.

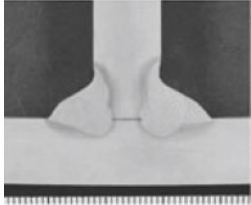
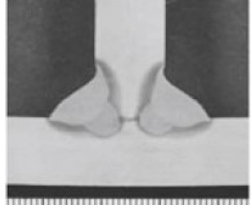
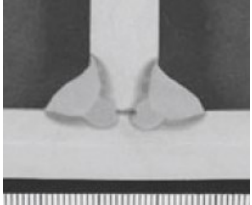


Source: (ADONYI; RICHARDSON; BAESLACK, 1992)

2.2.2 Buried Spray Arc GMAW

The first commercial usage of the buried spray arc GMAW was probably AGA's Rapid Melt moderated spray arc. At higher voltage, the Rapid Melt would produce a rotating spray arc with high deposition rate and wide bead. However, at lower voltages, the so-called moderated spray arc mode would be obtained, which consisted of a buried projected spray arc with high deposition rate and deep penetration (BENGTSSON; SKARIN, 1991; MATUSIAK; PFEIFER, 2008). Table 2.2 shows the effect of reducing the process voltage to achieve a buried arc in weld penetration (YUAN; YAMAZAKI; SUZUKI, 2016).

Table 2.2: Weld penetration increase by decreasing voltage.

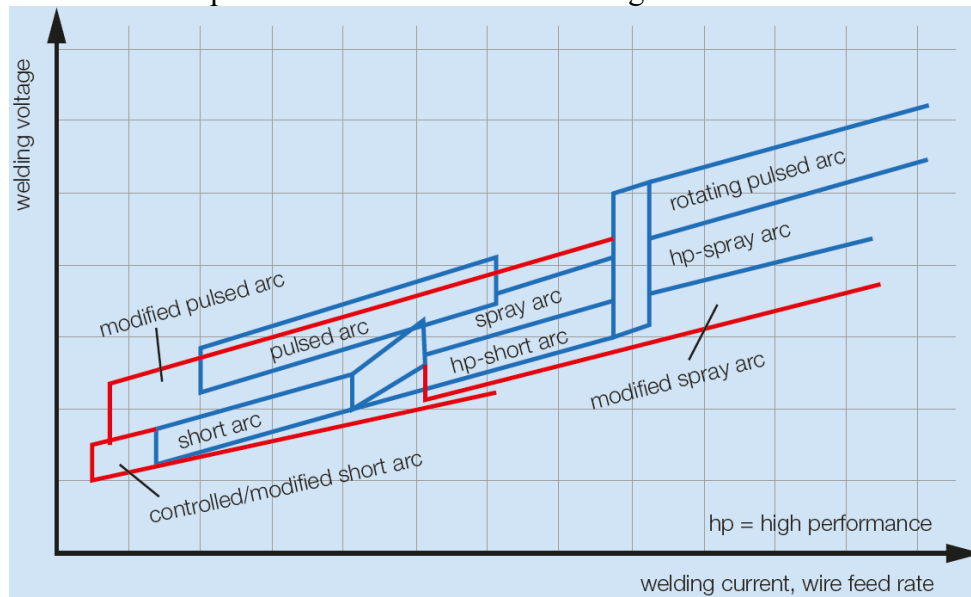
Wire feed rate	8 m/min		
Current	474 A	464 A	454 A
Voltage	31.6 V	29.1 V	26.3 V
Penetration	7.2 mm	8.1 mm	8.7 mm
Cross section			

Adapted from: (YUAN; YAMAZAKI; SUZUKI, 2016).

Following the moderated spray Rapid Melt from AGA, other companies developed their own variants of the GMAW based on the buried spray arc. EWM developed its forceArc (BUDIG, 2005), Lorch the SpeedArc (LORCH, 2016), Cloos the Rapid Weld, Fronius the PCS, Merkle the DeepARC and so forth (DVS, 2015). All those variants work in a forced short spray arc condition, where higher wire feed rates and stick-out lengths are used to form very short arcs with deep pool surface depression (BUDIG, 2005; CRAMER; BAUM; POMMER, 2011). The advances in welding source electronics played an important role in the development of those processes, enabling the sources to detect and quickly actuate in the event of a short circuit, which becomes more critical in such short arc lengths (BUDIG, 2005; CRAMER; BAUM; POMMER, 2011).

There is no well adopted nomenclature for those processes yet. The German Welding Society (DVS) has been one of the first entities to try to categorize the over 50 commercial processes developed in recent years by wave form manipulation, publishing an information sheet with a proposed classification (DVS, 2015). Following that classification, the buried spray arc GMAW would be called “modified spray arc”, and its position on a current x voltage diagram would be as shown in Figure 2.21, in a high-current low-voltage condition. Other nomenclatures found in the literature include: Gas Metal Buried Arc Welding (GMBAW) (STOL; WILLIAMS; GAYDOS, 2006) and buried arc GMAW (BABA et al., 2017).

Figure 2.21: GMAW processes classification according to DVS 0973 information sheet.



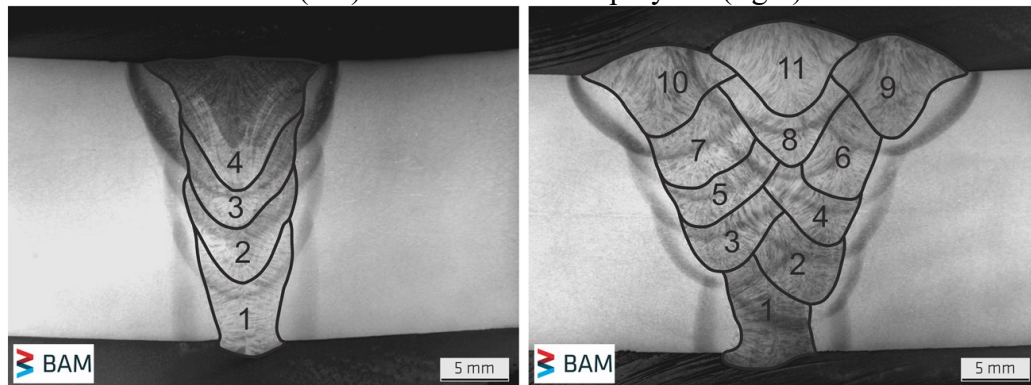
Source: (DVS, 2015)

In the absence of a well-defined nomenclature in the literature, the present author suggests adding the adjective “buried” in front of the International Institute of Welding (1976) metal transfer mode terminologies, which results in a specific and clear nomenclature. In that case, the moderated spray Rapid Melt process would be named “buried (projected³) spray arc GMAW”, while the nomenclature for the Rapid Arc process would be “buried short arc GMAW”.

Welding with a buried spray arc results in good penetration, a directionally stable arc, high welding speed, reduced heat input, reduced tendency of undercutting and good root formation (BUDIG, 2005; DOMPABLO, 2013). For thick sections, the longer stick-out (up to **40 mm**) and more contained arc enable the welding of narrower joints, with less filling passes being necessary, leading to higher productivity, reduced thermal distortions and reduced environmental impact (SCHAUPP; RHODE; KANNENGIESSER, 2018; SCHROEPFER; KROMM; KANNENGIESSER, 2017; SPROESSER et al., 2015). Figure 2.22 shows **20 mm** thick plates butt welded with a narrow groove joint (buried spray arc) and a regular V-joint preparation (conventional spray arc), where the reduced number of passes and lower heat input are clearly observed when buried spray arc is used.

³ Whenever the sort of spray arc is not specified in this work, the author is referring to both projected and streaming spray arcs, without relevant distinction between them.

Figure 2.22: Welding of thick plates using the modified spray arc with narrower joint preparation (left) and conventional spray arc (right).

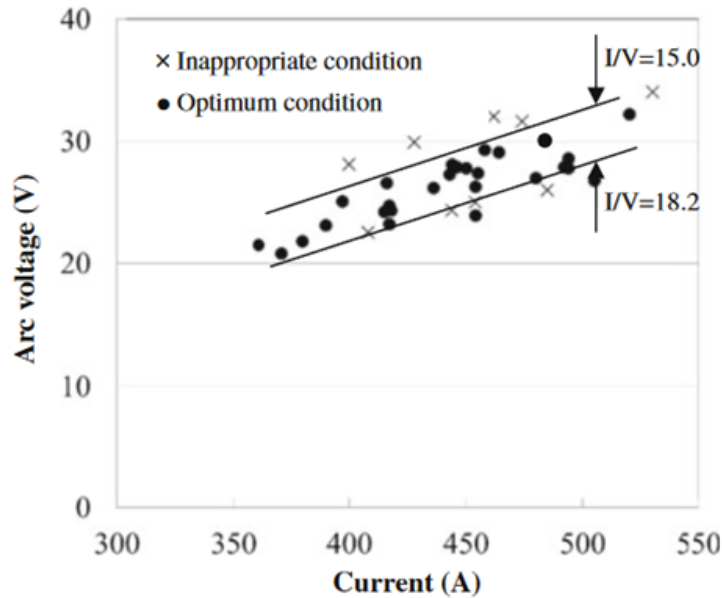


Source: (SCHAUPP; RHODE; KANNENGIESSER, 2018)

In general, the shielding gas is composed of argon and carbon dioxide mixtures and fed at **20 l/min** or more. In most works, either Ar + 8 % CO₂ (BENGTSSON; SKARIN, 1991) or Ar + 18 % CO₂ (HEINZE et al., 2014; SCHAUPP; RHODE; KANNENGIESSER, 2018; ZHANG et al., 2015) are used. The presence of CO₂ in the shielding gas stabilizes the axial spray arc at higher currents (WEMAN; LINDEN, 2006), which is important to avoid the kink instability at the high welding currents usable during buried spray arc.

Interestingly, the transition from globular to spray metal transfer with pure CO₂ shielding gas has been observed in the buried arc condition. It is believed that the arc attachment to the sidewalls of the pool depression causes it to attach higher onto the sides of the wire electrode, emulating the high argon content arcs behavior (YUAN; YAMAZAKI; SUZUKI, 2016). Yuan *et al.* (YUAN; YAMAZAKI; SUZUKI, 2016), using a **1.6 mm** wire and pure CO₂ shielding gas, found an optimum current-voltage ratio (I/V) of between **15.0 A/V** and **18.2 A/V** for buried spray arc GMAW where a stable process could be obtained at currents higher than **400 A**. Too high I/V ratios resulted in the wire diving too deep into the weld pool to keep a stable arc open, while the buried arc condition was not observed at lower I/V ratios and the process would revert to a repelled globular transfer. The obtained process window can be seen in Figure 2.23.

Figure 2.23: Appropriate I/V ratio for buried arc.



Adapted from: (YUAN; YAMAZAKI; SUZUKI, 2016)

Also with pure CO₂ as shielding gas, Baba *et al.* (2017) found two metal transfer conditions at different current ranges in the buried arc condition: projected spray arc and rotating spray arc (or pendulum). With the usage of pulsed current to alternate between both transfer modes, they developed a process capable of butt welding **19 mm** thick plates in a single pass buried spray arc GMAW. Current and voltage acquisition and high-speed imaging of the process are shown in Figure 2.24 and the single pass welding of **19 mm** thick ASTM A36 steel with different butt joint configurations can be seen in Figure 2.25.

Figure 2.24: Alternated projected and rotating spray buried arc current and voltage evolution and high-speed imaging.

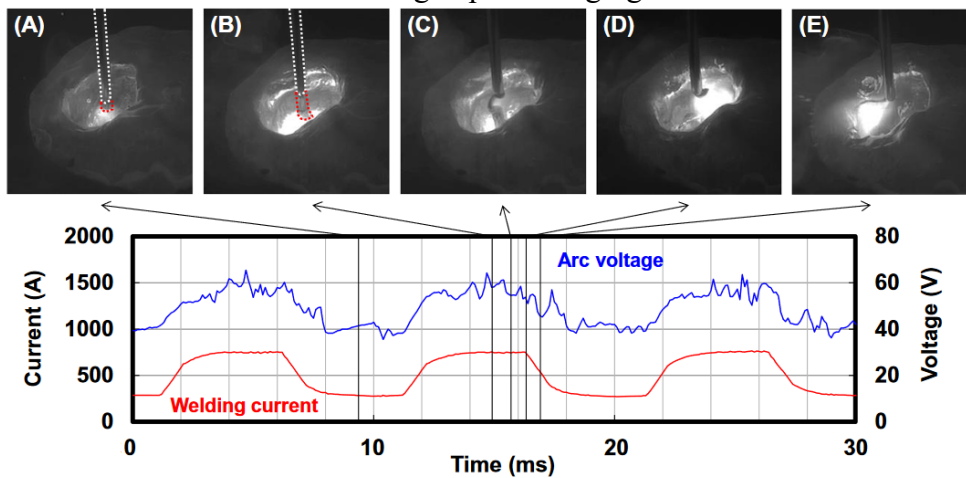
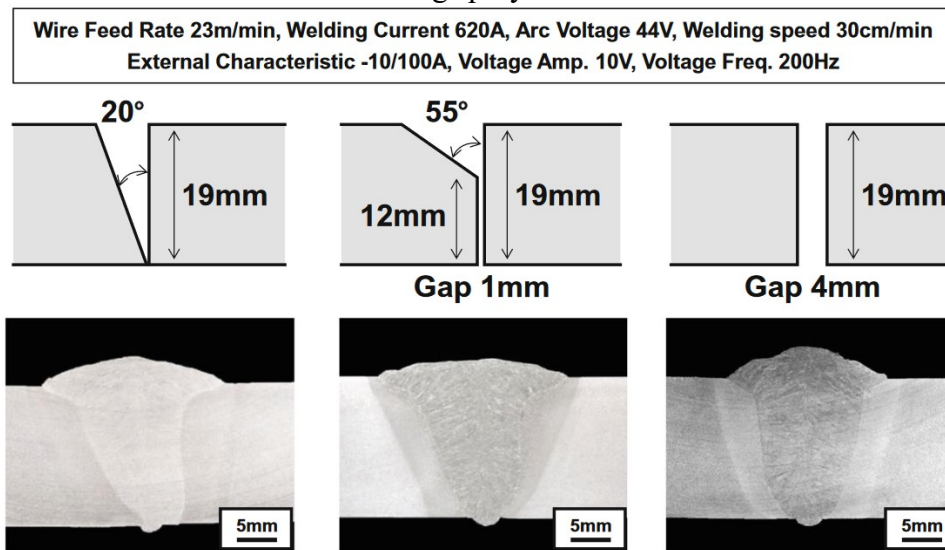
Source: (BABA *et al.*, 2017)

Figure 2.25: Single pass GMAW of 19 mm thick ASTM A36 steel with alternated projected and rotating spray buried arc.



Source: (BABA et al., 2017)

2.3 HYBRID LASER-GMA WELDING

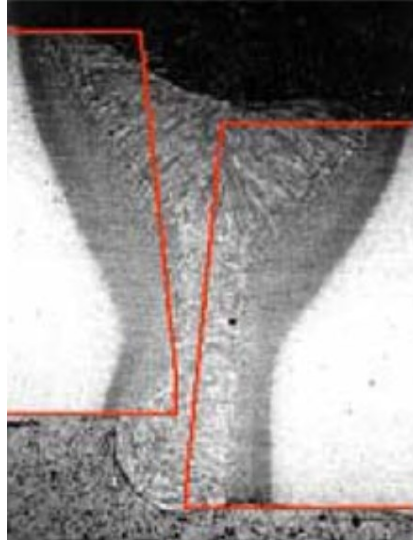
Hybrid laser-arc welding (HLAW) is the combination of laser beam welding (LBW) and arc welding into a single process. It was first developed by Steen and his team (STEEN; EBOO, 1979) in the 1970's, when gas tungsten arc welding (GTAW) was used in conjunction with a 2 kW CO₂ laser.

HLAW is defined when one or more laser beams act in the same molten pool as one or more welding arcs (DVS, 2018; KAH, 2012), although some authors suggest considering hybridization even if the heat sources actuate in different pools (MAHRLE; BEYER, 2006; OLSEN, 2009). The nomenclatures “arc augmented laser welding” and “laser enhanced arc welding” can also be used, where the first indicates that most of the welding energy comes from the laser and the second is used when the arc is the major heat source. However, HLAW is the most general and most often used term (DOWDEN; SCHULZ, 2017; KAH, 2012).

Compared to LBW, HLAW allows deeper penetration, higher welding speed, is less prone to porosity and hot cracking, easier processing of highly reflective materials and has better gap and misalignment tolerance (AKSELSEN; REN; AAS, 2014; DOWDEN; SCHULZ, 2017; FELLMAN; SALMINEN, 2007; KAH, 2012; OLSEN, 2009; PETRING; FUHRMANN, 2004). This last characteristic is exemplified in Figure 2.26, where a joint with 2 mm misalignment is welded by HLAW (PETRING; FUHRMANN, 2004). The presence of a gap can even be beneficial, as deeper penetration and better filler metal mixing are possible, provided the

filler metal feed rate is enough to completely fill the joint (FELLMAN; SALMINEN, 2007). A narrow V-joint can also be used for the same benefit (NILSSON et al., 2003).

Figure 2.26: Hybrid laser-GMA welding of 10 mm thick API 5L X52 steel with 2 mm misalignment.

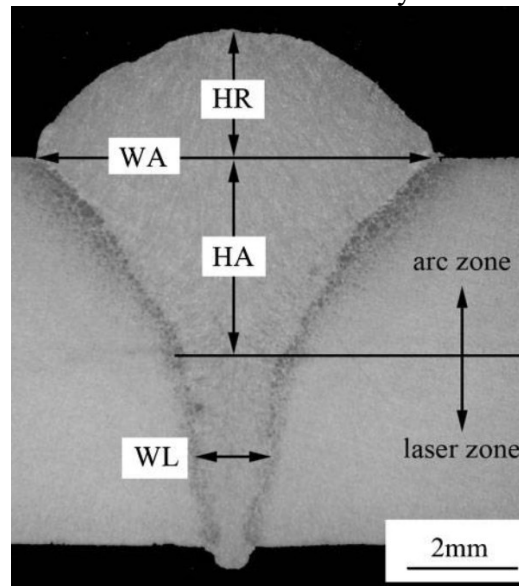


Adapted from: (PETRING; FUHRMANN, 2004)

Different arc processes have been studied in HLAW, including GMAW, GTAW, PAW and SAW, although this last one has limited application (DOWDEN; SCHULZ, 2017; KAH, 2012; MAHRLE; BEYER, 2006; REISGEN et al., 2012). Since the addition of filler metal is usually desirable as it improves gap tolerance and can change the weld metal composition, GMAW is the most common arc process found in HLAW (FELLMAN; SALMINEN, 2007). To achieve higher deposition, the spray transfer mode is most often used, although short-circuiting and pulsed modes are also possible for reduced heat input (ERIKSSON; POWELL; KAPLAN, 2013; KAH, 2012). Hybridizations with GTAW or PAW can be more suitable for thin materials (under **3** or **4 mm** thick) (AKSELSEN; REN; AAS, 2014; BAGGER; OLSEN, 2005; KAH, 2012).

The resulting weld from the HLAW process generally assumes a wine cup shape with a wider region dominated by the arc parameters, the **arc zone**, and a narrower deeper region linked to the laser beam penetration, the **laser zone**, as shown in Figure 2.27. The geometry will also depend on the laser-arc energy ratio (GAO et al., 2008; KAH, 2012). In deep laser zones, adequate filler metal mixing is hard to achieve (FELLMAN; SALMINEN, 2007; KAH, 2012).

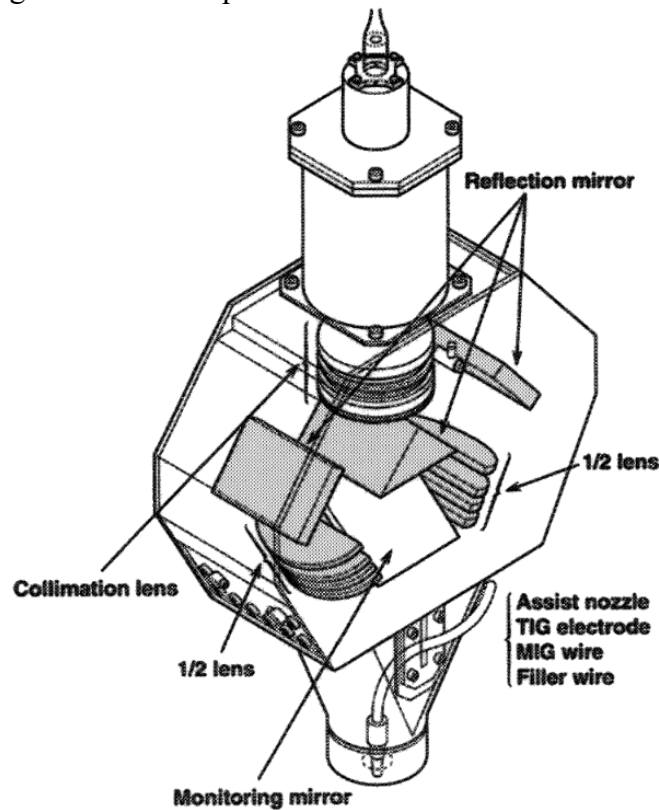
Figure 2.27: Arc zone and laser zone in a hybrid laser-GMA weld.



Source: (GAO et al., 2008)

Typically, the laser beam is aimed perpendicularly to the plate and the arc torch inclined interacting close to the laser beam in a serial configuration (KAH, 2012). However, there are also coaxial solutions, such as the one found in Figure 2.28, a HLAW head in which the beam is split in two around the electrode (ISHIDE; TSUBOTA; WATANABE, 2003). Although the coaxial configuration has the advantage of omnidirectional welding (the process performs equally in every direction), the highest penetration is obtained in a serial configuration (CHEN et al., 2006) and other limitations are found, such as reduced beam quality (ISHIDE; TSUBOTA; WATANABE, 2003; KAH, 2012).

Figure 2.28: Example of a coaxial HLAW head solution.



Source: (ISHIDE; TSUBOTA; WATANABE, 2003).

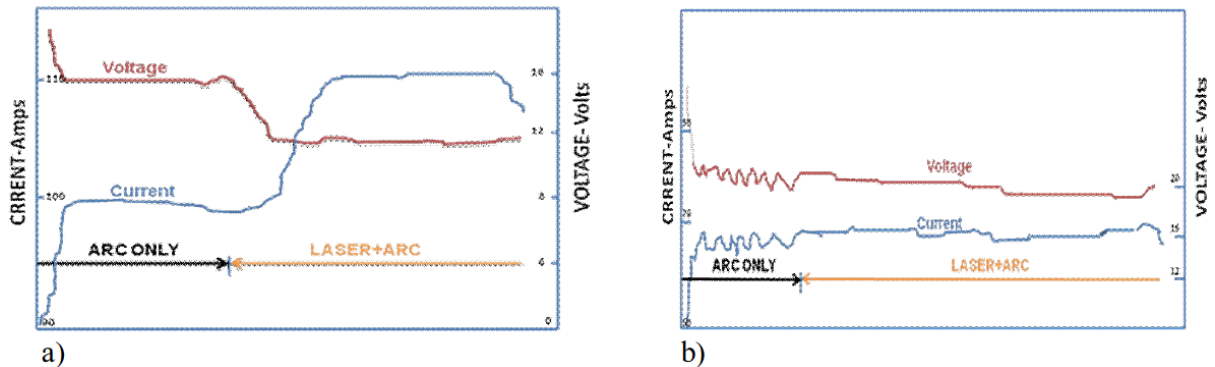
In a serial configuration, the order and the distance between both sources are important parameters added to the process. The choice between a leading or a trailing arc torch depends on many factors, such as laser type, power level, material being welded and arc parameters. However, a leading arc provides better shielding gas coverage and the trailing arc leads to wider pools, less susceptible to undercutting generally (FELLMAN; SALMINEN, 2007). The optimal laser-arc distance (D_{LA}) is usually around **2 mm**, measured from the points where the electrode and the laser beam intercept the base metal, but this value will also vary for different welding conditions (BUNAZIV et al., 2015). The correct relative positioning of the heat sources for each welding condition is important, since the complex interactions and synergies between the laser beam and the electric arc can lead to very different results if their order and distance are changed.

2.3.1 Laser-Arc Interaction

In the first works on HLAW by Steen and Eboo (STEEN, 1980; STEEN; EBOO, 1979) it was already observed that there was interaction between the laser beam and the electric arc. The most notable effects were arc constriction, arc stabilization, arc anchoring and a reduction in arc impedance. Figure 2.29 shows the variation in arc impedance and its stabilization when

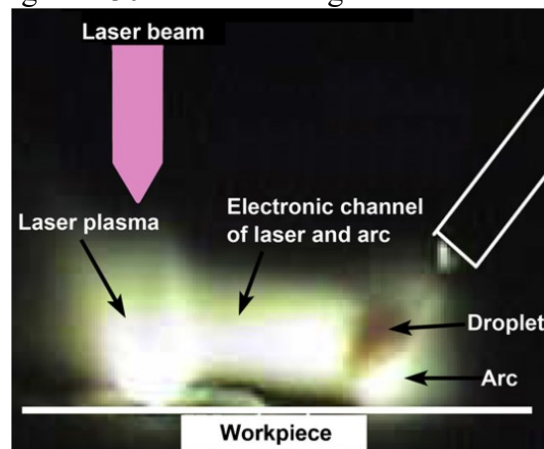
a low power laser beam shone on a GTAW arc. The anchoring effect can be quite pronounced, such as in the case from Figure 2.30 (SUGINO et al., 2005), and has been used to fix wandering arcs, for example, in low current GTAW of mild steels (HU; OUDEN, 2005a), in GMAW of copper (WANG et al., 2017), in GMAW of steels with pure Ar or He shielding gases (OLSEN, 2009) and in GMAW of titanium (SHINN; FARSON; DENNEY, 2005).

Figure 2.29: Arc impedance reduction and stabilization in HLAW.



Source: (STEEN, 1980)

Figure 2.30: Arc anchoring effect in HLAW.



Source: (SUGINO et al., 2005)

Many phenomena have been proposed to explain the interactions observed between laser beam and arc, but it is still not clear which are most significant and how they affect the process under different conditions. Some of these phenomena are presented below and will be further discussed:

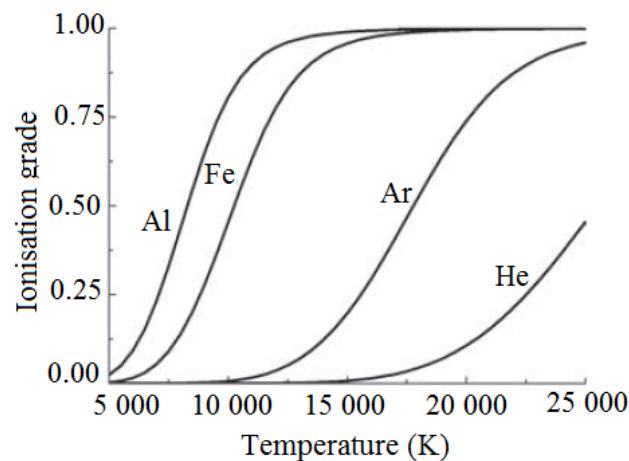
- Metallic vapors;
- Pool depression;
- Arc plasma heating;
- Thermionic emission;

- Pre-heating
- Optogalvanic effect; and
- Other phenomena.

2.3.1.1 Metallic Vapors

Metals have lower ionization potential than noble gases, that is, they reach higher ionization grades at lower temperatures, as depicted in Figure 2.31. In HLAW, the laser beam induces metallic evaporation, which enriches the arc plasma with metallic vapors. The increased density of charge carriers resulting from the higher ionization grade reduce the arc impedance, leading to different effects. For constant voltage welding sources, higher current is expected, while the voltage drop should be reduced in a constant current source. In both cases the arc constricts due to thermal pinching effect, increasing current density. Arc anchoring is also possible, as the electric arc follows the metal vapor rich low impedance laser vapor capillary outlet (HU; OUDEN, 2005b; KUTSUNA; CHEN, 2003; OLSEN, 2009; STEEN; EBOO, 1979). Measurements have confirmed the increased electron density in the arc (CHEN et al., 2018; LIU; CHEN, 2011; LIU; HAO, 2008; RIBIC; BURGARDT; DEBROY, 2011), however, the electron temperature has been shown to both increase (CHEN et al., 2018; RIBIC; BURGARDT; DEBROY, 2011) and decrease (CHEN et al., 2018; LIU; HAO, 2008) in HLAW for different welding conditions.

Figure 2.31: Ionization grade as a function of temperature for Al, Fe, Ar and He.



Source: (OLSEN, 2009)

Occurrences have also been observed where the arc impedance increased because of an interacting laser beam (CAI et al., 2016; ERIKSSON; POWELL; KAPLAN, 2013; LIU; CHEN, 2011). In the work from Eriksson *et al* (2013) the reduced current with the addition of

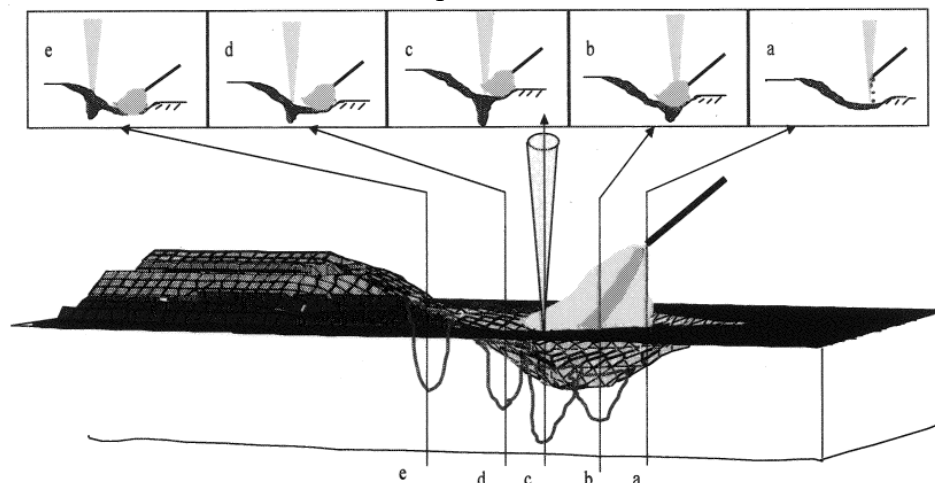
a 3 kW fiber laser beam in a constant voltage GMAW was attributed to disturbances in the shielding gas due to the ejected vapor. For Liu and Chen (2011), the reduction in current occurred when the high speed ejected vapor jet crossed the arc's path, causing the arc to expand and reduce the electron density.

2.3.1.2 Pool Depression

If sufficient current is provided to the arc welding process, arc forces will cause a depression on the molten pool surface (HU; TSAI, 2007; MENDEZ; EAGAR, 2000, 2003; ROKHLIN; GUU, 1993), as exposed in section 2.2.1.

Correct positioning of the laser regarding the pool depression is important for optimal penetration. Neglecting other interaction phenomena, the closer the beam is to the deepest point of the pool depression, the deeper is the total weld penetration (KUTSUNA; CHEN, 2003; OLSEN, 2009). Figure 2.32 illustrates the behavior of weld penetration as the laser-arc distance is varied, with an optimum in the (c) position. If the distance is further reduced, the laser may interact with the filler metal (a) or be affected by the plasma shielding effect (in case of $10\ \mu\text{m}$ wavelength laser) (b). As the distance increases from the optimum, the depression becomes shallower and thus penetration is reduced (d), reaching a point where the depression gives place to a crown reinforcement (e) and penetration can be lower than autogenous LBW.

Figure 2.32: Weld penetration variation at different beam interaction points within the pool depression.



Source: (KUTSUNA; CHEN, 2003)

Since the interaction point of the laser on the surface varies with the pool depression and the depression shape varies with the arc welding conditions, different laser beam focal po-

sitions (f) are necessary to maintain optimal penetration. For example, at higher welding currents, the pool depression tends to be deeper and the focal position should usually be lowered as a consequence (KUTSUNA; CHEN, 2003; MATSUDA et al., 1988; OLSEN, 2009).

The pool depression was found to be slightly deeper in hybrid laser-GMA welding as compared to GMAW alone (LE GUEN et al., 2011).

2.3.1.3 Arc Plasma Heating

As discussed in section 2.3.1, light interacts with plasmas. In hybrid laser-arc welding, the absorption of the laser beam by the arc plasma through inverse Brehmstrahlung can be quite significant for **10 μm** lasers, increasing the arc's temperature, leading to higher ionization grade and, thus, reduced impedance. On the other hand, less laser power reaches the workpiece. This effect is negligible for **1 μm** lasers (DOWDEN; SCHULZ, 2017; HU; OUDEN, 2005b; RIBIC; RAI; DEBROY, 2008; SEYFFARTH; KRIVTSUN, 2002).

Startsev *et al.* (2000) studied this phenomenon through numerical simulation of a coaxial hybrid laser-GTAW process with a hollow cathode through which the laser beam passes. Arc's core temperature increased from **10,000-12,000 K** for **50-200 A** without laser to **18,000-21,000 K** with a **1.5 kW** CO₂ laser. For **100 A**, the current density at the anode increased from **7·10⁶ Am⁻²** to **4.5·10⁷ Am⁻²** and the voltage drop in the arc column decreased by **25-50 %**.

2.3.1.4 Thermionic Emission

At sufficiently high temperatures, electrons are emitted with a current density (J) given by the Richardson-Dushman Equation (2.12), as below. A_R is the constant of Richardson (A/m²K²), T the temperature (K), k_B the constant of Boltzmann (**8.6173x10⁻⁵ eV**) and W_e is the working function of the material (eV), which is the energy the electron has to overcome to be emitted (LANCASTER, 1984; STUTE; KLING; HERMSDORF, 2007).

$$J = AT^2 \cdot e^{\frac{-W_e}{k_B T}} \quad (2.12)$$

Thermionic emission has been a suspected phenomenon in arc stabilization since Steen and Eboo (1979) observed that a laser heating a titanium plate from the opposite side of the arc could anchor it, provided the laser power was sufficient to heat the opposing surface (where the GTAW arc acted) to at least **400 °C**. Ono *et al.* (2003) also consider the thermionic emission an important factor.

Through Equation (2.12), Stute *et al.* (2007) estimated that a surface temperature of **2200 °C** would be needed for thermionic emission to produce prominent current density in aluminum. Their experiments showed that arc stabilization happened even at measured surface temperatures of **1200 °C** and then concluded that thermionic emission was not a main factor in arc stabilization. However, the calculated temperature is still below the boiling point of aluminum, so at higher laser powers and for different materials, the thermionic emission could still be significant. Seyffarth and Krivtsun (2002) also dispute the significance of thermionic emission for arc stabilization.

2.3.1.5 Pre-Heating

The pre-heating provided by the arc can lead to increased laser penetration due to increased absorptivity in hotter metals and due to the higher energy input, which reduces the required energy provided by the laser to penetrate the material (BUNAZIV *et al.*, 2015; DILTHEY; WIESCHEMANN, 2000; KAH, 2012). This effect is more important for highly reflective metals (KAH, 2012) and more pronounced in a leading arc configuration (BUNAZIV *et al.*, 2015).

2.3.1.6 Optogalvanic Effect

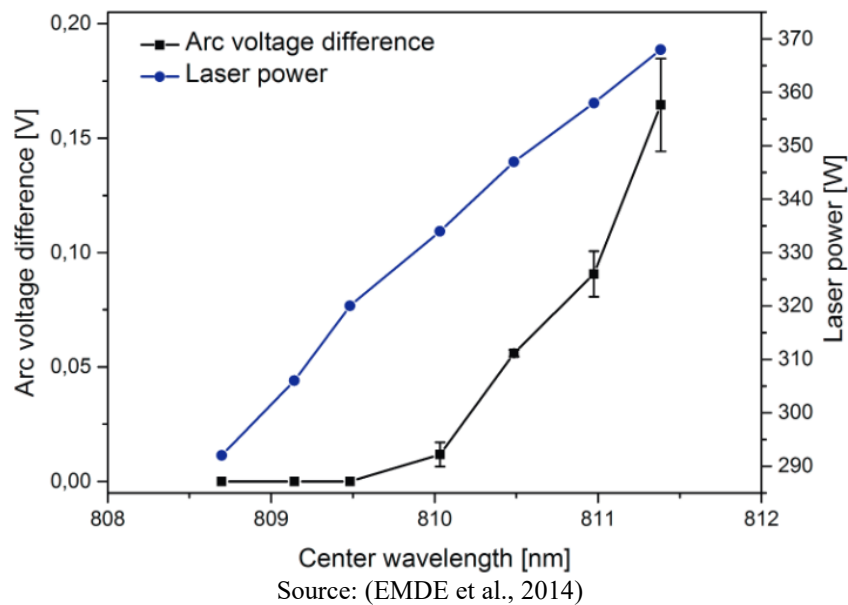
The optogalvanic effect is the change in impedance of a gas discharge (e.g. electric arc) caused by the incidence of photons which resonate with one or more atomic or molecular quantum transitions (BARBIERI; BEVERINI; SASSO, 1990). It was first described by Pennin (1928) and has found applications in spectroscopy (BARBIERI; BEVERINI; SASSO, 1990).

In HLAW, if the laser photons match the transition energy of one of arc plasma components, the optogalvanic effect takes place, increasing the population of higher energy states, which can be more easily ionized by secondary processes and thus reducing arc impedance (EMDE *et al.*, 2014; KOZAKOV *et al.*, 2015; STUTE; KLING; HERMSDORF, 2007). Stute *et al.* (2007) even consider it to be the most important interaction phenomenon between arcs and continuous wave lasers.

The optogalvanic effect is, however, strongly dependent on the wavelength matching between the photon and the absorption lines of the plasma components. Emde *et al.* (2014) tested the effect of resonant and non-resonant beams on a GTAW arc using a tunable diode laser with a linewidth of **2.5 nm** and **367 W** max power crossing the arc transversely, so that it would not interact with the substrate. The laser wavelength was varied from **808.1 nm** to **811.3 nm**. Figure 2.33 shows the arc voltage reduction as a function of the wavelength. As the wavelength approaches **811.3 nm**, both argon absorption lines of **810.4 nm** and **811.5 nm** are

excited and the voltage reduction increases. The resonant beam attenuation was measured to be around **16 %** in this configuration, while the non-resonant beam attenuation was negligible. In a later work (EMDE et al., 2016), this time with the beam irradiating on the substrate, it was found that the resonant beam had an increased effect on arc luminosity, indicating higher ionization grades, but the resonant and the non-resonant beams were equally effective at arc anchoring.

Figure 2.33: Arc voltage reduction due to the optogalvanic effect as a function of laser wavelength.

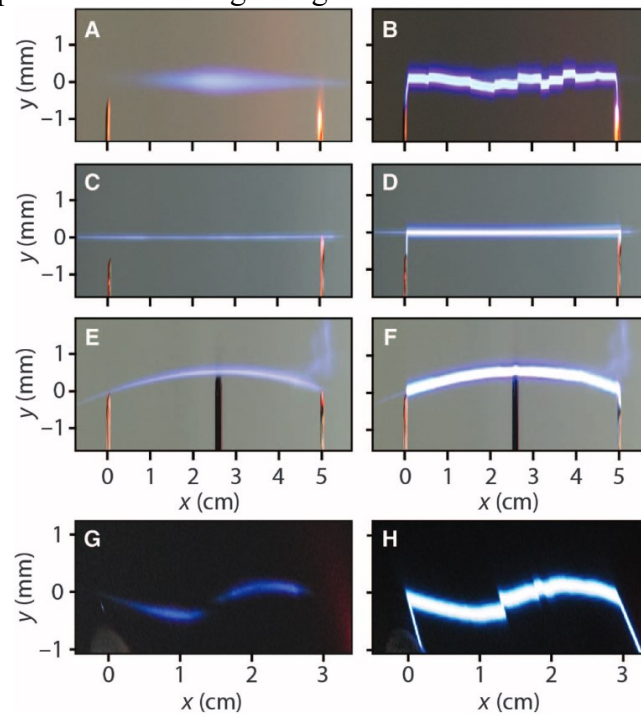


No study was found in the literature regarding the optogalvanic coupling between the wavelengths of typical welding lasers and common shielding gases or other arc plasma components.

2.3.1.7 Other Phenomena

The photon energy of infrared and visible lasers is not sufficient to cause direct ionization. However, in the case of extremely high intensities, multiple photons can be simultaneously absorbed and lead to the multiphoton ionization phenomenon. This phenomenon has been shown to guide electric arcs when using a femtosecond pulsed laser, as in Figure 2.34, which shows on the left the gas ionized by the laser and on the right the electric arc following the previously ionized path (CLERICI et al., 2015). For the time being, no continuous wave lasers reach the required intensities required for the multiphoton ionization phenomenon to be relevant, so it is still not observable in HLAW.

Figure 2.34: Multiphoton ionization guiding electric arcs in different beam configuration.



Source: (CLERICI et al., 2015)

Scattering is also present as the laser beam crosses the arc, being the Rayleigh scattering and the Mie scattering the most significant for HLAW (DOWDEN; SCHULZ, 2017).

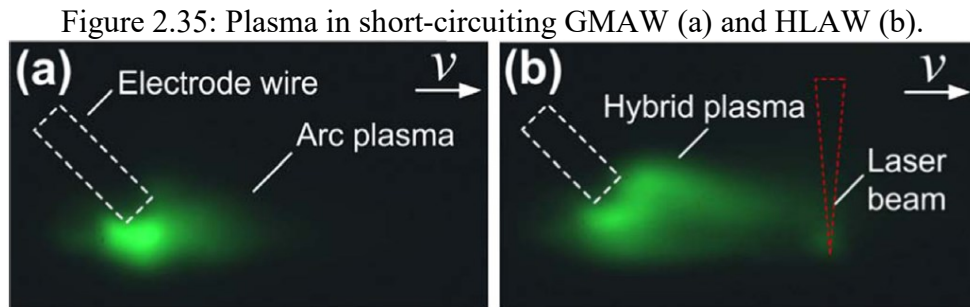
2.3.2 Metal Transfer in Hybrid Laser-GMA Welding

Since the laser beam can influence the geometric and electromagnetic properties of the arc, changes in wire metal transfer in HLAW are expected. It has been observed that the magnitude and direction of the electromagnetic force and the plasma drag force can change by arc interaction with a laser beam and it might promote or hinder metal transfer (CAI et al., 2016). The laser influence on the metal transfer for short-circuiting, globular and spray modes will be respectively discussed.

2.3.2.1 Short-Circuit

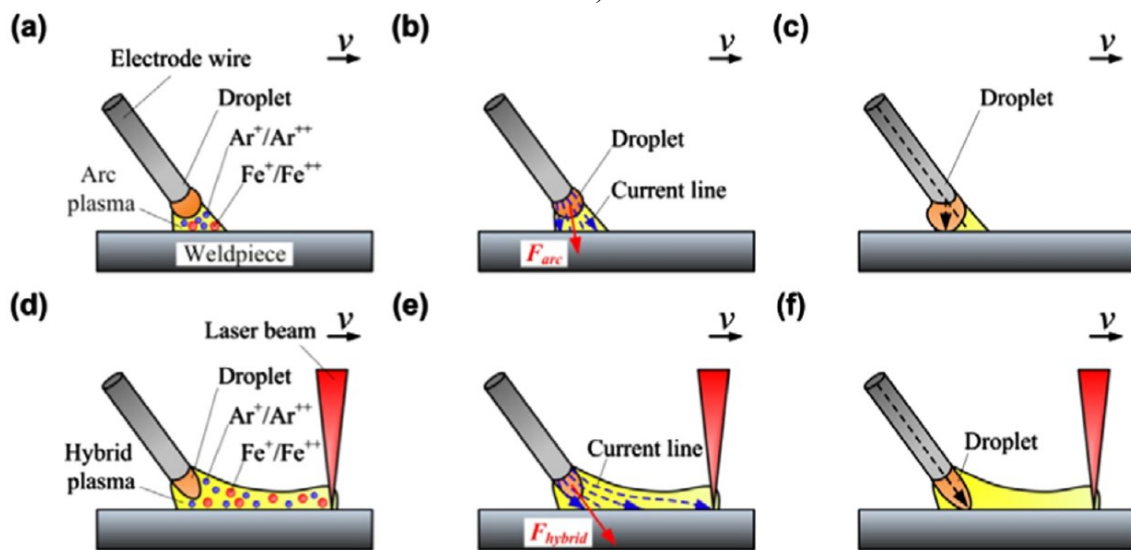
When a laser beam is applied onto a short-circuiting GMAW, the open arc phase tends to decrease and the transfer frequency to increase (CAI et al., 2016; ONO et al., 2002). Cai *et al.* (2016) observed a **70 %** increase in transfer frequency when a **3 kW** fiber laser was used **4 mm** apart from the arc. Peak current reduction was also noticeable, leading to a more stable molten metal transfer. Similar behavior was noticed by Ono *et al.* (2002), with a **3 kW** Nd:YAG laser, where the open arc phase decreased from **50-100 ms** to **10 ms**. Figure 2.35 shows plasma images for GMAW (a) and for HLAW (b). As can be seen, the laser leads to a much wider arc

that engulfs the electrode tip, increasing the magnitude of the electromagnetic force due to a more divergent current flow at the droplet, which promotes its earlier contact with the molten pool. The schematics in Figure 2.36 explain this difference between GMAW (a, b and c) and HLAW (d, e and f) and also shows that the force direction also changes (CAI et al., 2016).



Source: (CAI et al., 2016)

Figure 2.36: Electromagnetic force in short-circuiting GMAW (a, b and c) and in HLAW (d, e and f).



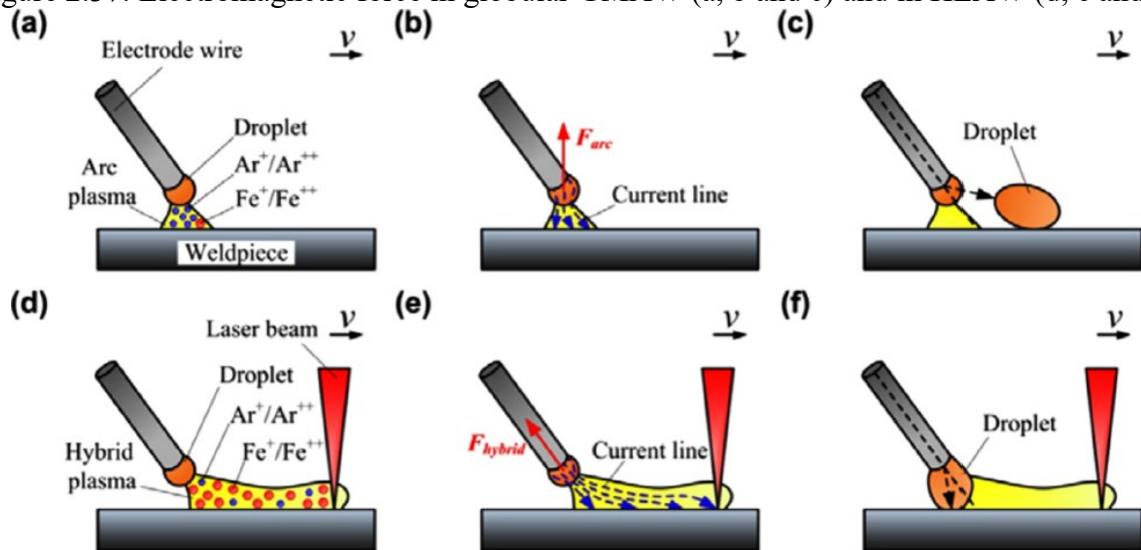
Source: (CAI et al., 2016)

A different behavior was observed by El Rayes *et al.* (2004), where the short-circuit frequency was reduced as the laser power increased from 4 kW to 9 kW. This phenomenon was attributed to the reduced ionization potential of the metallic vapor, which resulted in increased average current as the laser power increased. The difference to the previous cited works might be due to the He based mixture (high ionization potential) shielding gas and high interacting CO₂ laser used by El Rayes *et al.* (2004), so the current increase should be more prominent under these conditions and dominate the short-circuit frequency influence. The HLAW was not compared to the sole GMAW process either, only at different laser powers.

2.3.2.2 Globular

In globular GMAW, the arc attaches into a narrow anode zone under the droplet and cause a repulsive upward force that hinders its detachment. As the arc anchors to the vapor capillary in HLAW, it reaches the droplet sideways (on the front if the laser is leading, and on the back if the arc is leading). Therefore, the repulsive force has a sideway component and a smaller upward component, as depicted in Figure 2.37. This leads to higher transfer frequency and may also change the metal transfer to a short-circuiting mode (CAI et al., 2016; LEE et al., 2005).

Figure 2.37: Electromagnetic force in globular GMAW (a, b and c) and in HLAW (d, e and f).



Source: (CAI et al., 2016)

The vapor jet leaving the vapor capillary can act as a hindering force however. Liu *et al.* (2012) observed a reduction in droplet detachment frequency as D_{LA} was reduced and the vapor jet interacted with the droplet. The transfer mode was also changed from projected spray to a globular mode. Lei *et al.* (2017) showed through numerical models and high-speed imaging that the droplet detachment critical size can increase with laser power, mostly due to the vapor jet drag force.

2.3.2.3 Spray

Cai *et al.* (2016) observed that the laser presence hindered the droplet detachment in the spray mode, reducing the detachment frequency from **436 Hz** to **313 Hz** in their work. This reduction was attributed to the reduced current caused by the presence of metallic vapor in the plasma, from **289 A** to **274 A**. However, it is not clear if the reduced current is the only factor

influencing the transfer frequency, since other phenomena can be equally or more important, such as the arc contraction.

The laser beam can also influence the droplet trajectory. It has been shown that the droplets path can be deflected upward from the wire axis in the leading arc (pulling torch) condition and downward in the leading laser (pushing torch) condition (BUNAZIV et al., 2018a; CAI et al., 2016; FELLMAN; SALMINEN, 2007). The former configuration can lead to process instability and porosity, since the droplet is deflected towards the laser vapor capillary and can disturb it (CAI et al., 2016; CAMPANA et al., 2007). The droplet deflection was found to be stronger for higher arc power, shorter arc length and smaller droplets (BUNAZIV et al., 2018a).

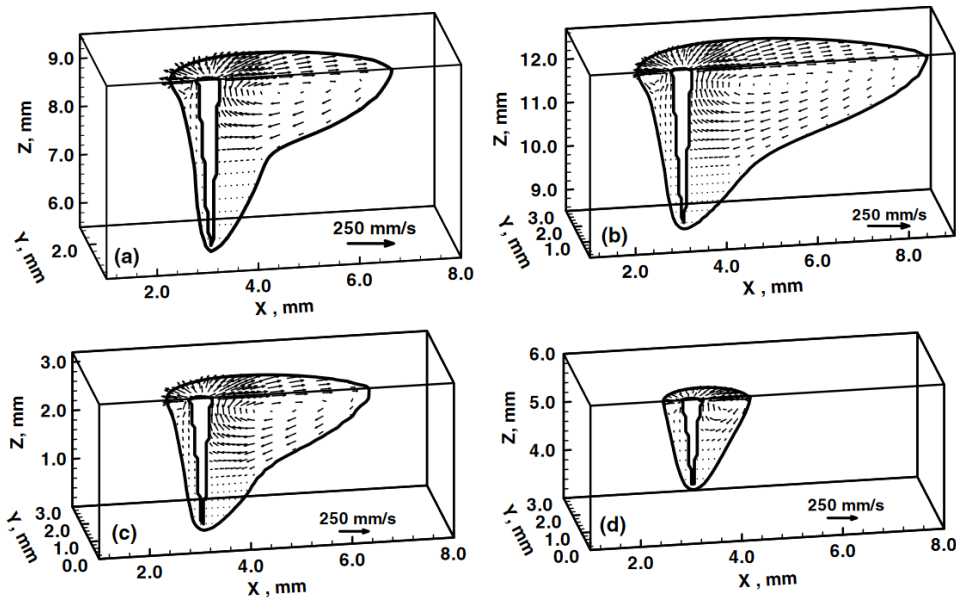
In general, the free flight transfer modes (spray and pulsed arc) are preferred over globular and short-circuiting due to being more stable (CAMPANA et al., 2007). The CMT technology can also be a solution when lower currents are desired (FROSTEVARG, 2016).

2.3.3 Pool Dynamics

In penetration mode LBW, the Marangoni force dominates the convective flow due to high thermal gradient between the laser heated vapor capillary surface and rapid cooling pool backside. For most welding conditions, the Marangoni force produces a rapid backward flow on the surface away from the vapor capillary, which then turns inwards and forwards near the solidification front in order to maintain mass conservation. The resulting flow pattern is characterized by high flow speeds near the welding surfaces and slow flows on the inside (ARTINOV et al., 2018; RAI et al., 2007). Figure 2.38 shows the numerical simulated pool flow for stainless steel, titanium, vanadium and tantalum welding with **1900 W** Nd:YAG laser at **0.76 m/min** welding speed (RAI et al., 2007).

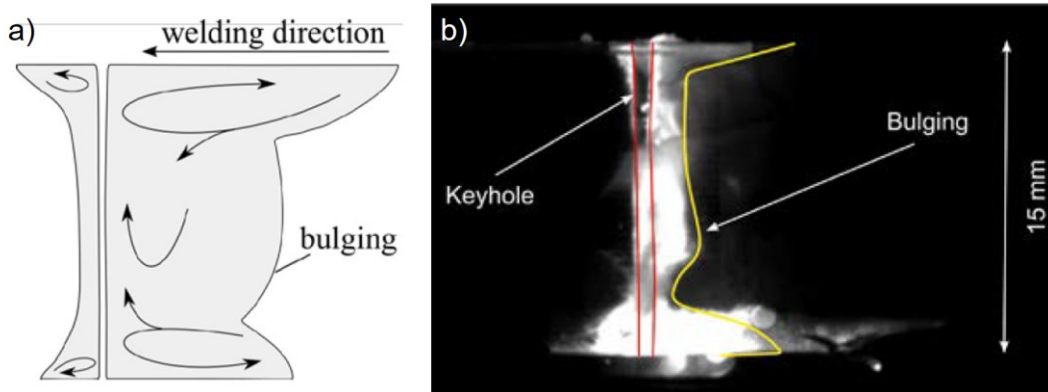
For fully penetrating welds, the Marangoni force produces the same convection pattern on the root side, so that there is two main circulation vortexes, as seen in Figure 2.39 a) (ARTINOV et al., 2018). These circulation vortexes carry cold material from near the solidification front towards the vapor capillary right below the surface, causing the region to cool faster and produce a necking on the molten pool, while the central region is unaffected by the colder metal and cools slower, resulting in a heated bulge, demonstrated in Figure 2.39 b) (ARTINOV et al., 2018; BAKIR et al., 2018). The last to solidify bulging region has been observed to be related to solidification cracking defects (BAKIR et al., 2018; BARBETTA, 2014).

Figure 2.38: Molten pool shape and flow for (a) 304L stainless steel, (b) Ti-6Al-4V, (c) vanadium and (d) tantalum.



Source: (RAI et al., 2007)

Figure 2.39: Fluid flow in fully penetrating welds (a) and necking and bulging regions on the pool (b).

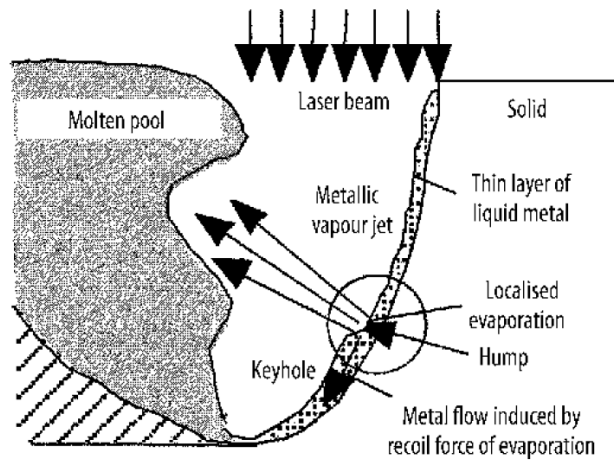


Adapted from: (ARTINOV et al., 2018)

In the vapor capillary region, other phenomena exert important influence on the molten pool dynamics, namely the vaporization recoil force and the vapor jet.

The vapor capillary front wall has been observed to be rugged, with humps that move downwards. The upper part of each hump is nearly perpendicular to the beam propagation direction, thus it is a region of higher beam absorption and increased vaporization. The localized vaporization recoil pressure leads to humping growth and produces fast downward flow on the front wall, while the concentrated vapor jet can interact with the capillary back wall (BERGER et al., 2011; ERIKSSON; POWELL; KAPLAN, 2011; MATSUNAWA, 2002; ROMINGER et al., 2010). The schematic in Figure 2.40 illustrates this behavior.

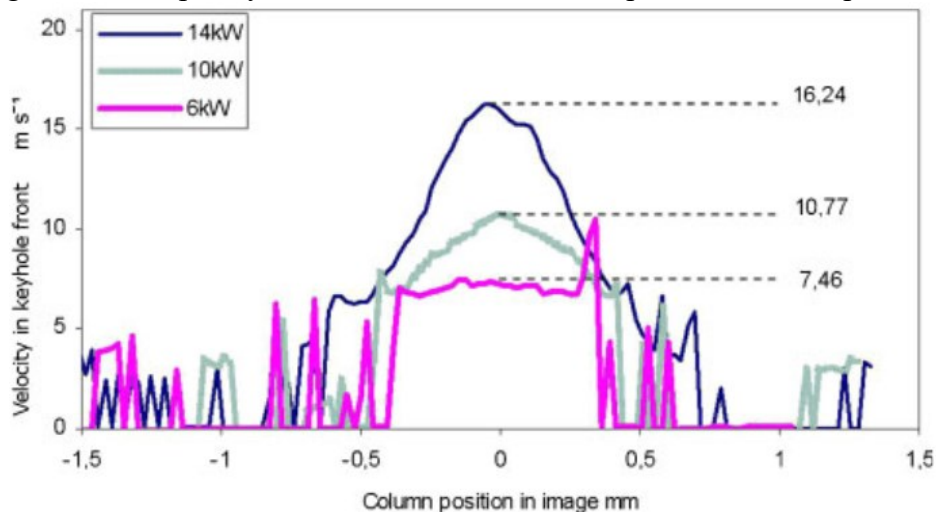
Figure 2.40: Pool behavior inside the vapor capillary.



Source: (MATSUNAWA, 2002)

Using high-speed imaging and the streak image technique coupled with fast Fourier transform, Eriksson *et al.* (2011) measured the front wall downward flow in high power fiber laser welding, and found that the flow speed is highest in the wall center and is correlated with beam intensity. 2.41 shows the measured flow speed at different positions on the front wall for three power levels, reaching over **16 m/s** at **14 kW**. It was also reported that the beam wavelength also has a strong influence on the downward flow speed, with solid state lasers (**1 μm**) resulting in faster flows than CO₂ (**10 μm**) lasers due to the higher absorptance of laser light on the hump upper side (HAUG *et al.*, 2013; POWELL *et al.*, 2015; ROMINGER *et al.*, 2010).

Figure 2.41: Capillary front wall downward flow speed at different positions.



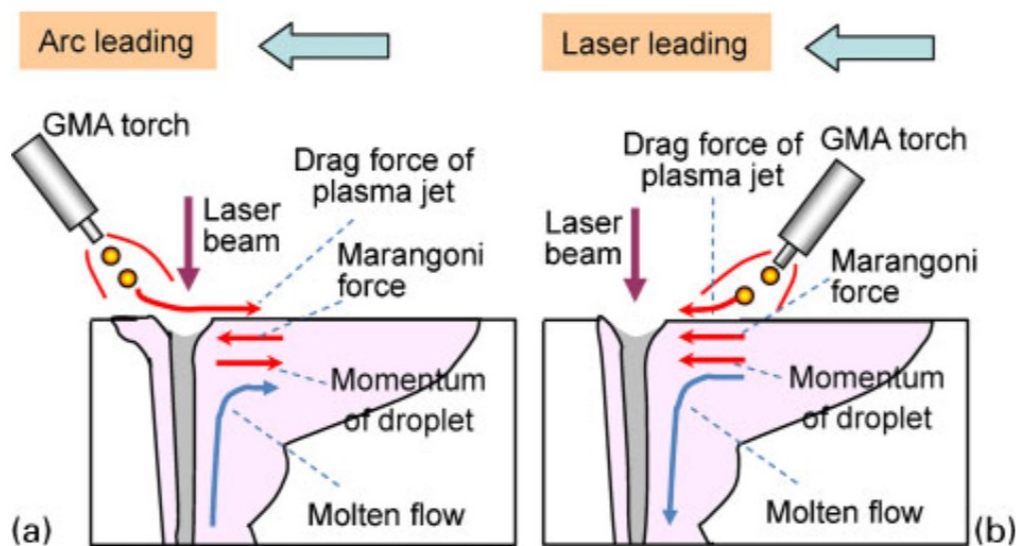
Source: (ERIKSSON; POWELL; KAPLAN, 2011)

The arc addition to the process brings new convection driving forces to the HLAW, most notably the arc shear force and arc stagnation pressure produced by the high-speed plasma

jets, the electromagnetic forces due to divergent current flow inside the molten pool and droplet momentum in the case of GMAW. The resulting fluid flow will depend on many factors, such as the arc parameters, the shielding gas and the heat sources arrangement (BUNAZIV et al., 2018b; NAITO; KATAYAMA; MATSUNAWA, 2003; RIBIC; PALMER; DEBROY, 2009; RIBIC; RAI; DEBROY, 2008; ZHAO et al., 2009).

Heat sources positioning is especially important to the resulting fluid flow in the molten pool, since many driving forces will be in different directions for a leading arc and for a leading laser configuration. As illustrated in Figure 2.42, plasma shear force (or drag force) and droplets momentum point backwards for an arc leading configuration and forward in a laser leading configuration (BUNAZIV et al., 2018b; MURAKAMI; SHIN; NAKATA, 2010; ZHAO et al., 2009). In the present schematics, the Marangoni force is forwards due to the presence of O_2 in the shielding gas, which can lead to positive surface tension temperature coefficient in steels, reversing the force direction (ZHAO et al., 2009).

Figure 2.42: Driving forces in HLAW for arc leading (a) and laser leading (b) with 2 % O_2 content in shielding gas.



Source: (ZHAO et al., 2009)

One of the main advantages of welding with the addition of a filler metal is the possibility to change the weld metal composition in order to obtain better metallurgical properties. In deep penetrating HLAW (and LBW as well), distributing the filler metal along the whole weld depth is not trivial and it tends to concentrate on the upper portion of the weld (CHEN et al., 2017; CHO et al., 2010; LIU; KUTSUNA; XU, 2006; ZHAO et al., 2009).

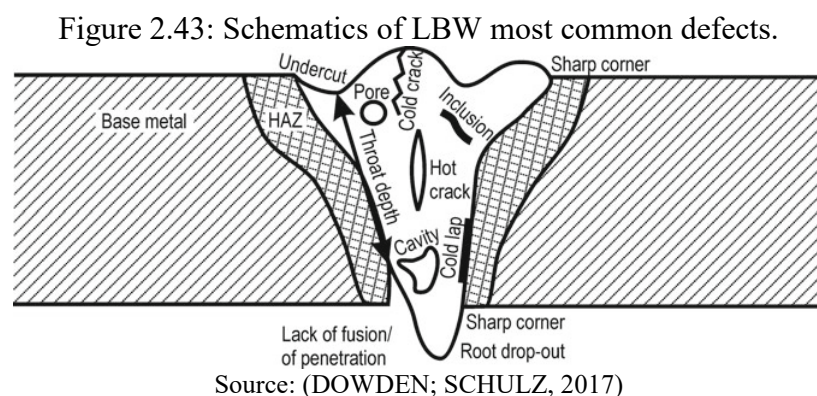
By using a leading laser configuration and by adding at least 2 % O_2 to the shielding gas composition, Zhao *et al.* (2009) promoted a stronger molten pool downward flow that led

to better filler metal dilution at the weld root, see Figure 2.42. Better filler metal distribution can also be obtained by employing wider gaps/joints (FELLMAN; SALMINEN, 2007; ZHAO et al., 2009). Magnetic stirring has also been observed to promote filler metal dilution in aluminum LBW (GATZEN; TANG; VOLLERTSEN, 2011; VOLLERTSEN; THOMY, 2006) and in HLAW of stainless steel (CHEN et al., 2017).

2.3.4 Discontinuities and Defects

Several discontinuities can be found in LBW and in HLAW, including but not limited to the ones illustrated in Figure 2.43 and in the list below (DOWDEN; SCHULZ, 2017; LIENERT et al., 2011; RIBIC; PALMER; DEBROY, 2009):

- Humping;
- Undercut;
- Root humping (sagging, root dropout, root drop-through);
- Solidification cracking;
- Cold cracking;
- Porosity;
- Spatter;
- Lack of penetration;
- Reinforcement excessive convexity;
- Crater cracks;
- Shrinkage grooves.



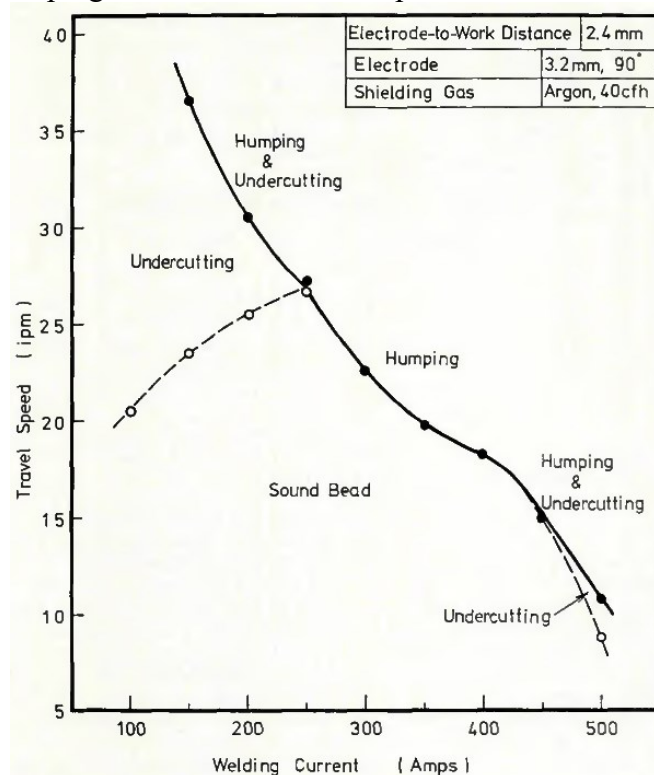
When high current arc welding processes are used, such as in the present work, humping and undercutting are important discontinuities hard to avoid. For this reason, these discontinuities will be discussed more deeply, while other discontinuities will be presented briefly.

Also, since humping and undercutting seem to have some common origins (SODERSTROM; MENDEZ, 2006), they will be discussed together.

2.3.4.1 Humping and Undercutting

Bradstreet (1968) was among the first to study both humping and undercutting phenomena in GMAW and linked it to high welding speeds. It was also noticed that a pushing torch would suppress humping development, while oxygen exacerbated the problem. Savage *et al.* (1979) carried an extensive work to map humping and undercut formation critical welding speed in GTAW for different currents, shielding gases, electrode-to-work distances, electrode geometry and other factors, while also measuring arc force. One map for critical welding speed as a function of welding current is presented in Figure 2.44.

Figure 2.44: Humping and undercut critical speeds for different welding currents.

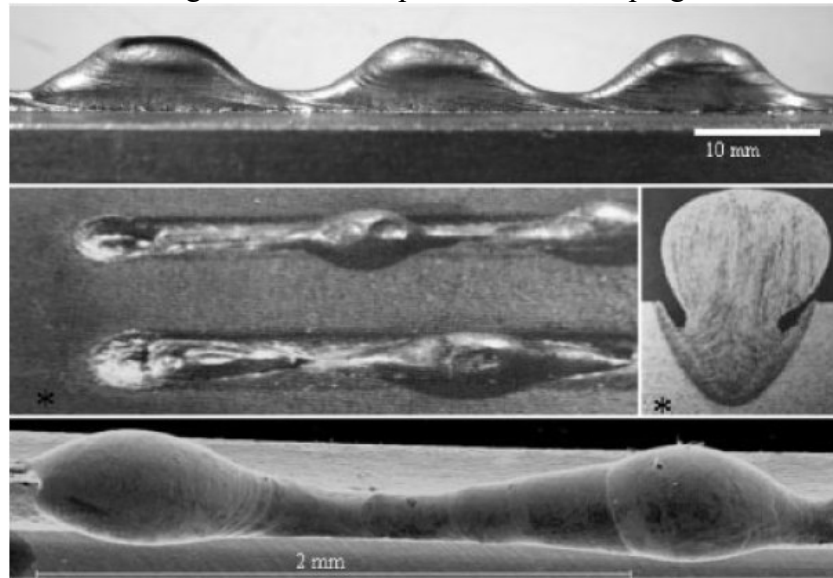


Source: (SAVAGE; NIPPES; AGUSA, 1979)

Humping discontinuities can vary greatly in shape and different phenomena can explain their formation (SODERSTROM; MENDEZ, 2006; WEI, 2010). Soderstrom and Mendez (2006) classified the humping defects into two broad categories based on their morphologies: gouging region morphology (GRM) and beaded cylinder morphology (BCM). Under some circumstances, characteristics of both morphologies can be seen in a single weld.

BCM humps show cyclical beadlike protuberances connected by a narrow central channel, without dry spots and deep depressions, similar to the ones presented in Figure 2.45 (SODERSTROM; MENDEZ, 2006; WEI, 2010).

Figure 2.45: Examples of BCM humping.

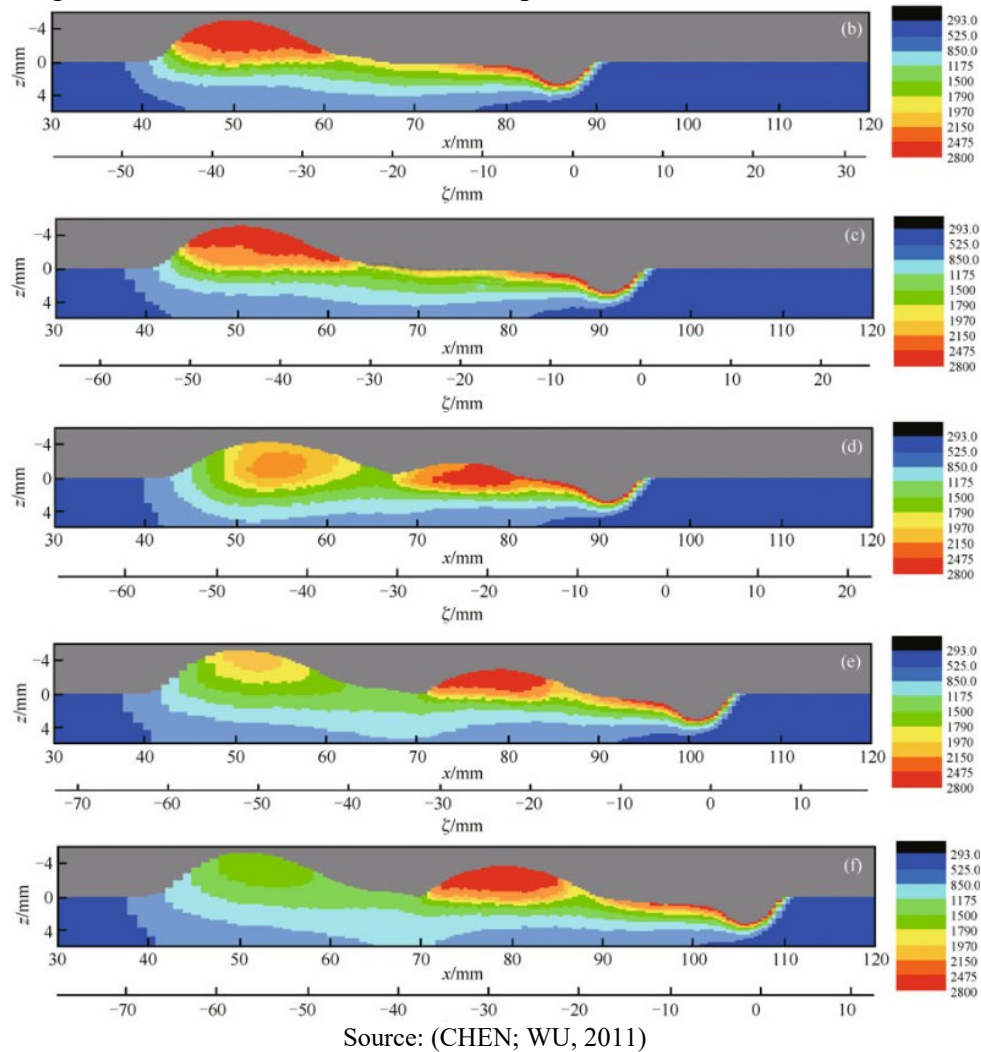


Source: (SODERSTROM; MENDEZ, 2006)

BCM humping might be explained by the Rayleigh capillary instability, which comes from the tendency of a liquid cylinder to break down into spheres in order to reduce surface energy. Gratzke *et al.* (1992) developed a theoretical model to evaluate Rayleigh instability in a partially bounded liquid cylinder (the elongated weld pool) and good agreement was found with experimental results. It was concluded that the governing factor was the width-to-length ratio, which, when below a critical level, humping is observed.

High speed backward flows can also lead to BCM humping formation, as the liquid momentum leads to material buildup on the pool backside. The material is fed through a smaller section in the trailing region of the molten pool, which can solidify as it moves further away from the heat source, cutting the liquid supply to the previous hump and a new hump begins to form. This phenomenon can be seen in the GMAW numerical simulations for **350 A** at **1.5 m/min** welding speed from Chen and Wu (2011), as shown in Figure 2.46, where the color scale refers to the temperature (K) and the interval between **1.5 s** and **2.3 s** after welding beginning is shown.

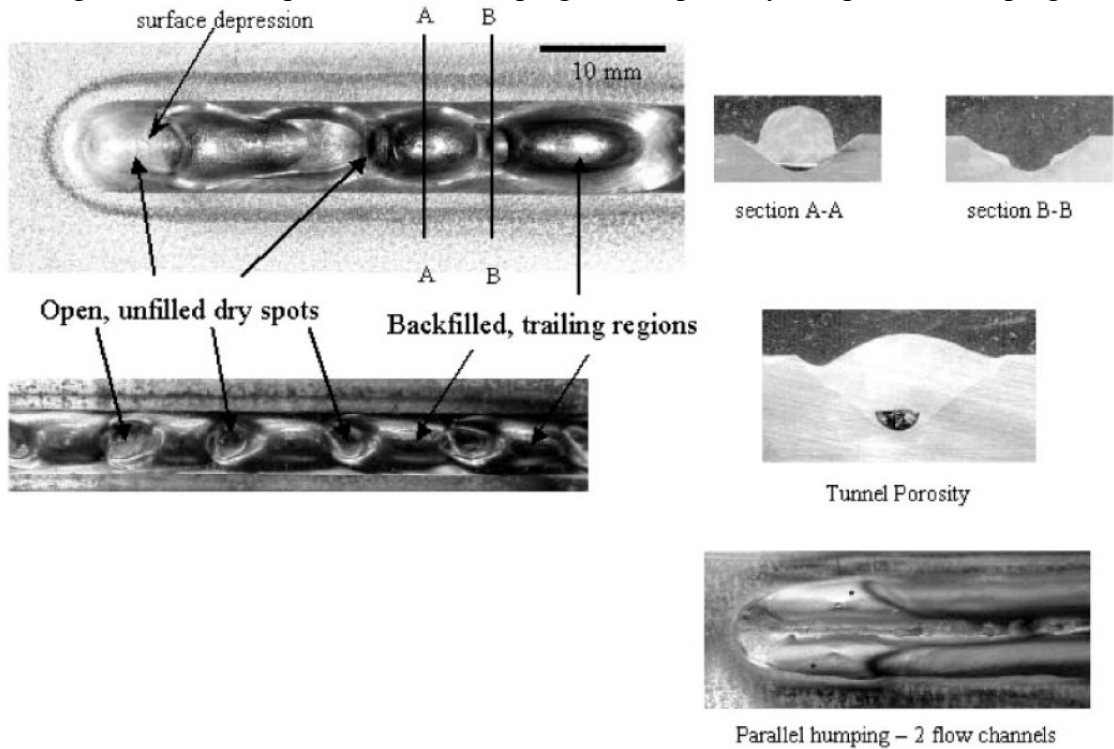
Figure 2.46: Numerical simulated hump formation due to backward flow.



Cho and Farson (2007) explained the BCM humping observed in their numerical simulation and experiments in buried pulsed arc GMAW by a combination of fast backward flow and surface tension induced necking of a long molten pool (Rayleigh capillary instability). At **0.75 m/min** welding speed, the pool was too short for the necking to occur and no humping was observed. However, at **1.5 m/min**, fast backward flow caused the metal to build up at the trailing region of the pool and the necking effect prevented the material to be redistributed along the pool. The necking region solidifies prematurely, and the buildup is left as a hump.

The GRM is characterized by open unfilled dry spots between the hump beads and is linked to the presence of a gouging region in the weld front. Tunnel porosity and split weld beads (parallel humping) are discontinuities that can also be related to GRM humping (SODERSTROM; MENDEZ, 2006; WEI, 2010). Figure 2.47 shows some examples of GRM humping, tunnel porosity and split weld beads.

Figure 2.47: Examples of GRM humping, tunnel porosity and parallel humping.



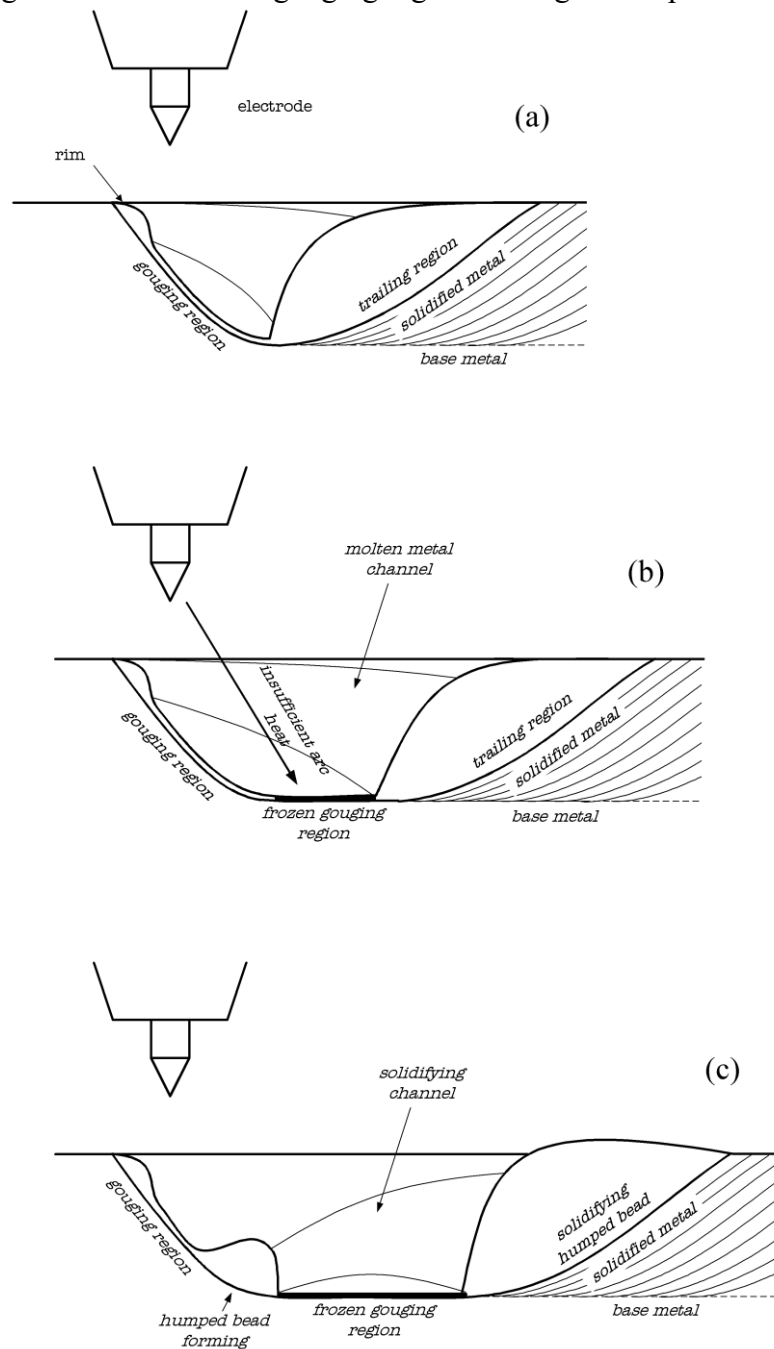
Source: (SODERSTROM; MENDEZ, 2006)

In order to discuss GRM humping, the gouging region behavior must be better understood. As presented in Section 2.2.1, when high arc currents are applied, a gouging region and a trailing region develop due to the high arc forces. The gouging region is characterized by a thin film of molten metal flowing backwards, towards the trailing region. Most of the molten metal flows through the sidewalls, where a rim (or molten channel) can be formed (see Figure 2.19) (MENDEZ; EAGAR, 2000, 2003; MENG; QIN; ZOU, 2016). The deepest point in the gouging region is found lagging behind the electrode due to thermal inertia (MENG; QIN; ZOU, 2016). At the transition point between gouging region and trailing region, conditions might be adequate for the hydraulic jump phenomenon to occur (YAMAMOTO; SHIMADA, 1975).

Due to the molten film small thickness in the gouging region, solidification happens after a few milliseconds in the absence of heat (MENDEZ; EAGAR, 2003; MENG; QIN; ZOU, 2016). Mendez and Eagar (2003) postulated that, if the transition between gouging and trailing regions was positioned outside of the heat source area of influence, it would solidify, leading to possible GRM humping formation. Figure 2.48 illustrates the possible humping phenomenon, comparing a weld where the gouging region is completely heated (a) to one where it solidifies before reaching the trailing region (b) and the trailing region then solidifies as a hump (c). A criterion for humping onset can be defined with a balance of forces (arc pressure against

hydrostatic pressure and capillary pressure) to determine transition position and comparing it to the heated area. The balance of forces can also indicate when the gouging region becomes unstable (no transition point) and split beads and tunnel porosity can form. The calculated transition point is pushed away from the heated area as the arc current is increased, increasing the likeability of humping, split beads and tunnel porosity, in agreement to what is observed experimentally.

Figure 2.48: Solidified gouging region leading to hump formation.

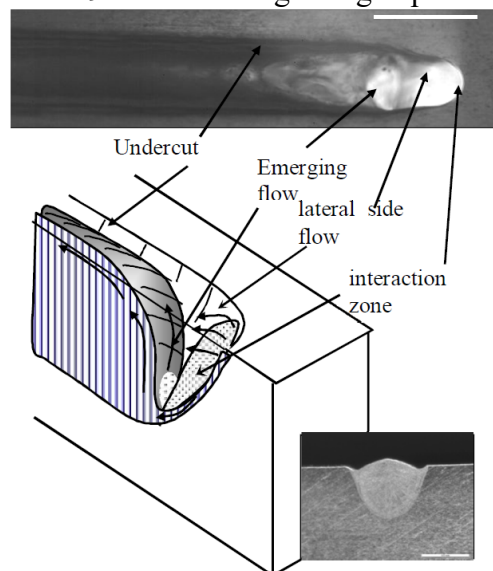


Source: (MENDEZ; EAGAR, 2003)

With numerical simulations supported by welding experiments, Meng *et al.* (2016) observed the premature solidification of the gouging region leading to humping formation. It could also be noted that the sidewalls rims (or molten channels) were the last part of the gouging region to solidify, creating a feeding channel to the trailing region and building up material on the sides of the weld bead. If the molten metal buildup on the sides met before fully solidifying, regular GRM humping (with or without tunnel porosity) could form. If both sides never touched, the results were split beads.

Undercutting might also be related to premature solidification of the gouging region, specifically the uppermost part of the sidewalls. If the thin film solidifies before reaching the trailing region, a solidified depressed area will be formed, which the trailing region might not be able to adequately wet, leaving behind a dent on the bead sides (MENDEZ; EAGAR, 2003; MENG *et al.*, 2016). At the beginning of the trailing region, the metal flows backwards, but an inward (towards the weld centerline) speed component is also observed at high welding currents (at **250 A** and above), which can play a role in undercut formation as well (MENG *et al.*, 2016). A similar condition was also observed in high-speed LBW (**15 m/min** or more) by Fabbro (2010), where the vapor capillary becomes elongated and resembles an arc welding gouging region, as shown in Figure 2.49.

Figure 2.49: Undercutting in high-speed LBW.



Source: (FABBRO, 2010)

In LBW, humping only begins to be of concern at much higher speeds than for arc welding, in the order of **20 m/min**. It is most often attributed either to the Rayleigh capillary

instability (CAI; WU; GAO, 2017; GRATZKE et al., 1992; WEI, 2010) or to the backward flow induced buildup (AI et al., 2018; FABBRO, 2010), both of which result in BCM humping.

Higher welding speeds can be used in HLAW when compared to arc welding processes (ONO et al., 2002; SUGINO et al., 2005). Sugino *et al.* (2005) found a maximal humping-free welding speed for pulsed arc GMAW of only **0.45 m/min**, while the addition of a **5 kW** laser beam to the process resulted in an increased maximal speed of **7 m/min**. It was noted by Murakami *et al.* (2010) that an arc leading configuration (pulling torch) had a higher tendency for humping formation due to the plasma drag force induced high-speed backward flow.

2.3.4.2 Other Discontinuities

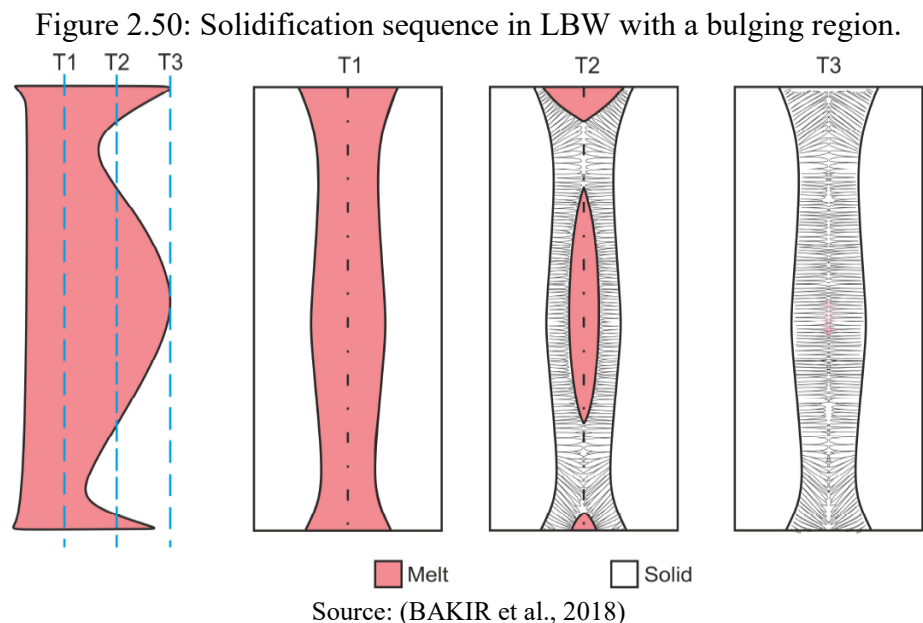
Root humping⁴ is a weld discontinuity observed in LBW and HLAW of thick plates, characterized by the formation of periodic drop-like humps on the weld root, usually accompanied by undercutting and lack of filling on the weld crown (ILAR et al., 2012; LIENERT, 2011; POWELL et al., 2015). In some cases, gravity can lead to the hump detachment from the molten pool.

Many factors can influence the likelihood of root humping, including: laser beam power, welding speed, shielding gas, laser wavelength, material properties, molten pool flow and joint geometry (CAO et al., 2011; FROSTEVARG, 2018; GOOK; GUMENYUK; RETHMEIER, 2014; HAUG et al., 2013; OHNISHI et al., 2013; PAN et al., 2016b; PETRING et al., 2007; SUDER et al., 2017). In general, reducing the root width is benefic to avoid root humping (FROSTEVARG, 2018; SUDER et al., 2017).

Porosity is a common discontinuity in welded parts and may be caused by inadequate shielding, dirt, humidity and other factors. In LBW and HLAW, porosity can also be caused by entrapped gas from vapor capillary instabilities, including collapse and bubble formation on the bottom or on the rear wall (BUNAZIV et al., 2018a; MATSUNAWA et al., 2003; RIBIC; PALMER; DEBROY, 2009; UCHIUMI et al., 2004). HLAW is less sensitive to porosity due to the lower solidification rate, which gives enough time for more entrapped gas bubbles to buoy and leave the molten pool (KATAYAMA et al., 2006; RIBIC; PALMER; DEBROY, 2009; UCHIUMI et al., 2004). Vapor capillary opening stabilization has also been suggested as porosity reduction phenomenon in HLAW (KATAYAMA et al., 2006). For hybrid laser-GMA welding process, the droplet impinging too close to the vapor capillary opening can lead to instabilities and consequent higher porosity (BUNAZIV et al., 2018a).

⁴ Root sagging, root dropout and root drop-through are other nomenclatures that have been used throughout the literature to describe this discontinuity.

Solidification cracking (sometimes referred to solidification flaw) is of great concern in LBW and HLAW due to the typically high aspect ratio of the welds produced by these processes (AKSELSEN; REN; AAS, 2014; BAGGER; OLSEN, 2005; DOWDEN; SCHULZ, 2017). Solidification cracking in LBW and HLAW tend to occur in the weld interior rather than on the crown surface, usually associated with a bulged region of the molten pool. The bulge is a local hot spot that has a later solidification than the surrounding region, so segregation of low melt point constituents (e.g. Sulphur in steels) can cause a thin film of liquid metal between the solidification fronts to extend into the tensile thermal stress region following the welding process (BAKIR et al., 2018; BARBETTA, 2014). Figure 2.50 presents the solidification with such a hot spot where solidification cracks tend to occur. It has been proposed that the pool bulge is caused by a local laser absorption peak (BARBETTA, 2014), but newer studies suggest that convection mechanisms lead to faster cooling of the regions above and below the bulge (ARTINOV et al., 2018; BAKIR et al., 2018), as discussed in Section 2.3.3. Results obtained by Gebhardt *et al.* (2014) suggest that increasing the arc-power-to-laser-power ratio reduces solidification cracking tendency in HLAW.



2.3.5 Hybrid Laser-Buried Arc GMA Welding

Literature on the usage of buried arc in HLAW is scarce and no clear example of a buried spray arc being employed in HLAW was found. Nevertheless, some examples of buried arc HLAW with different transfer modes and other relevant information are cited next.

Wahba *et al.* (2015) used a buried arc hybrid laser-GMAW process with **100 % CO₂** as shielding gas in a leading torch configuration. Sound and fully penetrated weld beads were obtained on **17 mm** thick K36D shipbuilding with square groove joint preparation and **0.5 mm** root gap by employing only **8 kW** laser power and **310 A** average current. It is not clear in the work if the transfer mode was still globular in the buried arc condition, but spatters were suppressed, nevertheless. Good metallurgical properties were also found.

Pan *et al.* (2016b) compared the pulsed arc with Ar+20 % CO₂ shielding gas to buried globular arc in hybrid laser-GMA welding of **11 mm** thick high strength steel HT780. The buried globular arc condition resulted in increased penetration, reduced spatter and a much wider processing window regarding root humping and underfill. The same arc current (**280 A**) and wire feed rate (**11.5 m/min**) were used for both conditions.

Modified pulsed arc with shorter length was supposedly employed by Gook *et al.* (2014) in HLAW, resulting in higher penetration of the arc zone in the molten pool and extending the region where adequate filler metal mixing was obtained, but little difference in dilution was seen within the laser zone. Another benefit noted by the authors is that undercuts and root humping were suppressed. However, it is unclear if the arc could be considered buried in this work, as the arc length above the surface was measured at **3.1 mm**, and the conventional pulsed arc had a very similar length of **3.3 mm**. The observed benefits might be better explained by the higher peak current of **608 A** for the supposedly modified pulsed arc versus **494 A** for the conventional pulsed arc, which should lead to stronger plasma pressures on the pool surface, despite similar average currents (**248 A** and **237 A** respectively) and similar average voltages (**30.6 V** and **30.9 V** respectively). Arc power was also reportedly higher for the modified process, at **9.4 kW**, against the **8.4 kW** observed on the conventional variant.

Gong *et al.* (2017) performed HLAW in a **6 mm** wide and **10 mm** deep groove. Although no buried arc was used in their experiments, the effect of the narrow groove constraining the arc can be considered analogous to the walls of the pool depression in a buried arc. It was found that the constrained arc led to improved droplet detachment and to higher arc pressure on the molten pool surface. The higher arc pressure has been shown to stabilize and widen the vapor capillary opening (FABBRO, 2010).

3 METHODOLOGY

3.1 EQUIPMENT

The welding experiments for this work were carried in a custom-made SL8600 laser processing machine from Preco Inc. This machine is comprised of a 5-axis moving system, a Trumpf 10002 TruDisk laser and a Digiplus A7 PMDAC – 1000 welding source from IMC. Figure 3.1 shows a general view of the machine.

Figure 3.1: Laser processing machine SL8600 from Preco Inc.



The moving system has a XY-table with **10 m/min** maximum feed rate. The laser welding head moves in the Z-axis. The last two axis are given by a rotary tilting table attached to the XY-table, but it was not used for the present work.

The high-power disk laser is attached to a Laser Mech welding head with reflective optics through an optical fiber. The laser and the optical system main characteristics are presented on Table 3.1.

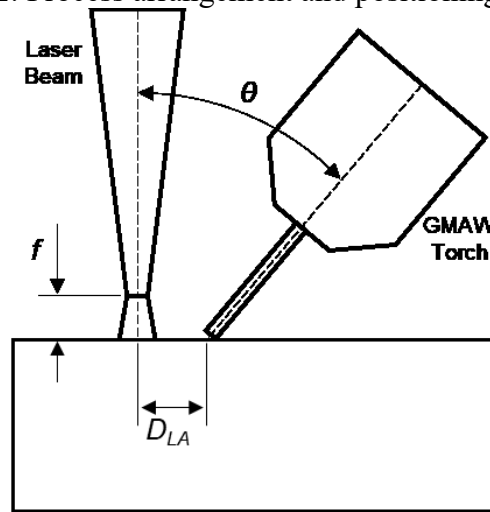
The multi-process dual output Digiplus A7 welding source is capable of GMAW, GTAW, SAW, PAW and other processes with a maximum peak current of over **1000 A** and maximum filler metal feed rate of **20 m/min**. It is a transistorized welding source which acts as a current source and can operate as a constant current or a constant voltage source for GMAW. The welding source also has an inbuilt current and voltage acquisition system (**5 kHz** acquisition rate) that was used to measure these variables. Those acquisitions were taken for the whole length of the weld, except for the unstable regions at the beginning and at the end of the process.

Table 3.1: Laser and optical system characteristics.

Characteristic	Value
Max. Beam Power	10 kW
BPP	8 mm.mrad
Fiber Core Diameter	200 μm
Collimating Focal Length	150 mm
Focusing Focal Length	450 mm
Focal Spot Diameter	600 μm

Figure 3.2 shows the welding process arrangement with the definition of laser-arc distance (D_{LA}), focal position (f) and torch angle (θ). The plates to be welded were placed on top of the XY-table and the GMAW torch attached to the laser welding head. The GMAW torch fixture allows dislocation in X, Y and Z axis and rotation in the X axis in relation to the laser welding head, thus torch inclination, D_{LA} and f could be varied.

Figure 3.2: Process arrangement and positioning variables.



High-speed imaging was carried using a Phantom V611 camera from Vision Research. The camera monitored the process from the side, placed **1800 mm** away and **210 mm** above from the process, inclined 7° from the workpiece plane. The used recording parameters are shown in Table 3.2.

Table 3.2: High-speed imaging parameters.

Characteristic	Value
Resolution	320 x 240 pixels
Acquisition Rate	20000 fps
Exposure	5 μ s
Lens Focal Length	135 mm
Lens Aperture	f/16.0

3.2 MATERIALS

3.2.1 Base Metal

Two different base metals have been used in this work. SAE 1020 steel has been chosen as the base metal for the development of the buried spray arc HLAW process. Its simpler composition has less influence on the results, facilitating the analysis of the process itself. SAE 1020 steel plates with dimensions **400x300x12.5 mm³** were used for bead on plate welding. The standardized metal composition is presented in Table 3.3.

Table 3.3: SAE 1020 steel composition.

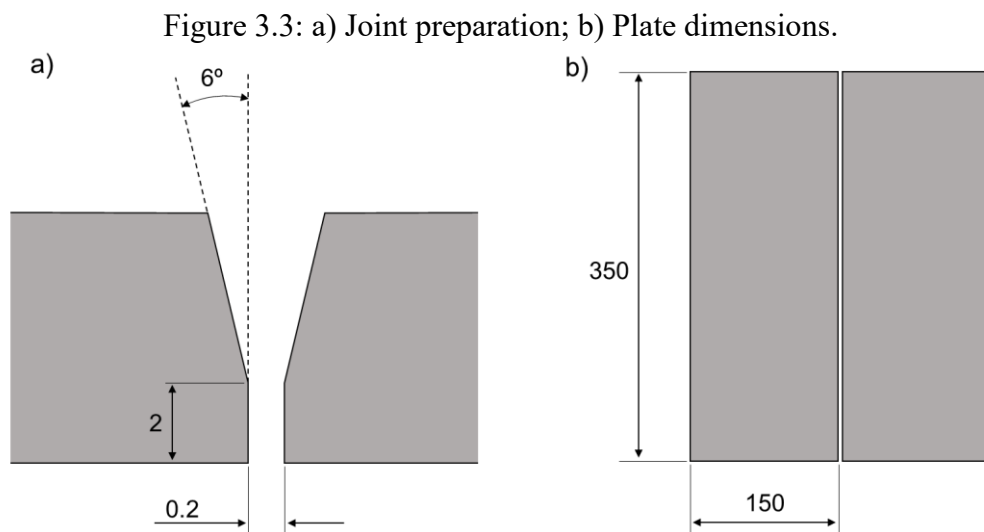
C	Mn	P	S	Fe
0.17-0.23	0.30-0.60	≤ 0.040	≤ 0.050	Balance

As an example of the buried spray arc HLAW application of industrial interest, **9.5 mm** thick thermo-mechanically control processed (TMCP) ASTM A709 HPS 70W steel was chosen, which is an atmospheric corrosion resistant high-strength low alloy structural steel. The material was provided by Usiminas and its main applications are road structures. Table 3.4 presents the measured chemical composition of this steel as measured through spark optical emission spectroscopy.

Table 3.4: ASTM A709 HPS 70W composition.

C	Si	Mn	P	S	Cr
0.05	0.41	1.13	0.02	0.003	0.51
Mo	Ni	Al	Cu	V	Fe
0.03	0.35	0.04	0.33	0.04	Balance

As an application example, the welding process was carried on joints rather than beads on plate. The joint configuration followed the best results from Cao *et al.* (2011), who performed HLAW under similar conditions (plate thickness, laser power, welding speed and material), except for the high-current buried arc. Y-joints were milled with 6° bevel angle to each side (12° total opening), **2 mm** root face and **0.2 mm** root opening (gap), as depicted in Figure 3.3 (a). The plates dimensions were **150 mm** wide and **350 mm** long to accommodate a **300 mm** weld length, following ISO 15614-11 (2002) recommendations (Figure 3.3 (b)). Drawings in Figure 3.3 are out of scale for clarity.



All plates were machined in order to remove scales and oxides on surfaces near the welding process and then cleaned with ethylic alcohol.

3.2.2 Filler Metal

1.2 mm diameter AWS A5.18 ER 70S-6 was chosen as filler metal for the same reason as the SAE 1020 base steel: simple composition with reduced interference on the welding process. It is also usually recommended for SAE 1020 steel welding.

The same filler metal was used for ASTM A709 HPS 70W welding, as the same parameters obtained for SAE 1020 welding could be used and due to the lack of recommendation for HLAW processing of this steel. The Steel Market Development Institute (2011) recommends using AWS A5.28 E90C-G metal cored filler metal for GMAW processing of ASTM A709 HPS 70W steel. However, the HLAW process exhibits higher cooling rates and increased base metal dilution in the weld metal than the multi-pass GMAW, so the GMAW recommended

filler metal might not be adequate for HLAW. The reduced alloy content and equivalent carbon of the ER 70S-6 wire might even be better for HLAW than the E90C-G, giving these conditions.

3.2.3 Shielding Gas

1 μm wavelength lasers do not require plasma suppression capable shielding gases, therefore the shielding gas can be chosen solely based on the GMAW and metal requirements (BAGGER; OLSEN, 2005; ERIKSSON; POWELL; KAPLAN, 2013). Spray arc transfer usually require argon based shielding gases, often mixed with CO₂. Most authors have been found to work with CO₂ contents of **8 %** (GONDIM et al., 2016; MVOLA BELINGA, 2012; WEMAN; LINDEN, 2006), **10 %** (BUDIG, 2005; DOMPABLO, 2013) and **18 %** (HEINZE et al., 2014; SCHAUPP; RHODE; KANNENGIESSER, 2018; ZHANG et al., 2015) for buried spray arc GMAW. Since increased CO₂ content reduce the tapering length (liquid metal projection) and suppresses the kink instability (RHEE; KANNATEY-ASIBU JR., 1992) *apud* (SCOTTI, 2000) and since most recent works apply Ar+18 %CO₂ as the shielding gas, that same mixture was chosen.

The gas flow was defined as **20 l/min**, which has been shown to be adequate in other works (HEINZE et al., 2014; MVOLA BELINGA, 2012; WEMAN; LINDEN, 2006).

3.3 METHODS

For the development of this thesis, four sets of experiments were carried, where the previous set would feed necessary information for the following set:

- Buried spray arc GMAW parameters development and process evaluation;
- Application of the buried spray arc in the HLAW process;
- Comparison between buried arc and conventional arc for HLAW; and
- Application example of the developed buried spray arc HLAW for joining A709 HPS 70W steel plates.

The experimental procedure for each of these steps will be presented in the following sections.

3.3.1 Buried Spray Arc GMAW Preparation

This set of experiments is meant to address the first specific objective of this work, that is, to prepare the high-current buried spray arc GMAW for hybridization with the laser beam and evaluate its stability under such conditions (welding speed, torch inclination and current).

Most authors have studied the buried spray arc at lower welding speeds, between **0.35 m/min** and **0.6 m/min** (BABA et al., 2017; CHEN et al., 2011; GONDIM et al., 2016; HEINZE et al., 2014; SPROESSER et al., 2015). Among the few exceptions are Yuan *et al.* (2016), who applied welding speeds from **0.8 m/min** to **1.4 m/min**, and Stol *et al.* (2006), working in the **0.7 m/min** to **1.8 m/min** range. In the present work, the buried spray arc GMAW process was studied at **1.0 m/min**, **1.5 m/min** and **2.0 m/min** welding speeds, representing more typical values for thick plate processing with HLAW.

The buried spray arc GMAW process is mostly carried with the torch perpendicular to the welding direction (**0°**) (GONDIM et al., 2016; HEINZE et al., 2014; SCHROEPFER; KROMM; KANNENGIESSER, 2017; STOL; WILLIAMS; GAYDOS, 2006). In HLAW, a perpendicular torch would only be possible in a coaxial configuration, which is not available in the present system and would carry its own disadvantages, as discussed previously. Therefore, this work also studied the implications of using the torch at both the pulling and the pushing positions. A torch inclination of **40°** (to the orthogonal) was chosen, which is a bit more inclined than usual for HLAW (ERIKSSON; POWELL; KAPLAN, 2013), with the intent of exacerbating its influence on the process and to allow very short D_{LA} to be used in the following experiments.

The welding source was operated as a constant voltage source, since the self-regulating arc length property of this mode is expected to keep the process more robust at the low arc lengths employed in the buried arc condition. The welds were carried as bead on plate in the plane position on SAE 1020 steel.

In order to compare the pushing and the pulling configurations, the following factors were fixed for both conditions: current, contact-tip-to-work distance (*CTWD*), wire feed rate, source inductance, shielding gas composition and shielding gas flow. The voltage was varied in order to obtain the buried spray arc at the same welding current for both configurations. Pushing and pulling welding with increased (conventional) arc length and same current were also performed in order to observe which effects are due to the increased arc current and which are due to the buried arc. In order to achieve the same welding current with longer arcs, the wire feed rate was changed as well.

The target current was defined as the highest possible current considering the equipment wire feed rate limitation of **20 m/min** and the influence of *CTWD*. The shorter the *CTWD*, the higher the average current can be for the same arc length, which must be near **0** for a buried arc. However, the laser beam will intersect the torch components if a too short *CTWD* is used in HLAW. Considering these limitations, a good compromise was found by using an average

current in the range between **460 A** and **480 A** and a *CTWD* of **15 mm**. The chosen welding current is expected to provide adequate buried spray arc GMAW as both lower (BUDIG, 2005; CHEN et al., 2011; GONDIM et al., 2016) and higher (BABA et al., 2017) currents have already been used for **1.2 mm** wires. **15 mm** *CTWD* in buried spray arc has been used before by Gondim *et al.* (2016), is only **2 mm** longer than the one from Heinze *et al.* (2014) and within the typical *CTWD* for spray arc HLAW (**15 mm** to **25 mm**) according to Eriksson *et al.* (2013).

The welding source used in this work has also configurable source inductance, represented by the factors K_S and K_D , which inversely correlate to the current rise inductance and to the current drop inductance respectively. K_S was defined as **100** and K_D as **1**, meaning very low rise inductance and very high drop inductance, based on previous unpublished works.

Once the parameters combinations which resulted in all desired welding conditions (buried and long arc at pushing and pulling torch positions at the same average current), **3** additional reproductions of the welds were performed. These experiments were evaluated by the current and voltage acquisition system included in the welding source and by high-speed imaging.

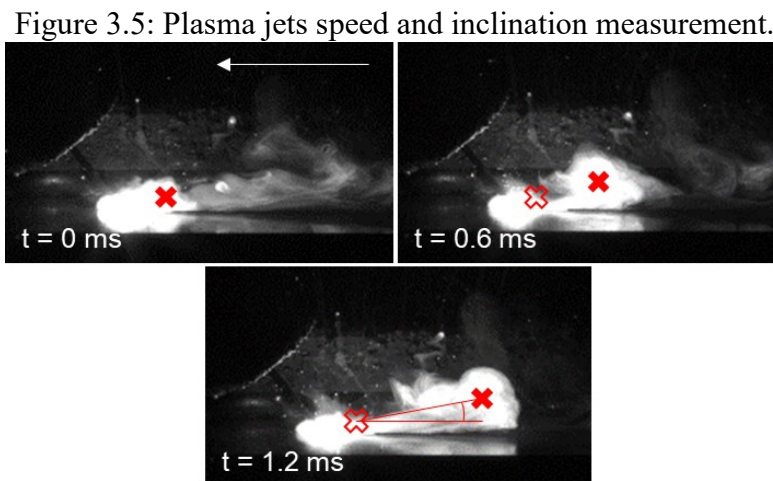
From the high-speed imaging, it was possible to measure the arc length and the arc plasma jets speed and direction. The arc length was measured by taking three random frames from the videos and taking the distance between the original workpiece surface (the arc length beneath the surface is not considered) and the lowest point where the wire is still visible, as in the example from Figure 3.4. The ImageJ software (RASBAND, [s.d.]) was used for these measurements and the values were corrected for the camera vertical tilt.

Figure 3.4: Arc length measurement



Turbulence and other visible features on the forward and backward plasma jets (the plasma jet within the arc was not measured) were used to track the jets speed and direction,

such as in the example from Figure 3.5. This kind of measurement is subject to subjective interpretation of the operator and has poor repeatability. It is still useful for qualitative comparison though. Three measurements were taken for each welding condition and all measurements were taken on the same day by the same operator to improve reliability. The speed and angle measurement function of the high-speed camera proprietary software PCC was used to analyze the videos.



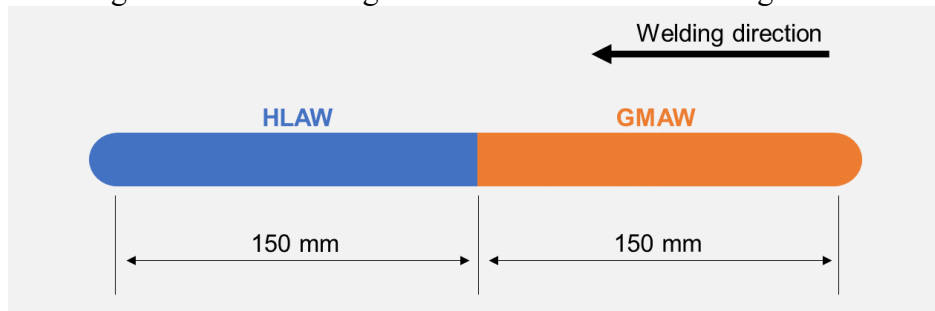
3.3.2 Application of the Buried Spray Arc in HLAW

A laser beam was added to the buried spray arcs (and high-current long arcs) developed in the previous set of experiments to evaluate if the process remains stable and if adjustments are needed to the arc parameters.

The laser power was fixed at **10 kW** to impose the maximum interaction permitted by the present system, and D_{LA} and f were defined as **2.5 mm** and **-3 mm** respectively, close to the expected optimal position for conventional HLAW (BUNAZIV et al., 2015; ERIKSSON; POWELL; KAPLAN, 2013). The three welding speeds (**1.0 m/min**, **1.5 m/min** and **2.0 m/min**) from before were tested again for HLAW.

The bead on plate welds were **300 mm** long and an alternation between GMAW and HLAW in the same bead was used to reduce the effect of other random factors and errors, which could influence the process. The first half of the bead was carried with GMAW only and the laser beam was turned on in the middle of the bead, at the **150 mm** length mark, as depicted in Figure 3.6. That way, it is possible to have a better and safer analysis of the laser beam effect on the arc and on the process, especially on the electric properties of the welding arc (current and voltage).

Figure 3.6: Alternating GMAW and HLAW on a single bead.



As in the previous case, current and voltage acquisition and high-speed imaging were used to monitor the process. Each experiment was carried only once.

3.3.3 Comparison between Buried and Conventional Arc HLAW

This set of experiments were carried with the intent of clarifying if the usage of buried spray arc in HLAW could provide improved penetration, which would allow using less powerful lasers or increase welding speed. The pushing and pulling buried arc HLAW were compared among themselves and against the high-current long arc HLAW and also against a more conventional (lower current) spray HLAW condition. Pulling torch position was used for high-current long arc, as it should give deeper penetration and is better comparable to conventional spray arc HLAW. Therefore, the pushing position was disregarded for the high-current long arc HLAW in this set of experiments.

Each process should be used in its optimal penetration condition (D_{LA} and f) for adequate comparison. It has been shown in the literature that the optimum penetration occurs mostly between **2** and **3 mm** D_{LA} and with the laser beam focus slightly below the surface (BUNAZIV et al., 2015). For this reason, the conventional spray arc HLAW was welded with D_{LA} and f as **2.5 mm** and **-3 mm** respectively, which should be at the optimum condition or very close to it. The arc parameters are the same as for the pulling buried arc, except for voltage (**30 V**) and wire feed rate (**7.5 m/min**) resulting in a more typical current of **250 A** and arc length of around **5 mm**. This condition was reproduced four times.

Little study has been carried with the high-current processes (buried and long arc), so it is not possible to obtain a good estimate for optimal heat sources positioning from the literature. Therefore, experimentation is necessary to find this position.

D_{LA} and f were optimized for the penetration depth (PD) for the pushing buried arc, for the pulling buried arc and for one of the long arc, whichever showed the most promising results. The Response Surface Method (RSM) with the second order Central Composite Design (CCD), as described by Montgomery (2013), was chosen as the evaluation and optimization

method. Although the exact optimum position is unknown, there is a very limited region where it might be found, so using the second order model directly is justifiable.

The CCD method was applied for each of the three welding conditions separately. Other factors will be held constant according to the previous experiments sets, including laser power, welding feed rate, torch angle, etc.

As shown in Table 3.5, the central point for the factors D_{LA} and f were chosen to be **2.5 mm** and **-3 mm**, the same as the conventional HLAW estimated optimum. The axial points for the D_{LA} were defined as **-1 mm** and **6 mm**, and as **-8 mm** and **2 mm** for the f , which represent the minimum and the maximum values at which each factor will be tested. The factorial points then followed. The same points were used for all three welding conditions.

Table 3.5: CCD points for D_{LA} and f .

CCD Point	D_{LA}	f
-1.414	-1.0	-8.0
-1	0.0	-6.5
0	2.5	-3.0
1	5.0	0.5
1.414	6.0	2.0

The order of each point execution was fully random and is presented in Table 3.6. To save time, after each aligning of the welding torch all three welding conditions were executed for that combination of D_{LA} and f values, also in a random manner.

Due to time and resource constraints, only one weld was performed for each point (no replication, except for the central points). The weld length was **300 mm**. Two measurements of the PD were taken for each weld, one **100 mm** from the weld beginning and the other **100 mm** from the weld end by transverse sectioning, grinding and etching. The macrographs were then measured with the help of the ImageJ software (RASBAND, [s.d.]).

Table 3.6: CCD experiments order.

D_{LA}	f	Order
0.0	-6.5	6
5.0	-6.5	3
0.0	0.5	4
5.0	0.5	1
2.5	-3.0	5
2.5	-3.0	2
6.0	-3.0	5
-1.0	-3.0	2
2.5	2.0	1
2.5	-8.0	4
2.5	-3.0	3
2.5	-3.0	6

3.3.4 HPS 70W Steel Application Example

Bead on plate welds are useful to obtain good amount of information about the process while consuming less time and resources. However, in industrial applications, the buried spray arc HLAW will be applied for joining procedures, thus on joints. This set of experiments emulated one possible application of the developed process on the atmospheric corrosion resistant ASTM A709 HPS 70W structural steel with a thickness of **9.5 mm** and Y-joint preparation. It was compared to the conventional spray arc HLAW used in the previous set of experiments as well. Only the **1.5 m/min** welding speed was used for these tests.

To determine the required laser power for full penetration, bead on plate welds were carried on the similar plates as the ones to be joined. The laser power was varied along the **400 mm** weld length with a **5 kW** variation range (**3 kW** to **8 kW** for buried spray arc HLAW, **5 kW** to **10 kW** for conventional HLAW). This way, the required laser power for full penetration was inferred from the distance needed for the molten pool to emerge and be maintained on the bottom side of the plate. This procedure was repeated twice for each process.

The author is aware that this procedure tends to overestimate the required laser power needed, as the chosen joint configuration has gap opening (root opening and bevel), which facilitates penetration. However, some excess power is often needed for good welds and the excess will be similar for both the buried spray arc HLAW and the conventional HLAW, allowing comparisons between both.

One **300 mm** weld for each process was then carried on the Y-joints using the laser power required for full penetration. Two cross sections were taken at **100 mm** after the weld beginning and at **100 mm** before the weld termination, which were then analyzed regarding the bead geometry. Metallurgical, mechanical and corrosion resistance properties of the welds are out of the scope of the present work and will be evaluated in future publications. Root backing was used to avoid root humping in welds performed in a joint.

4 RESULTS

4.1 BURIED SPRAY ARC GMAW PREPARATION

Parameters resulting in stable welding were found for all four GMAW conditions are displayed in Table 4.1. U is welding voltage and V_w wire feed rate. In order to achieve the same average current and process stability, the pushing position required higher voltage (**2 V**) for both the buried and the long arc.

Table 4.1: Defined GMAW parameters.

Torch	Arc	U (V)	V_w (m/min)	CTWD (mm)	θ
Pulling	Buried	35	18	15	40°
	Long	40	14	15	40°
Pushing	Buried	37	18	15	-40°
	Long	42	14	15	-40°

The found parameters were applied for bead on plate welding at **1.0 m/min**, **1.5 m/min** and **2.0 m/min** welding speed (V) and the arc length (L), the average current (I_m) and the bead appearance are summarized in Table 4.2. **1.3 mm** was the shortest arc length obtained for both pulling and pushing buried arcs where the process remained stable at **1.0 m/min**. **4.5 mm** and **4.3 mm** were the arc lengths for the pulling and pushing (high-current) long arcs respectively at the same welding speed. The arc length tended to have a small increase as faster welding speeds were applied. However, the average current remained between **460 A** and **480 A** under every condition.

Due to the high welding speeds and high currents for GMAW process, humping and undercutting have been observed in most welds, especially at welding speeds over **1.5 m/min**. The pushing buried arc showed the best results in that regard, as the humping was not so severe even at **2 m/min**, while the pulling long arc seemed to be the most unstable under the present conditions. Severe spattering was seen in the pushing long arc welds at every welding speed. Images of the beads are shown together with those from HLAW in the next section (4.2).

Arc measurements with the high-speed imaging system is shown in Table 4.3, with the arc length (L), the forward plasma jet speed (v_F) and inclination to the workpiece surface (α_F) and the backward plasma jet speed (v_B) and inclination (α_B). As mentioned before, the plasma jets measurements are meant for comparison's sake only.

Table 4.2: Summarized GMAW results.

Torch	Arc	V (m/min)	I_m (A)	Bead
Pulling	Buried	1.0	460	Good (narrow)
		1.5	466	BCM Humping and Undercut
		2.0	470	BCM Humping and Undercut
	Long	1.0	464	Undercut and Irregular
		1.5	469	GRM Humping
		2.0	471	GRM Humping
Pushing	Buried	1.0	467	Good (wide)
		1.5	472	Light Humping
		2.0	469	Undercut and GRM Humping
	Long	1.0	469	Spatter and GRM Humping
		1.5	474	Spatter and GRM Humping
		2.0	468	Spatter and GRM Humping

Table 4.3: High-speed imaging measured arc characteristics.

Torch	Arc	V (m/min)	L (mm)	v_F (m/s)	α_F	v_B (m/s)	α_B
Pulling	Buried	1.0	1.3	-	-	24	42°
		1.5	1.5	-	-	25	8°
		2.0	1.7	-	-	26	18°
	Long	1.0	4.5	-	-	25	15°
		1.5	5.1	-	-	25	8°
		2.0	5.0	-	-	23	7°
Pushing	Buried	1.0	1.3	9	3°	-	-
		1.5	2.1	7	50°	10	12°
		2.0	2.1	9	30°	23	24°
	Long	1.0	4.3	13	7°	10	10°
		1.5	5.2	17	8°	6	9°
		2.0	5.7	11	2°	-	-

4.2 APPLICATION OF THE BURIED SPRAY ARC IN HLAW

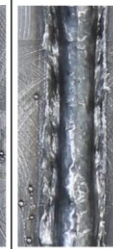
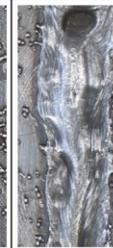
The parameters developed in the last set of experiments were applied for GMAW and HLAW in a single bead for all four welding conditions and at three different welding speed levels. The resulting average currents, voltages and arc lengths are presented in Table 4.4.

Table 4.4: Average current, voltage and arc length for GMAW and HLAW

Torch	Arc	V (m/min)	GMAW			HLAW		
			I_m (A)	U_m (V)	L (mm)	I_m (A)	U_m (V)	L (mm)
Pull	Buried	1.0	457	35.9	0.8	462	36.0	0.9
		1.5	474	35.8	1.6	465	35.8	1.8
		2.0	464	35.8	1.9	461	35.8	2.2
	Long	1.0	469	40.8	4.3	476	40.8	4.6
		1.5	459	40.8	5.0	459	40.8	5.2
		2.0	461	40.8	5.5	459	40.8	5.7
Push	Buried	1.0	459	38.2	1.5	463	39.3	2.0
		1.5	461	39.6	3.0	461	39.9	3.1
		2.0	463	38.4	2.4	462	37.3	2.6
	Long	1.0	463	43.0	4.6	460	43.6	5.0
		1.5	473	43.0	5.1	480	44.7	5.0
		2.0	457	43.0	6.1	462	44.1	5.7

Figure 4.1 shows how the bead appearance changed as the **10 kW** laser beam was applied during the welding. In many cases, humping was reduced or eliminated when the process changed to HLAW. Pulling torch still resulted in more humping than welding with a pushing torch. Severe spatter was still present in every pushing long arc welding.

Figure 4.1: Bead appearance for GMAW and HLAW.

Welding direction ↑	1.0 m/min		1.5 m/min		2.0 m/min	
	GMAW	HLAW	GMAW	HLAW	GMAW	HLAW
Pulling Buried Spray Arc						
Pulling High-Current Long Spray Arc						
Pushing Buried Spray Arc						
Pushing High-Current Long Spray Arc						

4.3 COMPARISON BETWEEN BURIED AND CONVENTIONAL ARC HLAW

The results for the conventional HLAW, the pulling buried arc HLAW, the pulling high-current long arc HLAW and the pushing buried arc conditions are presented in the following sections.

4.3.1 Conventional HLAW

Conventional spray arc HLAW was only performed with a **2.5 mm** laser-arc distance and **-3 mm** focal position, with four runs. The penetration depth of each is presented in Table 4.5. The beads showed overall good appearance.

Table 4.5: Conventional spray arc HLAW penetration depth.

Run	D_{LA} (mm)	f (mm)	PD (mm)
A	2.5	-3	8.7
B	2.5	-3	9.5
C	2.5	-3	8.0
D	2.5	-3	8.3

4.3.2 Pulling Buried Arc HLAW

Table 4.6 presents the penetration depth (PD) obtained at each pulling buried (spray) arc HLAW run for the second order CCD. The parameters (or factors) are presented in their natural form and in the coded form, which is used for the statistical tests. Equations (4.1) and (4.2) are used to convert the factors from their natural form to the coded form.

Table 4.6: Natural and coded factors and response for the pulling buried arc HLAW.

Run	Natural factors		Coded factors		Response
	D_{LA} (mm)	f (mm)	X1	X2	PD (mm)
4	5	0.5	1	1	10.5
8	2.5	-3	0	0	12.7
10	5	-6.5	1	-1	10.1
14	0	0.5	-1	1	12.5
18	2.5	-3	0	0	12.1
20	0	-6.5	-1	-1	11.4
24	2.5	2	0	1.414	12.3
28	-1	-3	-1.414	0	8.5
32	2.5	-3	0	0	12.3
36	2.5	-8	0	-1.414	11.3
37	6	-3	1.414	0	10.0
41	2.5	-3	0	0	12.4

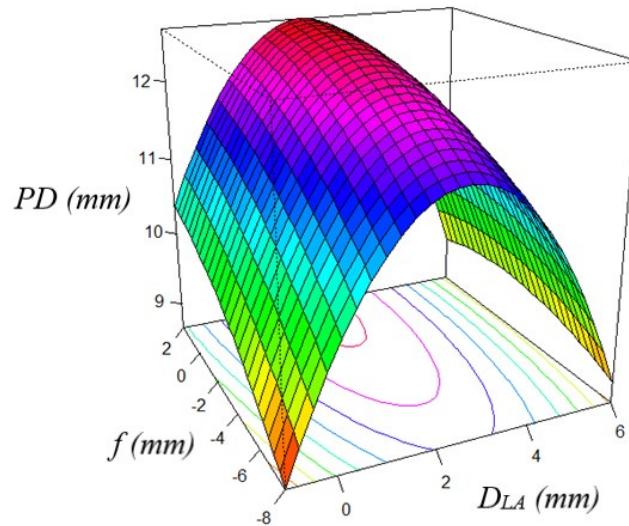
$$X_1 = \frac{D_{LA} - 2.5}{2.5} \quad (4.1)$$

$$X_2 = \frac{f + 3.0}{3.5} \quad (4.2)$$

The fitted response surface follows Equation (4.3) and is plotted in in Figure 4.2. The surface maximum was found as **12.65 mm** at $D_{LA}=2.14$ mm and $f=2.15$ mm. The adjusted determination coefficient is a bit low at **0.55**, and the model cannot be considered statistically significant with a p-value of **0.072**, slightly above the typical **5 %** significance limit. Lack of fit of the quadratic surface was also found significant, at p-value of **0.0363**.

$$PD = 12.3750 - 0.1515X_1 + 0.3623X_2 - 1.4315X_1^2 - 0.1315X_2^2 - 0.1750X_1X_2 \quad (4.3)$$

Figure 4.2: Response surface for the pulling buried arc HLAW.



Analyzing each function term, it is found that only the quadratic effect of the D_{LA} is significant (p-value is **0.0067**), but its linear effect, linear and quadratic f and the interaction term are not significant. It can be seen in the response surface from Figure 4.2 that PD is much more influenced by D_{LA} than by f .

The measured current, voltage and arc length for each run is presented in Table 4.7.

Table 4.7: Average current, voltage and arc length for each pulling buried arc HLAW run.

Run	D_{LA} (mm)	f (mm)	I_m (A)	U_m (V)	L (mm)
4	5	0.5	459	35.9	1.7
8	2.5	-3	462	35.8	1.7
10	5	-6.5	456	35.8	1.7
14	0	0.5	483	35.8	2.0
18	2.5	-3	466	35.8	1.8
20	0	-6.5	445	35.8	2.0
24	2.5	2	477	35.8	1.9
28	-1	-3	434	35.9	3.0
32	2.5	-3	453	35.9	2.2
36	2.5	-8	470	35.8	1.8
37	6	-3	452	35.8	1.7
41	2.5	-3	481	35.8	1.6

4.3.3 Pulling Long Arc HLAW

Similar to the previous section, PD and the other factors for each run of the pulling (high-current) long arc HLAW is shown in Table 4.8.

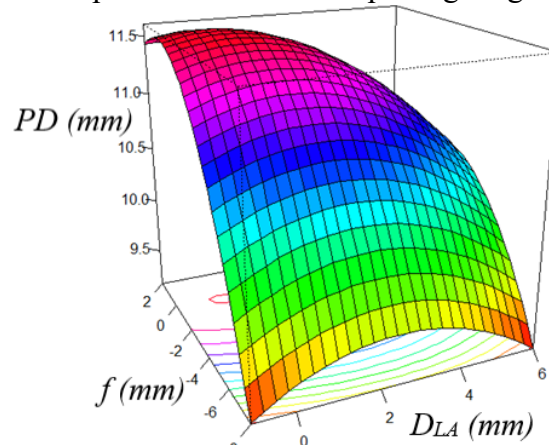
Equation (4.4) represent the response behavior obtained with the best fitting from experimental results. It is also plotted in Figure 4.3. The surface maximum was found at **0.262 mm** and **-0.214 mm** D_{LA} and f respectively, with a PD of **11.60 mm**.

$$\begin{aligned}
 PD = & 11.2749 - 0.2525X_1 + 0.5461X_2 - 0.2189X_1^2 \\
 & - 0.4411X_2^2 - 0.1750X_1X_2
 \end{aligned}
 \tag{4.4}$$

Table 4.8: Natural and coded factors and response for the pulling long arc HLAW.

Run	Natural factors		Coded factors		Response
	D_{LA} (mm)	f (mm)	X1	X2	PD (mm)
4	5	0.5	1	1	10.7
8	2.5	-3	0	0	10.3
10	5	-6.5	1	-1	9.2
14	0	0.5	-1	1	11.0
18	2.5	-3	0	0	11.1
20	0	-6.5	-1	-1	8.8
24	2.5	2	0	1.414	11.3
28	-1	-3	-1.414	0	12.3
32	2.5	-3	0	0	11.2
36	2.5	-8	0	-1.414	10.8
37	6	-3	1.414	0	10.8
41	2.5	-3	0	0	12.5

Figure 4.3: Response surface for the pulling long arc HLAW.



The obtained response surface is statistically not significant by any means, with an adjusted R^2 of **-0.18**, a p-value of **0.667** and no term of the equation achieving significance individually.

The measured current, voltage and arc length for each run is presented in Table 4.9

Table 4.9: Average current, voltage and arc length for each pulling long arc HLAW run.

Run	D_{LA} (mm)	f (mm)	I_m (A)	U_m (V)	L (mm)
4	5	0.5	463	40.9	4.9
8	2.5	-3	463	40.9	4.9
10	5	-6.5	481	40.9	5.4
14	0	0.5	463	40.9	4.5
18	2.5	-3	468	40.9	4.9
20	0	-6.5	470	40.9	5.5
24	2.5	2	487	41.0	5.2
28	-1	-3	485	41.1	5.6
32	2.5	-3	475	40.9	5.4
36	2.5	-8	462	40.8	5.3
37	6	-3	476	41.0	4.9
41	2.5	-3	489	41.0	4.7

4.3.4 Pushing Buried Arc HLAW

Lastly, the pushing buried (spray) arc was tested and the penetration depth is presented in Table 4.10.

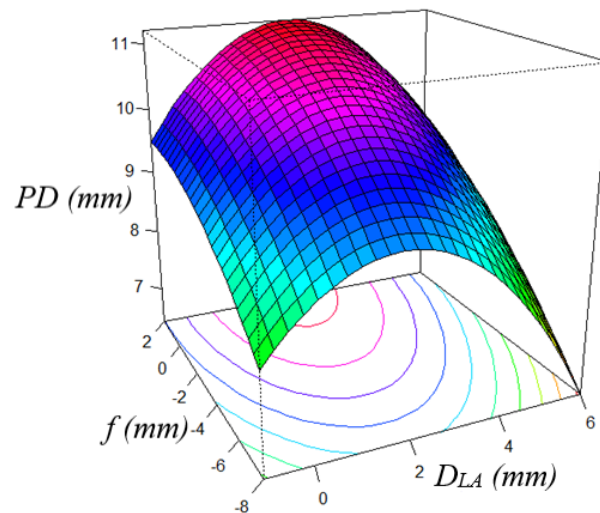
Fitted equation and its plotting are found in Equation (4.5) and Figure 4.4 respectively. At $D_{LA}=2.42$ mm and $f=3.28$ mm the maximum of **11.23 mm** is found.

$$\begin{aligned}
 PD = & 10.5500 - 0.3283X_1 + 0.7529X_2 - 0.9616X_1^2 \\
 & - 0.2083X_2^2 + 0.1500X_1X_2
 \end{aligned}
 \tag{4.5}$$

Table 4.10: Natural and coded factors and response for the pushing buried arc HLAW.

Run	Natural factors		Coded factors		Response
	D_{LA} (mm)	f (mm)	X1	X2	PD (mm)
4	5	0.5	1	1	9.0
8	2.5	-3	0	0	9.3
10	5	-6.5	1	-1	7.3
14	0	0.5	-1	1	10.7
18	2.5	-3	0	0	11.5
20	0	-6.5	-1	-1	9.6
24	2.5	2	0	1.414	11.5
28	-1	-3	-1.414	0	8.4
32	2.5	-3	0	0	8.8
36	2.5	-8	0	-1.414	9.2
37	6	-3	1.414	0	9.4
41	2.5	-3	0	0	12.6

Figure 4.4: Response surface for the pushing buried arc HLAW.



Once again, no significance was found for the model, with an adjusted R^2 of **-0.01**, a p-value of **0.499** and no term of the equation achieving significance individually.

The measured current, voltage and arc length for each run is presented in Table 4.11.

Table 4.11: Average current, voltage and arc length for each pushing buried arc HLAW run.

Run	D_{LA} (mm)	f (mm)	I_m (A)	U_m (V)	L (mm)
4	5	0.5	452	39.0	2.4
8	2.5	-3	465	40.2	2.4
10	5	-6.5	460	39.8	2.9
14	0	0.5	476	39.4	4.2
18	2.5	-3	474	39.6	3.0
20	0	-6.5	485	39.6	3.9
24	2.5	2	469	39.7	3.1
28	-1	-3	478	39.8	4.2
32	2.5	-3	460	39.0	3.0
36	2.5	-8	477	40.1	3.8
37	6	-3	450	38.9	1.4
41	2.5	-3	478	39.6	3.1

4.4 HPS 70W STEEL APPLICATION EXAMPLE

The required laser power needed for fully penetrating the **9.5 mm** HPS 70W steel plates at **1.5 m/min** welding speed was found to be 7.7 kW for the conventional spray arc HLAW (**250 A**) and **4.8 kW** for the pulling buried spray arc HLAW (**460 A**), a reduction of **38 %**.

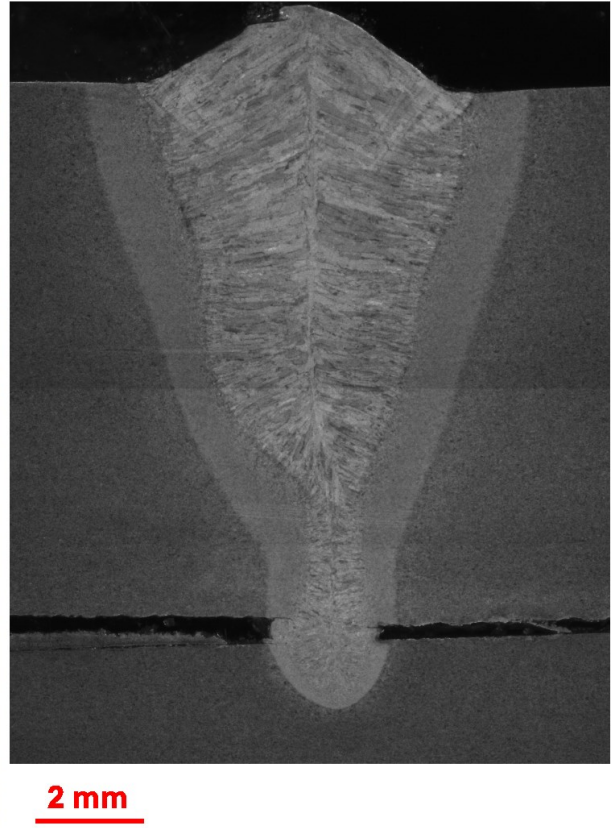
When the Y-joints were welded, the buried spray arc HLAW process resulted in a weld with good crown appearance: without humping and undercutting and with adequate reinforcement. The weld with conventional HLAW resulted in undercutting on the other hand. Beads cross section images are shown in Figure 4.5. Solidification cracking was found on the conventional spray HLAW but not on the pulling buried spray HLAW.

Figure 4.5: Conventional spray HLAW and pulling buried spray HLAW macrographs.

Conventional Spray HLAW



Pulling Buried Spray HLAW



5 DISCUSSION

5.1 BURIED SPRAY ARC GMAW

5.1.1 Buried Spray Arc Condition

Two conditions were defined for GMAW process to be considered in a buried spray condition. The first one is that most of the arc length is found beneath the original workpiece surface, that is, buried. The second one is that the metal transfer mode is predominantly spray.

5.1.1.1 Arc Length

To achieve the first condition, the arc length above the surface must be shorter than the pool depression. Although direct visualization of the pool depression was not possible with the present experimental configuration, craters left when the arc suddenly extinguishes can give a good insight into the pool shape if conditions are right. This technique has been used before by Mendez and Eagar (2003).

The trailing region could partly or fully refill the gouging region before the solidification was completed for both pulling and pushing buried arcs, so the technique could not be directly applied to those conditions. For the pulling long arc, on the other hand, solidification was finished before significant refilling could take place, allowing the crater to retain its during-welding characteristics and the pool depression properly measured. Table 5.1 compares the arc lengths for pulling and pushing buried arcs as measured through high-speed imaging to the crater depth obtained with the pulling long arc. Since the pool depression for the buried conditions is expected to be deeper than that of the long arc, it can be assumed that the majority of the arc length is beneath the original workpiece surface, thus the arc can be considered buried.

Table 5.1: Pool depression and arc length at different welding speeds.

	1.0 m/min	1.5 m/min	2.0 m/min
Pulling Long Arc Crater (mm)	4.0	3.5	3.5
Pulling Buried Arc Length (mm)	1.3	1.5	1.7
Pushing Buried Arc Length (mm)	1.3	2.1	2.1

The increased arc length above the workpiece surface at higher welding speeds can be related to the reduced pool depression. Considering that the total arc length should remain roughly constant, as the depression gets shallower, less of the arc is buried and more of it should

be visible above the original surface. Interestingly, the shallower pool depression would result in a shorter effective *CTWD* and the current would then be expected to increase. The fact that no significant current variation was observed could be due to changes in the arc geometry and attaching to the electrodes, which could change its impedance, or due to a too small influence compared to the process random variation.

5.1.1.2 Metal Transfer

Current and voltage oscillograms for the pulling buried arc and for the pushing buried arc for the three welding speed levels are presented in Figure 5.1 and in Figure 5.2 respectively.

Short-circuiting occurred rarely and sparsely for the pulling position at any tested welding speed, without any of these events shown in the time sample presented in Figure 5.1. The pushing position resulted in higher short-circuiting frequency, which increased with the welding speed. Short-circuiting events are very brief, voltage drop is small, current increase is mostly undetected and the arc does not seem to completely extinguish during the event. Figure 5.3 shows high-speed imaging frames of one short-circuit occurring. It is difficult to create a criterion to distinguish short-circuits apart from random voltage variation and other phenomena.

Figure 5.1: Current and voltage oscillogram for pulling buried GMAW at three welding speeds.

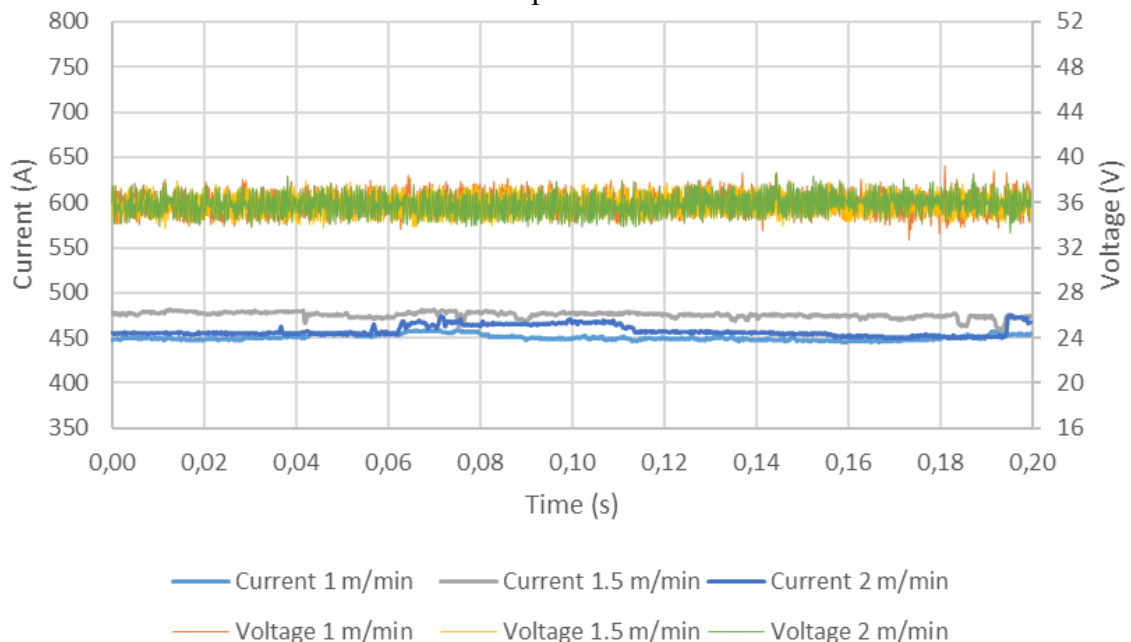


Figure 5.2: Current and voltage oscillogram for pushing buried GMAW at three welding speeds.

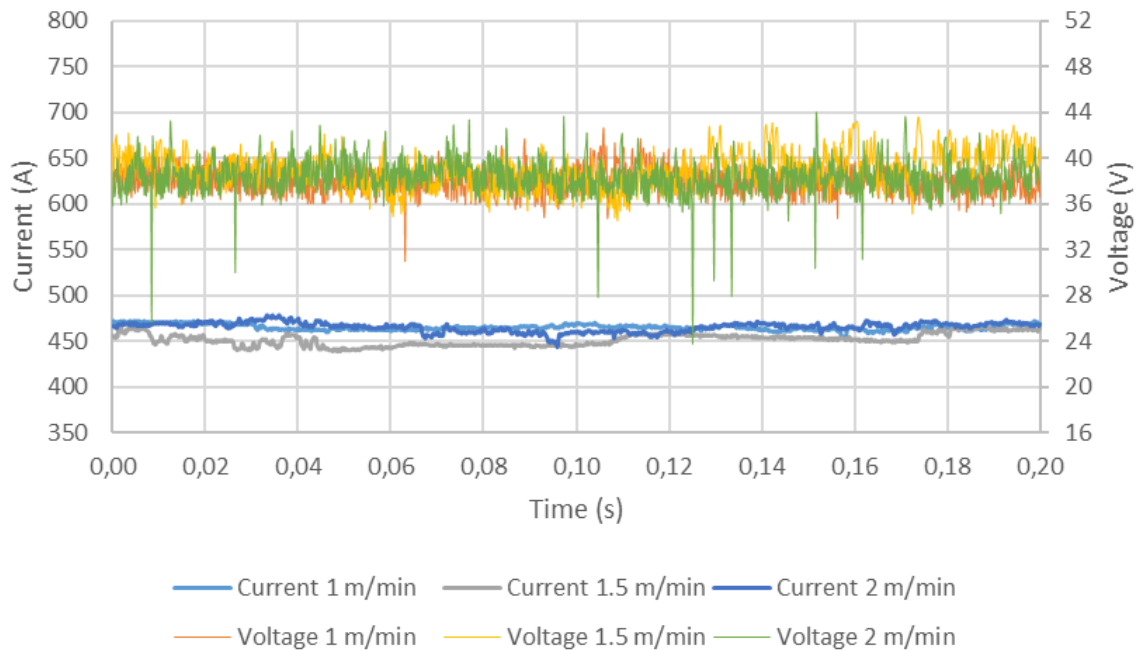
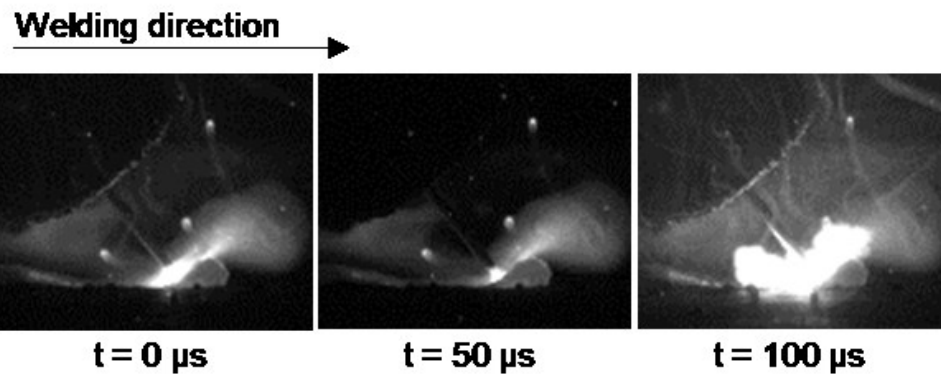


Figure 5.3: High-speed imaging of a short-circuiting event.



The author estimated a maximum of **40** short-circuits per second for the pushing arc GMAW at **2.0 m/min**. Although this frequency approaches that of regular short-circuiting GMAW, the droplet transfer frequency at the present current level should be around **275 Hz** (LESNEWICH, 1958) *apud* (LIU; SIEWERT, 1989), an order of magnitude higher. Therefore, it can be assumed that the spray transfer is predominant even in the worst case.

It is interesting to note that the current remains mostly unchanged, even during a short-circuit and considering that the current rise inductance was set to a very low value. This might be attributed to the welding source dynamics and to the fact that it is in fact a current source emulating a conventional constant voltage source. Perhaps, the events are so brief that the welding source is not capable to respond quickly enough.

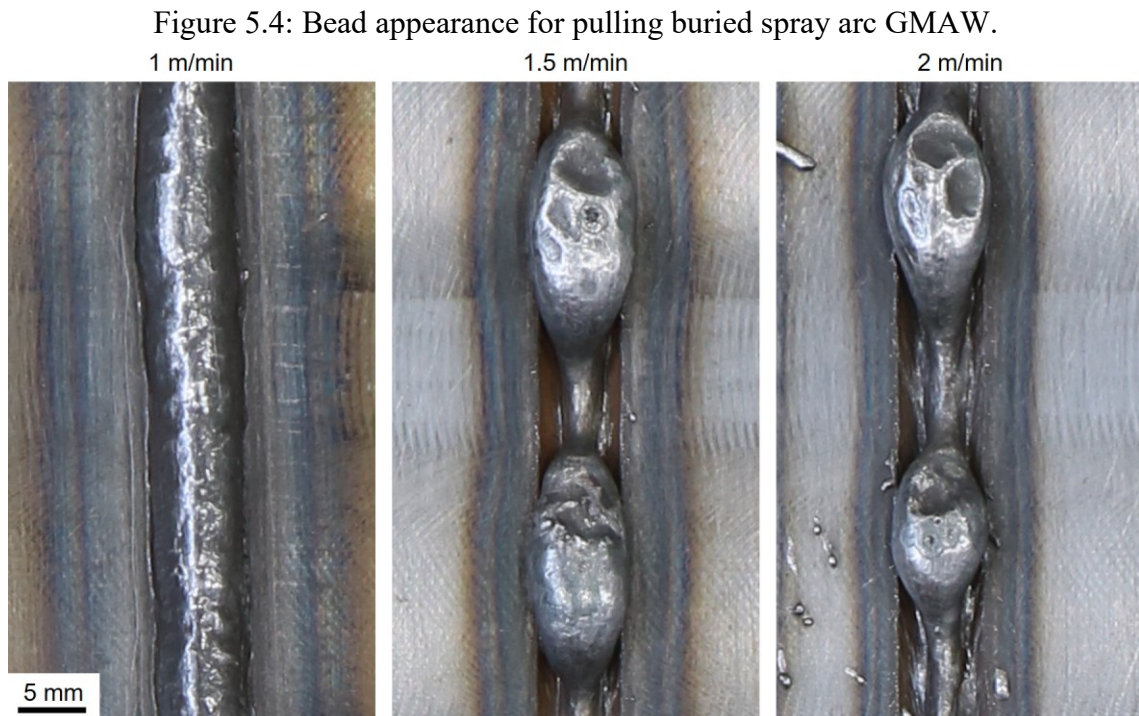
5.1.2 Pulling and Pushing Configurations

Arc shear stress and, to a lesser degree, arc stagnation pressure are the dominant factors determining pool flow in high current arc welding (MENDEZ; EAGAR, 2000; MENG; QIN, 2019; MENG; QIN; ZOU, 2016), so torch positioning is expected to play an important role in buried spray arc GMAW.

5.1.2.1 Pulling Torch

In the high-speed camera acquisitions, it is clearly shown that a pulling torch results in strong backward plasma jets, being faster for longer arcs and higher welding speeds, while forward jets were not significant or inexistent, as evidenced in the measurements from Table 4.3.

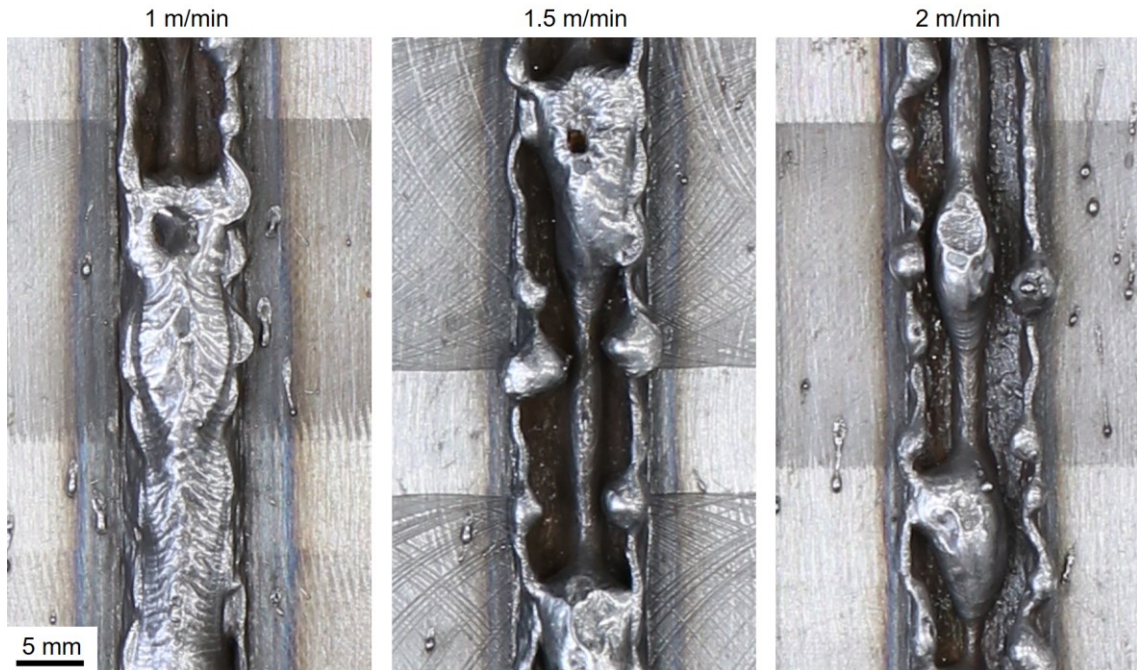
Strong backward flows on the pool surface are driven by the arc plasma drag force, which can adversely affect weld quality. For the buried arc, backward flow coupled with high welding speed resulted in BCM humping at **1.5 m/min** and **2.0 m/min**, similar to and starting at the same welding speed as the ones from Cho and Farson (2007). Figure 5.4 shows the bead appearance for the buried spray arc at the three welding speeds.



Welding with a longer arc resulted in split beads and humping at every welding speed, as shown in Figure 5.5. The beads were split in three, with dominating GRM humping characteristics at lower speeds and BCM humping in the central bead at higher speeds. Regarding split

beads and GRM humping, it is an interesting result, because Mendez and Eagar (2003) attributed the occurrence of such defects to higher arc pressures, which would push the transition between gouging and trailing region further from the heat source. Since shorter arc lengths result in higher arc pressures (ADONYI; RICHARDSON; BAESLACK, 1992; JARVIS, 2001), higher split beads and GRM humping tendency would be expected for the buried arc instead.

Figure 5.5: Bead appearance for pulling long spray arc GMAW.

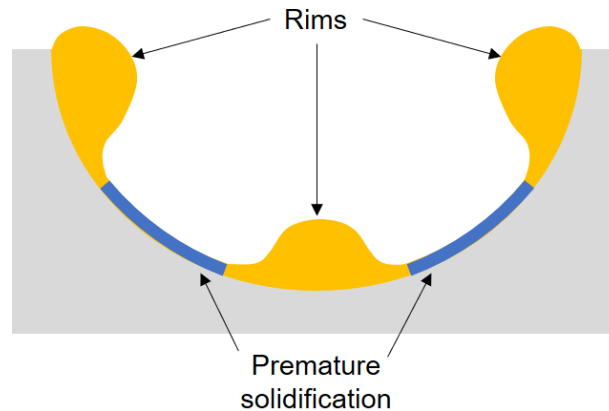


By definition, arc stagnation pressure acts orthogonally to the liquid surface, while arc shear stress acts parallel to the surface. Consequently, stagnation pressure induces the pool depression, while shear stress drives the pool flow. Therefore, the gouging region flow speed should be governed by the drag force. Hence, the present results suggest that the gouging region flow speed should be an important factor determining the transition point and that the plasma shear stress should be considered when modelling GRM humping.

The premature solidification of the gouging region, which leads to GRM humping and split beads is said to begin in the gouging region centerline (MENDEZ; EAGAR, 2003; MENG; QIN; ZOU, 2016), so a central bead associated with split beads and GRM humping was unexpected. The obtained pattern is only possible if premature solidification began in the sidewall's middle portions, and rims of molten metal were present at the weld centerline and at sidewalls upper portions. The schematics of a gouging region cross section under these conditions is presented in Figure 5.6. The author suspects that the central rim is produced by the filler metal impinging on the near solidification or already solidified gouging region, delivering heat and

material to the weld centerline. If this supposition is true, the central bead should be richer in filler metal than the side beads, and localized chemical analysis (Energy Dispersive X-Ray Spectroscopy - EDS, for example) using a marker element in the filler metal could confirm it.

Figure 5.6: Cross section of a gouging region with three rims.



No undercuts were observed in any of the welds done with a pulling torch, except for the undercuts inherent to BCM humping.

5.1.2.2 *Pushing Torch*

When welding with the torch in the pushing position, the backward jet is reduced and a forward jet arises, when compared to the pulling position, as was presented in Table 4.3. The resulting beads for pushing torch welding with a buried spray arc and with a long spray arc are shown in Figure 5.7 and Figure 5.8 respectively.

The reduced backward plasma jet resulted in lessened BCM humping tendency, with the absence of such discontinuity in all weld produced with a pushing torch. Undercutting was also absent.

As was observed for the pulling torch, longer arc resulted in more gouging region related problems than buried arc. The sparsely distributed dry spots and bead irregularities at **1.5 m/min** and **2.0 m/min** are believed to arise from gouging-trailing transition point near the threshold before GRM humping and split beads develop.

Figure 5.7: Bead appearance for pushing buried spray arc GMAW.

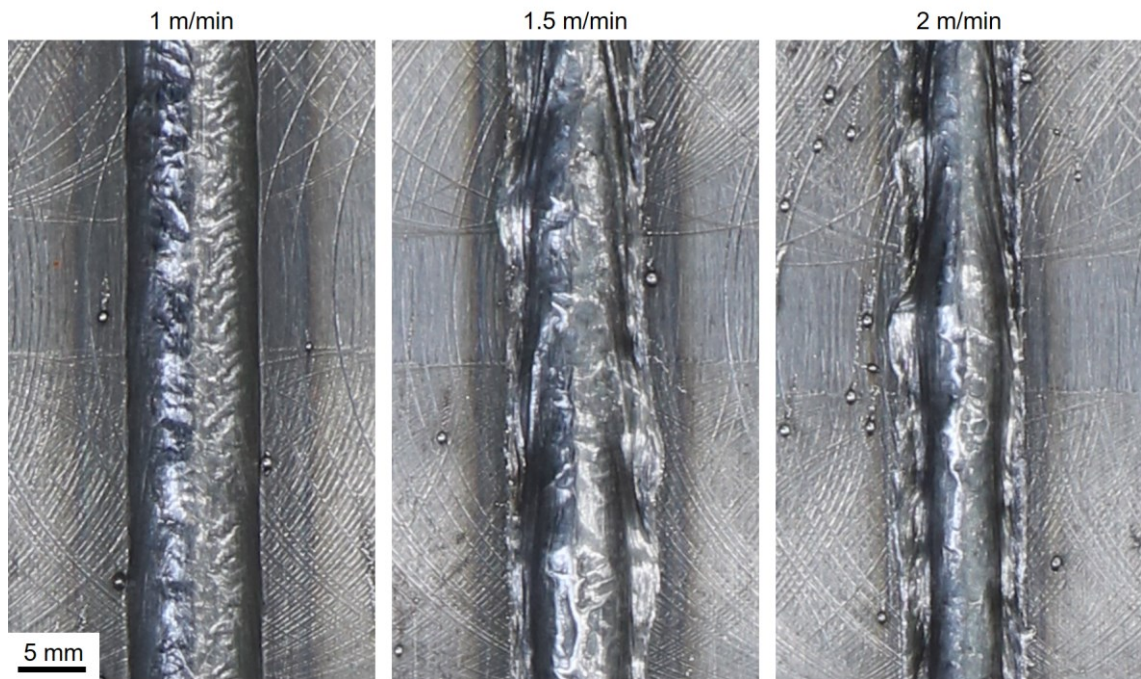
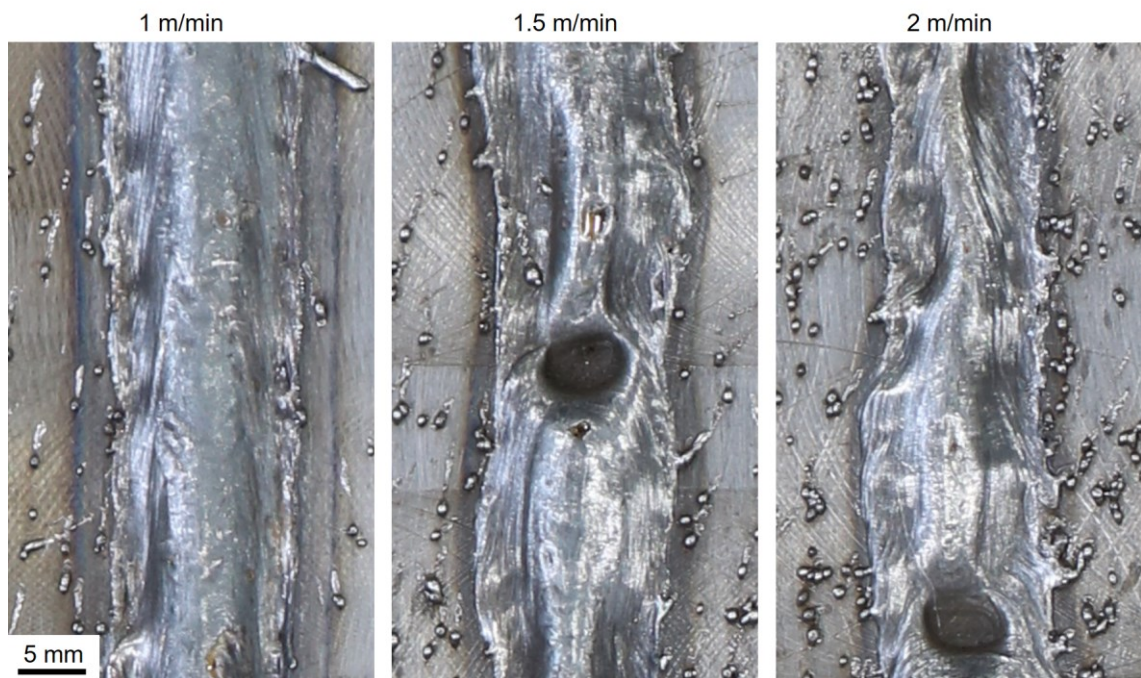
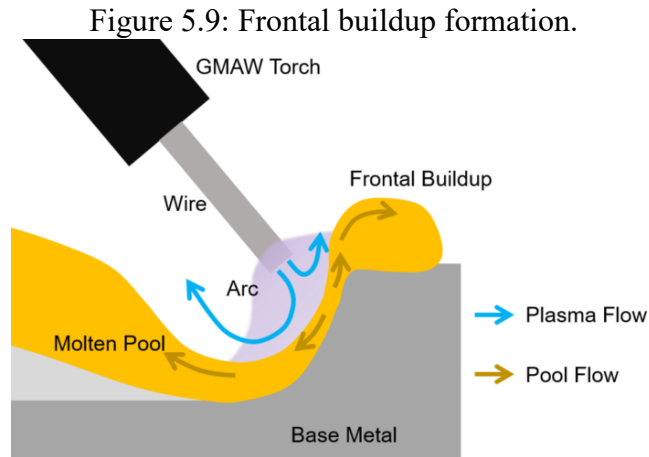


Figure 5.8: Bead appearance for pushing long spray arc GMAW.



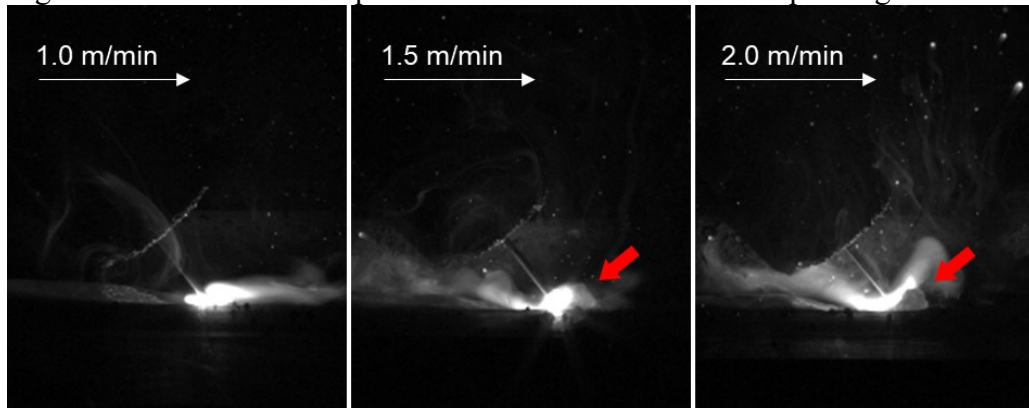
The emergence of a forward flowing plasma jet can influence molten metal flow at the pool front and lead to a localized upward-forward flow. As the flowing metal reaches the sudden end of the molten pool front, it rises above the workpiece surface and tumbles forward. Due to the high welding speeds used and thermal inertia, only thin films of molten metal exist in the pool front (gouging region), leaving little room for the upward-forward flow to recirculate and

flow backwards, towards the trailing region. Therefore, molten metal builds up ahead of the pool. The formation of this frontal buildup is illustrated in Figure 5.9.



Occurrence of the frontal buildup phenomenon in the buried spray arc GMAW is shown in the high-speed imaging frames from Figure 5.10. No frontal buildup was noticed at **1.0 m/min** welding speed, due possibly to the wider and deeper molten pool that gives room to the excess metal to flow backwards around the depression before it builds up considerably. At **1.5 m/min** and **2.0 m/min**, the frontal buildup is observed during most of the process.

Figure 5.10: Frontal buildup at 1.5 m/min and 2.0 m/min for pushing buried arc.



When a longer arc was used, the faster plasma jets caused the upward-forward flowing metal to achieve enough speed to be ejected from the molten pool, so severe spatter was observed, regardless of the welding speed. At **1.5 m/min** and **2.0 m/min**, frontal buildup could also be observed with high-speed imaging. Tracking of two droplets being ejected from the molten pool are presented in the high-speed images from Figure 5.11. Dashed circles represent

the previous locations of the droplets. The crater left by the arc extinction in Figure 5.12 shows the frontal buildup stretched forward and flattened down due to the strong plasma jets.

Figure 5.11: Tracking of two droplets being ejected from the pool.

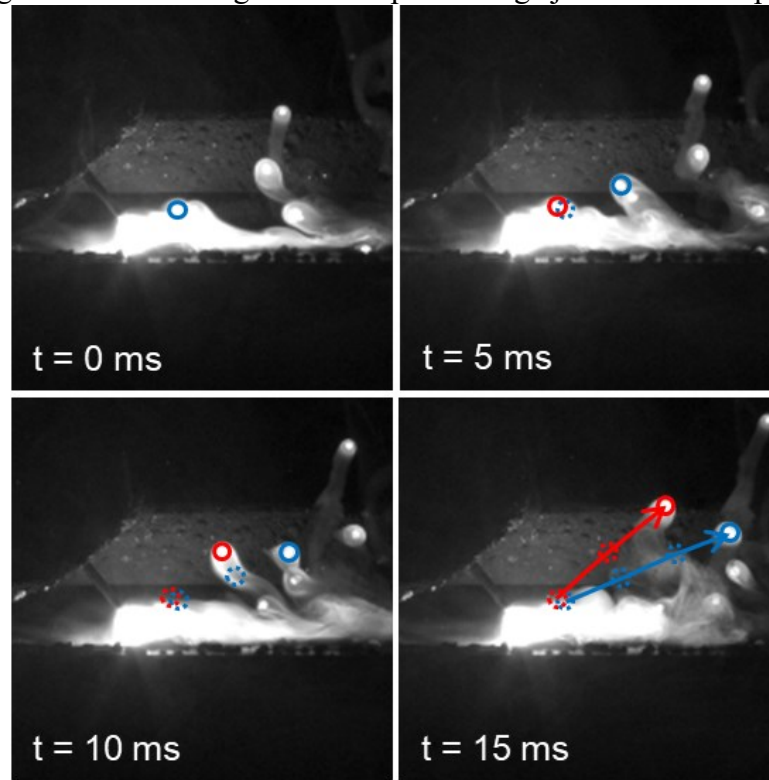


Figure 5.12: Stretched frontal buildup in the pushing long arc GMAW crater.



5.2 LASER INTERACTIONS WITH A BURIED SPRAY ARC

5.2.1 Laser Effects on Arc Electric Properties

The experiments performed with GMAW and HLAW on a single bead gives an excellent opportunity to observe the laser influence on the electric arc properties by minimizing the influence of random factors. A good comparison between HLAW and GMAW can be achieved by taking the results from Table 4.4 and finding the difference between the former and the later

average current (ΔI_m), average voltage (ΔU_m) and average arc length (ΔL). The results are presented in Table 5.2, where it can be noticed that no significant variation in any of these parameters was found.

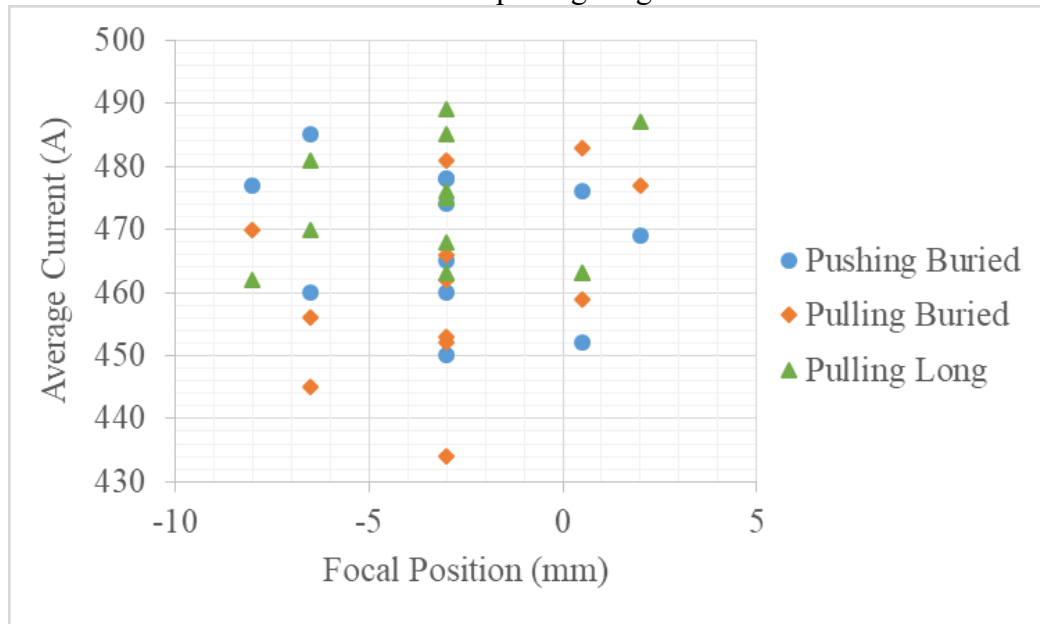
Although laser interaction with the arc seems to be negligible, it might be different if the relative positioning between the two heat sources is changed, especially the D_{LA} . The average currents from the CCD experiments are plotted in Figure 5.13 as a function of D_{LA} for the pushing buried, pulling buried and pulling high-current long arc.

There is no observable correlation for pulling buried (**0.09**) and for pulling long (**-0.02**) arcs between the two factors. For pushing buried arc, I_m and D_{LA} showed a strong correlation (**-0.84**) though. This reduction in current might be due to premelting of the pool front by the laser beam, which allows the arc pressure to push the pool depression further, increasing the effective distance between electrode and workpiece. The frontal buildup can also reduce the arc travel distance and it is also reduced at increased laser-arc separation (see Section 5.2.2.3). However, it is still possible that this correlation is simply an artifact due to small sample size and high variability.

Table 5.2: Average current, voltage and arc length difference between HLAW and GMAW.

Torch	Arc	V (m/min)	ΔI_m (A)	ΔU_m (V)	ΔL (mm)
Pulling	Buried	1.0	5.0	0.1	0.1
		1.5	-9.0	0.0	0.2
		2.0	-3.0	0.0	0.3
	Long	1.0	7.0	0.0	0.2
		1.5	0.0	0.0	0.3
		2.0	-2.0	0.0	0.2
Pushing	Buried	1.0	4.0	1.1	0.5
		1.5	0.0	0.3	0.1
		2.0	-1.0	-1.1	0.2
	Long	1.0	-3.0	0.6	0.4
		1.5	7.0	1.7	-0.1
		2.0	5.0	1.1	-0.4

Figure 5.13: Average current as a function of laser-arc distance for the pushing buried, pulling buried and pulling long arc.



At very short D_{LA} , the laser beam can intercept the welding wire, leading to premature filler metal detachment, increasing arc length and, thus, reducing current. This laser-wire interaction was observed for the pulling buried arc (due to the shortest arc length) at D_{LA} of **0** and **-1**, resulting in the two lowest current points in Figure 5.13.

Despite the similar average current and voltage, the oscillogram acquired by the welding source showed some behavior change when the laser was added to the pushing buried arc GMAW process. An oscillogram comparing the current and voltage of the pushing buried arc GMAW and HLAW at **2.0 m/min** welding speed is shown in Figure 5.14 and main measured arc properties summarized in Table 5.3 (where P_A stands for average arc power). The short-circuiting events are present in GMAW as was discussed in Section 5.1.1.2, but they are suppressed when the laser beam is added to the process. Instead of voltage drops due to short-circuits, the oscillogram shows a cyclic voltage variation with a period of around **15 ms** and **25 ms**. This phenomenon is observed in every pushing buried arc HLAW weld performed, although it becomes intermittent and with lower amplitudes at D_{LA} higher than **5 mm** or at **-1 mm** (laser intersecting the wire).

Figure 5.14: Current and voltage oscillogram for pushing buried arc GMAW and HLAW.

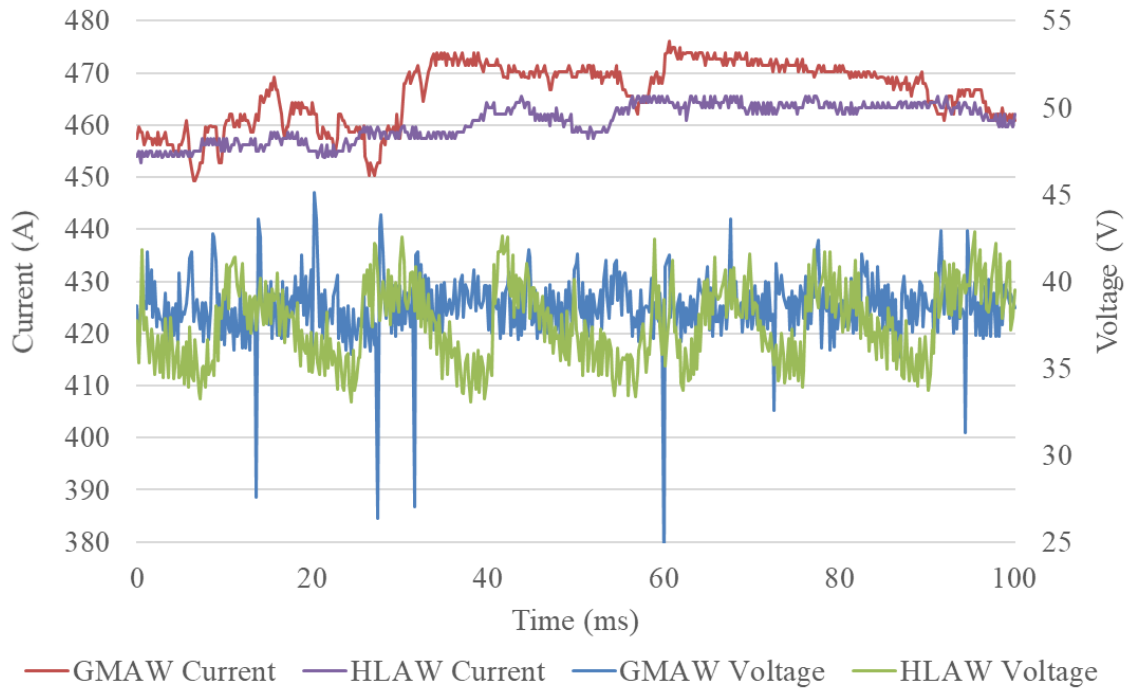


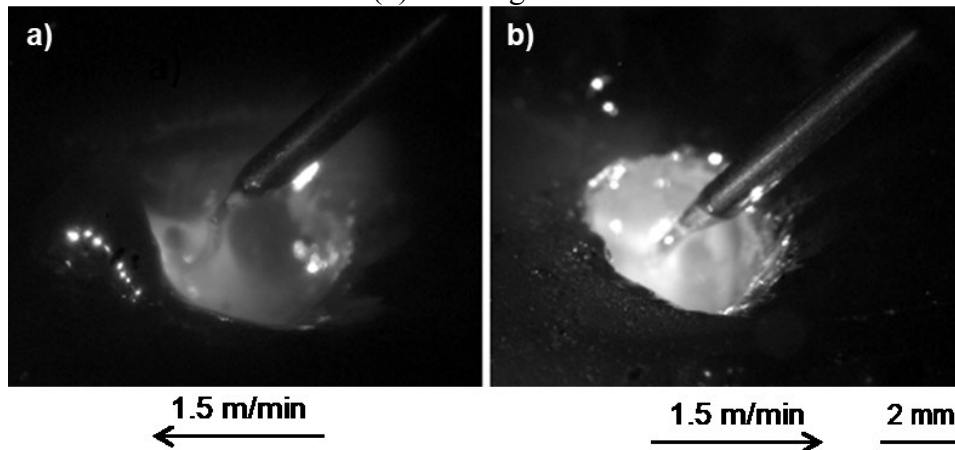
Table 5.3: Main arc properties.

Process	I_m (A)	U_m (V)	P_A (kW)
GMAW	463	38.4	17.7
HLAW	462	37.2	17.2

If this cyclical oscillation is related to metal transfer, it could indicate a change to the globular free flight transfer mode, as an average droplet diameter of **2.35 mm** would result from a **20 ms** detachment cycle. It has already been shown that the laser beam can hinder the droplet detachment in HLAW (CAI et al., 2016; LEI et al., 2017; LIU et al., 2012), but it was never observed to prevent spray transfer mode at such high currents.

Additional high-speed videos were taken with the support of a Cavitar Cavilux illuminating laser in order to verify if the metal transfer mode changes to globular in the pushing buried arc when the laser is added to the process. As can be seen in the extracted frames presented in Figure 5.15, the transfer mode of the HLAW process is clearly of the streaming spray mode, debunking the aforementioned hypothesis for the voltage oscillation seen in Figure 5.14. More investigation is necessary to explain said oscillation. Interestingly, the GMAW videos revealed frequent kink instabilities, in addition to the apparent short-circuiting events, which were much rarer in the HLAW footage, indicating that the laser presence might prevent the kink instabilities from developing.

Figure 5.15: High-speed imaging of the pushing buried arc condition in GMAW (a) and in HLAW (b) showing metal transfer.



5.2.2 Laser Effects on Pool Flow and Discontinuities

As the laser beam is added to the arc welding process to achieve the HLAW process, new convection driving forces are added and existing driving forces can be influenced, changing the flow pattern, and, thus, flow related discontinuities. BCM humping, GRM humping, split beads, undercut and the frontal buildup will be discussed.

5.2.2.1 BCM Humping

From Figure 5.16, where the weld beads from pulling buried arc GMAW and HLAW at different laser-arc distances at **1.5 m/min** are compared, it can be observed that BCM humping is reduced by the laser beam, and the reduction is greater as the D_{LA} increases. At **0.0 mm**, slight improvement is observed. At **2.5 mm**, the humping becomes intermittent and the humping free regions show undercuts. At **5 mm** and further, no humping nor undercuts are present and good welds are obtained. However, at such large D_{LA} , weld penetration depth starts to become compromised.

By analyzing the process with high-speed imaging, as in the frames from Figure 5.17, it is clear that the trailing region behavior changes dramatically. For GMAW and HLAW with short D_{LA} , the molten pool depression (marked by the point where the pool rises above the workpiece surface, with the distance to the arc interaction point shown in yellow) is much longer and the humping is formed just after that point. At longer D_{LA} , the pool depression ends abruptly behind the vapor capillary and then slowly climbs to a stable height.

Figure 5.16: Bead appearance for pulling buried spray arc GMAW and HLAW at different D_{LA} .

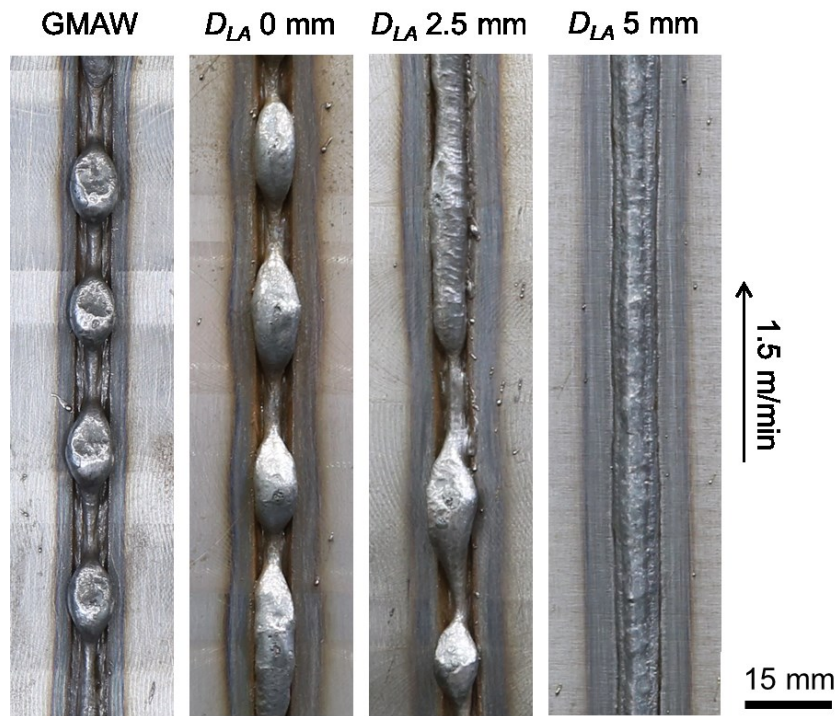
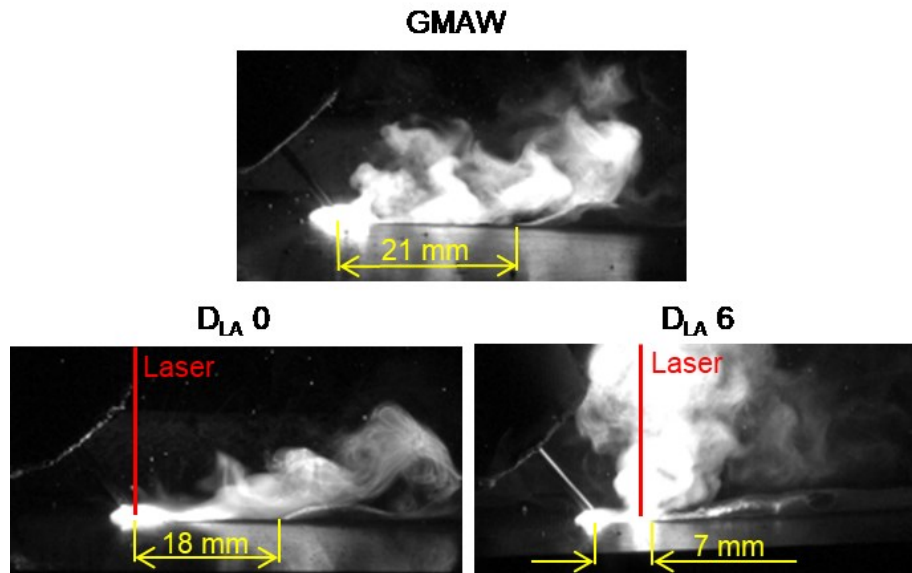


Figure 5.17: High speed imaging comparing GMAW to HLAW at 0 and 6 mm D_{LA} .



BCM humping in arc welding is oftentimes linked to a necking region, which prevents metal recirculation and leads to the formation of a built up hump at the pool rear portion (CHEN; WU, 2011; CHO; FARSON, 2007). LBW pools, on the other hand, are deep and allow surface flows to recirculate through the pool interior (ARTINOV et al., 2018). In HLAW, the deep pool might allow forward flow of metal below the necking region, refilling it, thus preventing its development and rear material build up. However, the laser induced deep portion of the pool is

very short, stretching to only a few millimeters, as was shown in Figure 2.39 (**18 kW LBW at 2.0 m/min**), so, at short laser-arc distances, it might not reach the necking region and the recirculation effect is thwarted. Although penetration depth is reduced at larger D_{LA} (at **2.5 mm**, PD is **12.4 mm**; at **5 mm**, PD is **10.3 mm**), it is still decent, and the resulting bead has a very good appearance.

If this effect is proved at lower laser powers, it can also be exploited for laser-assisted GMAW⁵ applications at high welding speed. Choi *et al.* (2006) have already shown that a laser beam can assist the GMAW for humping and undercutting prevention, but the prevention mechanism was different, as the laser beam was positioned defocused ahead of the arc to widen the pool. Their solution, however, increases heat input significantly and do not take advantage of the main characteristics of the laser beam, so cheaper heat sources (e.g. GTAW and PAW) could probably be used with similar results.

5.2.2.2 Gouging Related Discontinuities

Figure 5.18 and Figure 5.19 show how the bead appearance changes in pulling high-current long spray arc GMAW and HLAW at different welding speeds and different laser-arc distances respectively. It can be seen that the laser beam effectively suppresses GRM humping and split beads formation, although BCM humping and undercutting can start forming in HLAW welds at **1.5 m/min** and higher welding speeds.

By analyzing the crater left as the arc extinguished, it is possible to estimate the pool flow during the GMAW and the HLAW processes, as shown in Figure 5.20. When only the arc is present, the gouging region extends further than the heat influence of the arc and solidifies, except for the central and the sidewall rims. The surface tension refrains the rims of merging and split beads are formed, while each of these split beads can present BCM humping (as discussed in Section 5.1.2.1). As the laser beam is added to the process, the central rim is widened by the added heat and it becomes a deep molten pool. The deeper pool allows metal recirculation, leading to a higher central rim, similarly to what was observed for the BCM humping in HLAW (Section 5.2.2.1). As the central rim becomes higher and wider, it merges with the sidewall rims flow and a single trailing region is obtained, thus no more split beads are seen.

⁵ Laser-assisted arc welding (GMAW, GTAW, SAW, etc.) is a common nomenclature for HLAW processes where the arc is responsible for most of the heat input and penetration depth.

Figure 5.18: Bead appearance for pulling long arc GMAW and HLAW at different welding speeds.

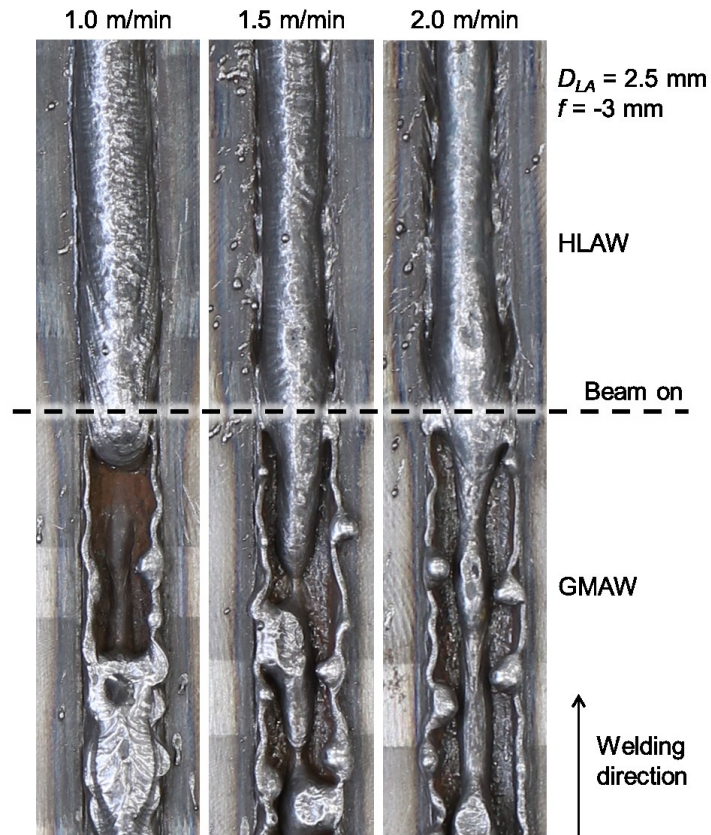


Figure 5.19: Bead appearance for pulling long arc GMAW and HLAW at different D_{LA} .

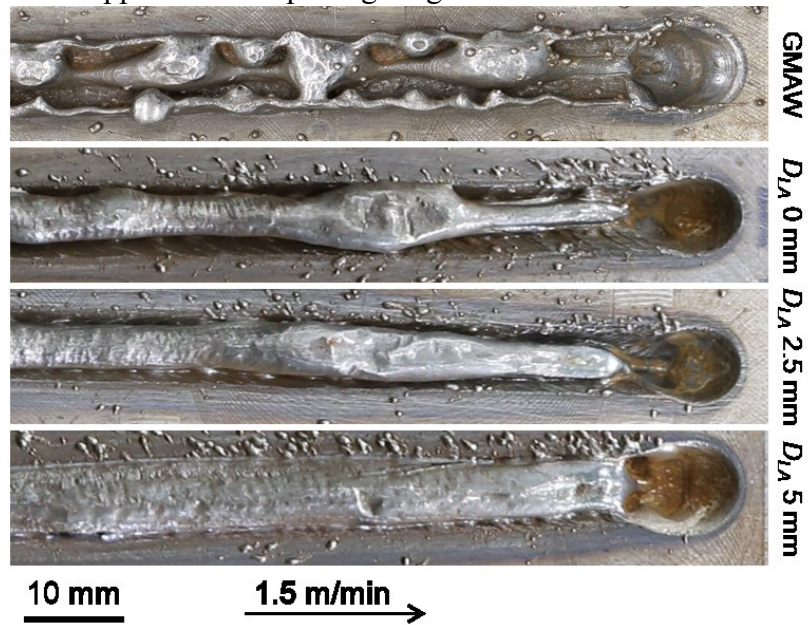
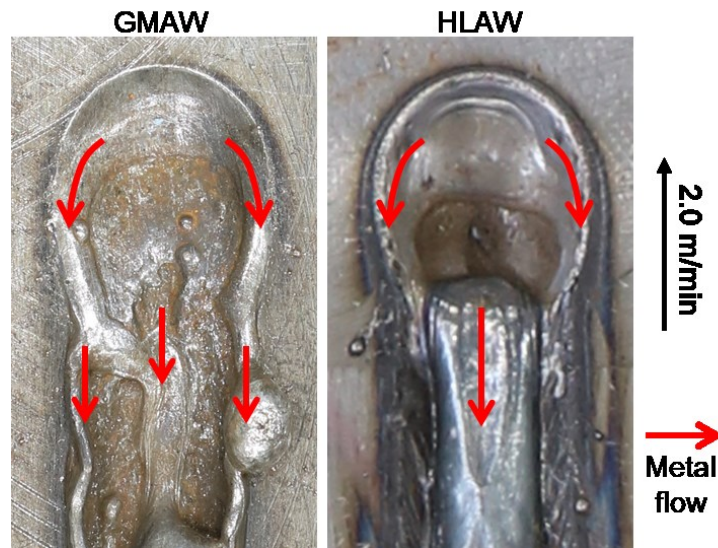
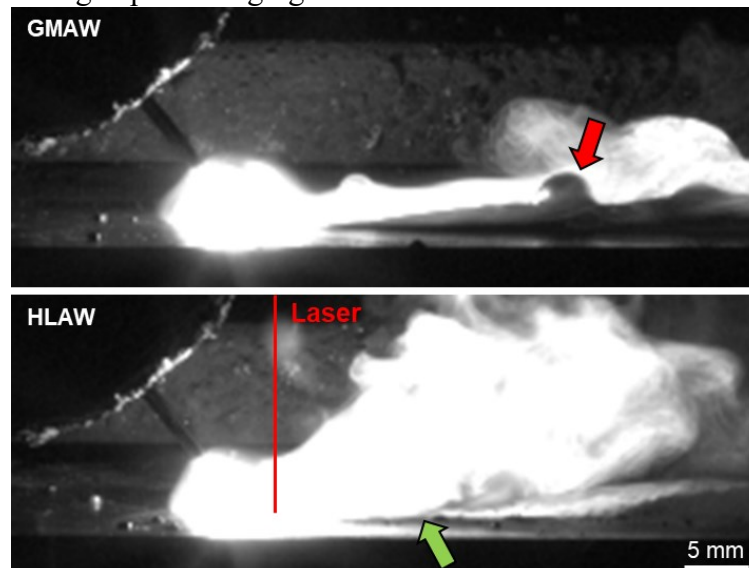


Figure 5.20: Fluid flow in the gouging region for GMAW and HLAW with high-current long arc.



High-speed imaging of the process agrees with the presented hypothesis. In the frames from Figure 5.21, the humping side bead growing during the GMAW process can be seen, while it is absent in HLAW. Central bead rise (marked by a green arrow) is shown to occur not far from the laser beam interaction point, while no perceivable rise of the central bead is observed for GMAW. The plasma jet is deflected upwards by the central bead height in HLAW.

Figure 5.21: High-speed imaging frames for GMAW and HLAW at 1.5 m/min.



The behavior of the pulling high-current long arc HLAW becomes very similar to that of the pulling buried arc HLAW, with the single central bead being susceptible to BCM humping, which improves with increased D_{LA} (refer to Section 5.2.2.1). The BCM humping is still

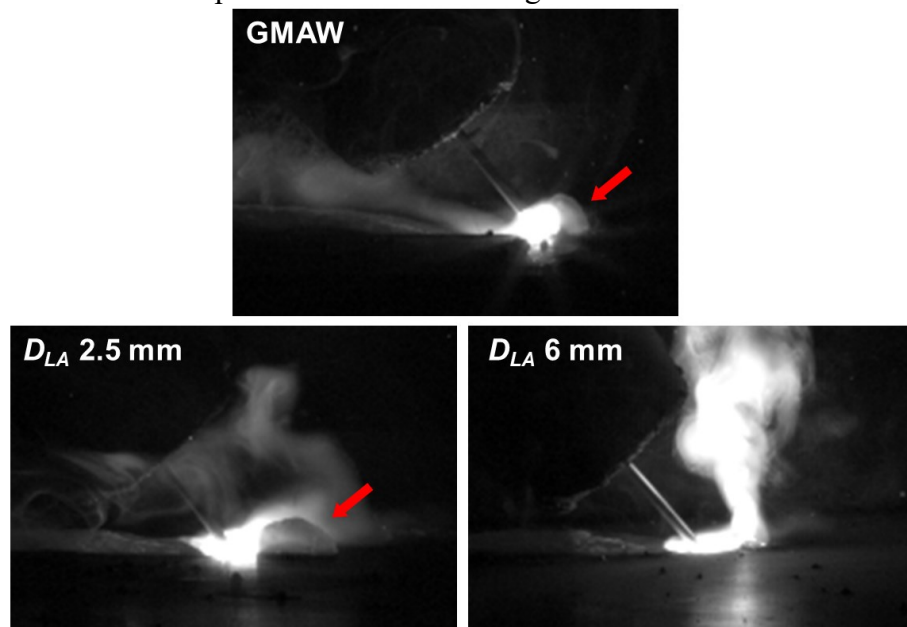
lower than that of the pulling buried arc, probably due to the fact that wider pools are less susceptible to BCM humping (GRATZKE et al., 1992).

Although less humping is observed with long arc than with buried arc in torch leading (pulling) HLAW, the former shows more undercutting. As the sidewall rim metal is captured by the central pool, the borders are left with very little material, which can solidify before it can be refilled. The upward plasma jet exacerbates the problem by ejecting the little material left on the pool borders. Some material ejection in the form of spatter is shown in both Figure 5.18 and Figure 5.19 for HLAW, but not for GMAW. Contrary to the spatter found in pushing long arc welding, this spatter does not travel far away from the molten pool. With increased laser-arc distance, the central pool becomes wider and less undercutting is observed. At **5 mm** and more, both undercutting and humping can be prevented.

5.2.2.3 Frontal Buildup and Forward Spatter

Laser interaction with the frontal buildup was observed to vary with the distance between both heat sources. Compared to GMAW process, buildup was larger at short D_{LA} and smaller or inexistent at long D_{LA} , as shown in Figure 5.22.

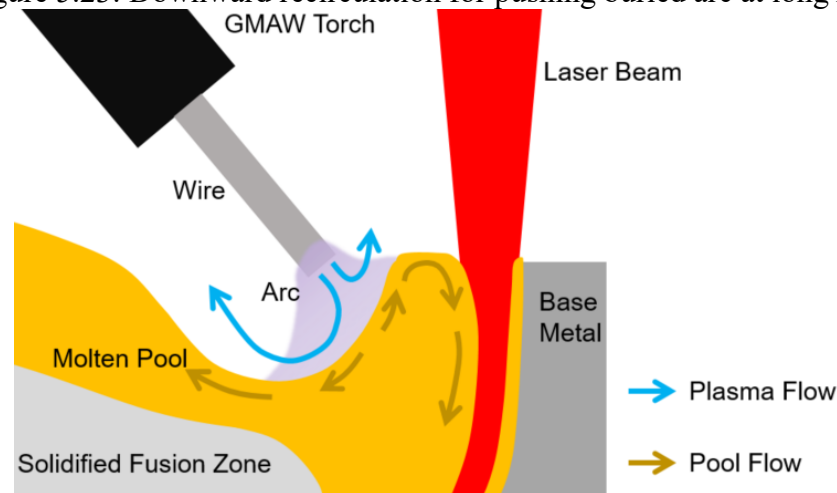
Figure 5.22: Frontal buildup under different welding conditions at 1.5 m/min welding speed.



As discussed previously, frontal buildup might be related to an upward and forward flow in the front of the gouging region, which has no room to recirculate as it reaches the abrupt end of the molten pool front at high speed (Section 5.1.2.2). At long D_{LA} (**5 mm** and **6 mm**),

the laser beam creates a deep and narrow molten pool ahead of the gouging region, so the forward flow has room to recirculate, possibly in the form of a downward flow near the vapor capillary hear wall, as in the schematics from Figure 5.23.

Figure 5.23: Downward recirculation for pushing buried arc at long D_{LA} .



On the other hand, at short D_{LA} (**-1 mm, 0 and 2.5 mm**) the frontal buildup increases to sizes that can leave visible irregularities on the weld bead if ejected to the side, as occurred in the bead from Figure 5.24. It has been observed that shorter distances between the laser beam and the arc cause the arc length above the workpiece surface to increase (correlation index of **-0.88**), which in turn leads to stronger forward plasma jets, so it is reasonable to expect more buildup under these conditions. The pushing long arc induced spatter can be perceived as an extreme case of this phenomenon. The increased buildup size can also be linked to the high-speed vapor jet leaving the capillary near the gouging region front, acting as another driving force for the upward flow.

As the overgrown frontal buildup swings randomly back and forth, it can cross the beam path, leading to irregular penetration profiles. Longitudinal cuts were made to investigate this behavior, comparing the pushing buried, the pulling buried and the pulling high-current long arcs, presented in Figure 5.25. As can be seen, there is a much larger penetration variation along the weld length for pushing buried arc than for other conditions. More and bigger porosities are also present. When the laser hits the frontal buildup, the vapor capillary can partly or completely collapse, entrapping gases. Unstable vapor capillaries have been shown to cause porosity before and the characteristics of the present samples (round and concentrated on the bottom half of the weld) agree with the literature (BUNAZIV et al., 2018a; MATSUNAWA et al., 2003; RIBIC; PALMER; DEBROY, 2009).

Figure 5.24: High-speed imaging of a frontal buildup ejection and the resulting bead.

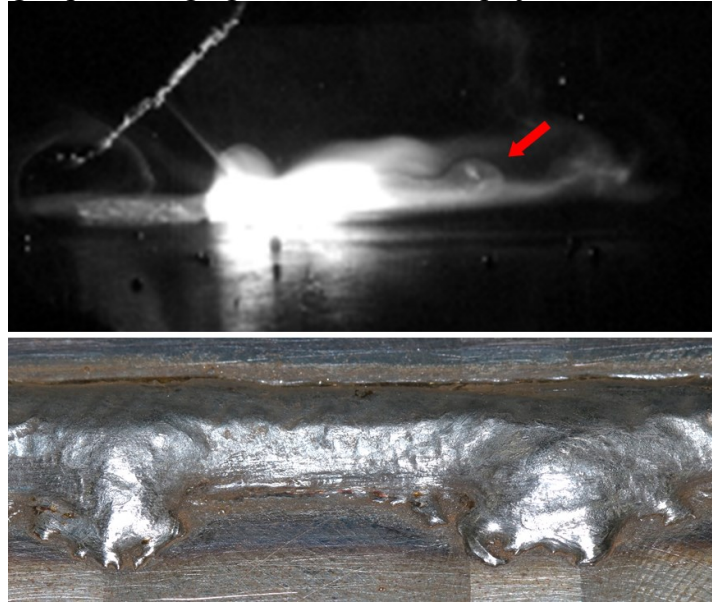
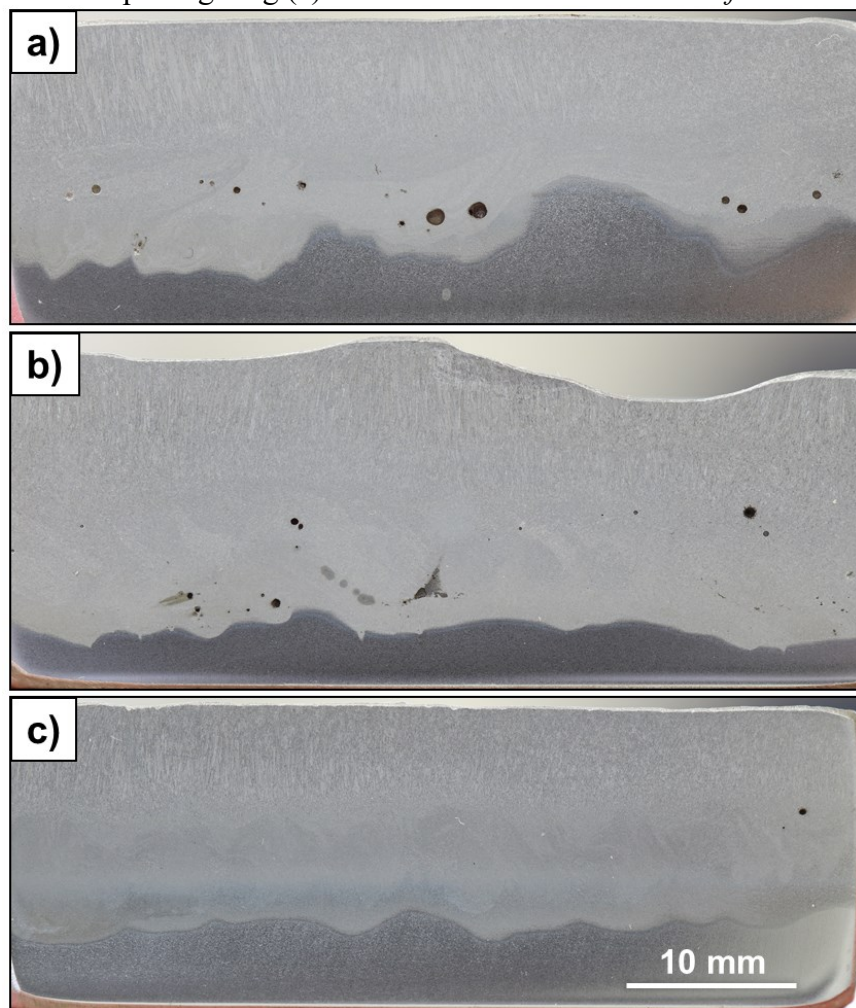
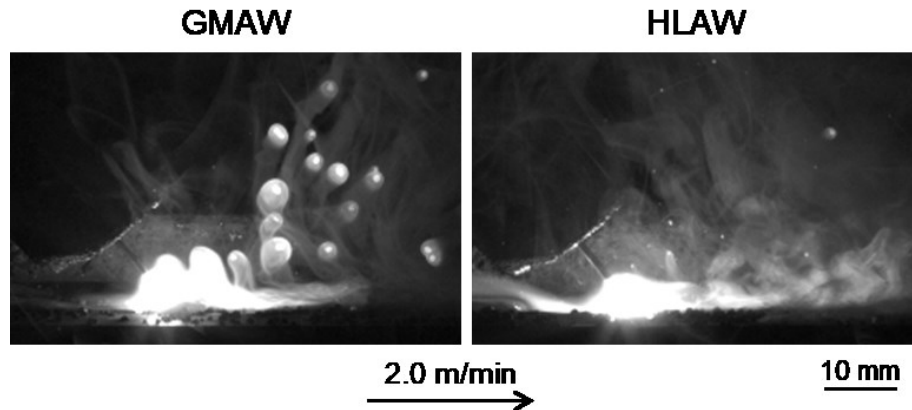


Figure 5.25: Penetration longitudinal profile for pushing buried (a), pulling buried (b) and pulling long (c) arcs at 2.5 mm D_{LA} and -3 mm f .



For the pushing long arc, the addition of the laser beam to the process decreased considerably the spatter formation, but increased the frontal buildup, as shown in the high-speed imaging frames from Figure 5.26.

Figure 5.26: Pushing long arc GMAW and HLAW spatter.



5.3 BURIED SPRAY ARC HLAW PROCESS

In this section, the buried spray arc HLAW process is discussed regarding the penetration gains, other possible advantages and observed difficulties.

5.3.1 Penetration

The response surfaces obtained with the second order CCD RSM were not adequate, as there was no significance and no good fit for all three experimented arc conditions. The author suspects that high process variability allied with a small sample size are the main culprits behind these results.

Even though the fitted response surfaces were not satisfactory, these experiments were important to observe laser-arc interaction, especially regarding the molten pool behavior and associated discontinuities. Important observations about the penetration capability of each condition could also be drawn from the results. For instance, one can observe that D_{LA} has a much stronger influence on PD than f .

It could also be perceived that the optimal positioning for the pushing buried, pulling buried and pulling high-current long arc should be close to the central point of the second order CCD experiment, which is also the same to the four reproductions of the conventional spray arc. It is then possible to compare the four welding conditions using the four reproductions of each at $D_{LA}=2.5$ mm and $f=-3$ mm. Table 5.4 summarizes the relevant information used for the comparison.

Table 5.4: Mean and standard deviation of penetration depth for all four welding conditions reproductions at the central point.

Welding Condition	Mean <i>PD</i> (mm)	σ <i>PD</i> (mm)
Conventional	8.62	0.65
Pushing Buried	10.55	1.80
Pulling Buried	12.37	0.25
Pulling Long	11.27	0.91

The comparison was made by comparing each welding conditions pair separately through the Welch Two Sample t-Test based on Montgomery's (2013) description. The comparison results are shown in Table 5.5. For better presentation of the results, "Conventional Spray Arc" was shortened to "Conv.," "Pushing Buried Spray Arc" to "Push B.," "Pulling Buried Spray Arc" to "Pull B." and "Pulling High-Current Long Spray Arc" to "Pull L.".

Table 5.5: Results of each comparison pair.

Comparison Pair	Estimate Difference (mm)	p-Value
Push B. – Conv.	1.93	0.119
Pull B. – Conv.	3.75	0.000502
Pull L. – Conv.	2.65	0.004172
Push B. – Pull B.	-1.82	0.1349
Push B. – Pull L.	-0.72	0.5084
Pull B. – Pull L.	1.10	0.09075

Both pulling buried spray arc HLAW (**99.95 %** confidence) and high-current long spray arc HLAW (**99.58 %** confidence) achieved significant deeper penetration than conventional spray arc HLAW (**250 A** with longer arc), attesting that increased current does increase penetration depth. To confirm that burying the arc increases penetration even further, pulling buried arc condition must be significantly deeper than pulling long arc condition. With a **90.93 %** confidence level, it is probable that the buried arc does result in deeper welds, however, it cannot be confirmed using the usual **95 %** confidence criterion for the obtained results. More testing is required for confirmation.

Not only did the pulling buried spray arc HLAW result in the deepest welds, it also showed the least penetration depth variability, indicating a more stable and reliable process.

On the contrary, due to high variance in penetration depth, the pushing buried spray arc HLAW penetration can neither be confirmed to be above that of the conventional spray arc,

nor can be confirmed to be below both pulling high-current conditions with the available information.

It is worth mentioning that the deepest measured weld with pushing buried arc HLAW reached **12.6 mm**, just **0.1 mm** less than the deepest with pulling buried arc. This hints that, if the frontal buildup was suppressed, pushing buried arc HLAW could achieve similar *PD* as its pulling counterpart.

5.3.2 Other Advantages

The most striking difference between the conventional and the buried arc welds is the arc zone depth (see Figure 4.5). In A709, it reaches **6.9 mm (77 % of plate thickness)** of depth for the buried arc, against **2.4 mm (27 % of plate thickness)** for the conventional HLAW. This can lead to some benefits.

Firstly, it should considerably reduce solidification crack susceptibility. It has been shown that solidification cracks usually happen in a bulged area in the weld interior, as discussed in Section 2.3.4.2. On the present experiment, the arc zone completely overlapped the area where the necking and the bulging are usually found, leaving a much more benefic V-shape weld with no late solidification areas within the weld. A solidification crack on a bulging region is seen on the conventional spray arc HLAW weld cross section in Figure 4.5, while neither the bulging nor the crack are found with a pulling buried spray arc.

Another advantage is regarding the filler metal dilution along the weld depth. It has been observed that the filler metal is poorly fed to the laser zone, which remains roughly with the same composition as the base metal (CHEN et al., 2017; CHO et al., 2010; LIU; KUTSUNA; XU, 2006; ZHAO et al., 2009). Stretching the arc zone deep within the weld is expected to have a beneficial effect on filler metal distribution, which should be confirmed in future studies. Many alloys require changing the weld metal composition to avoid problems related to the thermal cycle of the welding process, such as cold cracking, hot cracking, corrosion resistance and so on. The proposed buried spray arc HLAW process might allow welding of alloys that are not LBW or HLAW weldable due to these problems.

The buried spray arc HLAW might also help prevent root humping formation by allowing higher welding speeds for the same laser power and by reducing the effective plate thickness the laser beam must penetrate. This should be further investigated in future works with different welding conditions and without backing.

The process also has good gap bridgeability thanks to its intrinsic high deposition rate and could prove more robust for industrial environment than the conventional HLAW. In the

present application example, the bead showed no humping nor undercutting along its whole length, while the weld performed with a conventional spray arc HLAW process manifested undercuts.

Buried arcs are applicable at narrower gaps than conventional arcs (SCHROEPFER; KROMM; KANNENGIESSER, 2017). For very thick plates, where the HLAW process is used for root pass and subsequent filling passes (usually by GMAW or SAW processes) are needed, using buried spray arc HLAW will allow for narrower joints to be used, reducing the number of filling passes required.

5.3.3 Discontinuities and Difficulties

Humping and undercutting, as expected, are the main concerns regarding the buried spray arc HLAW process at high currents.

With a pulling torch, BCM humping was severe on bead on plate welding at D_{LA} close to the optimum penetration, with the problem being avoided only at distances of **5 mm** or more for **1.5 m/min**, or with welding speed of **1.0 m/min**. Penetration depth decreases considerably at such D_{LA} , but it still seems to be above that for conventional HLAW, so it can still be an interesting option, considering also the other advantages of the buried spray arc HLAW. Reducing the welding speed to **1.0 m/min** is also possible, but it may negatively impact productivity and it should become very sensitive to root humping, so root backing might be necessary.

Considering an industrial application, the joint is another factor that can be manipulated to influence bead quality. It has been shown in the A709 steel application example that an adequate joint can suppress humping and undercutting for the pulling buried spray HLAW at optimal penetration configurations. The influence of the joint configuration should be further studied, as well as the process robustness to malalignment. It is possible that the severe humping might be present if the joint is not adequately prepared and placed.

The pushing buried spray arc HLAW process, on the other hand, showed excellent results regarding humping and undercutting, regardless of the heat sources positioning and welding speed. However, the frontal buildup is detrimental to the penetration depth and can lead to porosity formation and irregularities at the bead sides. If the frontal buildup can be suppressed somehow, possibly with reduced torch angle or with joint preparation, the process with a pushing torch might become interesting to many applications. However, it can still substitute the conventional spray HLAW as it is, due to the seemingly similar or higher penetration, higher wire feed rate and very good bead appearance. Its high bead quality and apparent robustness might even justify it over the pulling buried spray arc HLAW for some applications.

6 CONCLUSIONS AND SUGGESTIONS FOR FUTURE WORKS

6.1 CONCLUSIONS

The buried spray arc HLAW was developed and studied in this work. The first step was preparing the buried spray arc GMAW process for hybridization with LBW. The developed GMAW parameters were then applied in HLAW. Next, the heat sources positioning was optimized regarding penetration depth and the process was compared to conventional spray arc HLAW and to analogue high-current long spray arc HLAW. Finally, the developed process was tested on an application example. From these experiments, the following conclusions can be drawn:

- Stable buried arc GMAW can be obtained with either pushing and pulling torch positions and at welding speeds of **1.0**, **1.5** and **2.0 m/min**, being adequate for hybridization with a laser beam for HLAW.
- As the laser beam is added to the buried spray arc GMAW, the process remains stable without the need to change any welding parameter.
- Very little interaction is observed between the laser beam and the electric arc, with no major changes in average current, voltage and arc length. In the case of a pushing buried arc, however, short-circuiting and kink instability occurrences were reduced with the addition of the laser beam.
- At long laser-arc distances (**5 mm** or more), the laser can completely suppress BCM humping and undercutting formation in pulling buried spray arc HLAW and in pulling high-current long spray arc HLAW. At shorter distances, both discontinuities are reduced but still present. It is believed that the formation of a deep pool under the necking on the trailing region, which allows recirculation of the backward flow, is the phenomenon behind the BCM humping suppression in HLAW.
- The laser beam can effectively suppress GRM humping and split beads at every tested positioning in pulling high-current long spray arc HLAW. Increasing the central bead width and height by adding more heat and by creating a recirculation flow within the deep molten pool might allow the merging of all split beads in one single bead.
- The frontal buildup phenomenon was observed in GMAW and HLAW when a pushing buried arc was used. This frontal buildup is influenced by welding speed and laser-arc distance and it can negatively affect weld penetration, leading to

irregular penetration depths. Only at **5 mm** or above laser-arc distances that the frontal buildup could be suppressed, by allowing the upward-forward flow of metal on the pool front to flow downward through the deep laser induced molten pool.

- Heavy spatter was observed for the pushing high-current spray arc GMAW at every welding speed. Adding the laser to the process reduces the spatter.
- HLAW with a high-current buried spray arc in the pulling position achieve deeper penetration depth than conventional spray HLAW with a confidence of **99.95 %**. It is also highly likely that the increased penetration is not only due to high-current, but also due to the buried arc. There is a **90.93 %** confidence level that welding with a buried arc achieves deeper penetration than welding with equal current and a longer arc in HLAW
- Pulling buried spray arc HLAW on a **9.5 mm** thick Y-joint resulted in reduced laser power requirement, **4.8 kW** against **7.7 kW** for a conventional spray arc.
- A very deep V-shaped arc zone reaching **6.9 mm** depth was observed in pulling buried spray arc HLAW in the Y-joint. The deep arc zone might help against solidification crack, as the necking and bulging regions associated with that discontinuity are overridden by the arc zone. Improved dilution of filler metal along the weld depth should also be expected.

6.2 SUGGESTIONS FOR FUTURE WORKS

The buried spray arc HLAW process showed promising results in the present work, but more research is needed to further understand and develop the process. Some study suggestions for the buried spray arc HLAW are:

- Evaluate the process at different current levels.
- Test different torch inclinations. Frontal buildup and humping could be possibly avoided with reduced inclination.
- Application of different shielding gases should be studied. For instance, spray transfer mode is achievable with cheaper CO₂ shielding gas in buried arcs (BABA et al., 2017; YUAN; YAMAZAKI; SUZUKI, 2016). Other gases might also help reducing humping and undercutting.

- The process should be tested for joining different alloys and its influence on metallurgical properties studied.
- Good results were obtained with the used Y-joint, but other joints configurations should be tested. Process stability to root opening and malalignment should also be evaluated.
- The suspected benefits of reduced solidification flaw, better filler metal dilution and reduced root humping should be further studied.
- Evaluate if BCM and GRM humping are also suppressed with lower laser power, which would allow interesting applications of laser assisted buried spray arc GMAW.
- The voltage oscillation saw in the pushing buried spray arc HLAW should be further studied.
- Different visualization techniques should be applied to validate the hypotheses proposed in this work regarding metal flow, including frontal buildup formation and suppression, GRM humping suppression and BCM humping suppression.

REFERENCES

- ABRAMOCHKIN, E. G.; VOLOSTNIKOV, V. G. Generalized Gaussian beams. **Journal of Optics A: Pure and Applied Optics**, Bristol, v. 6, n. 5, p. S157, 2004.
- ADONYI, Y.; RICHARDSON, R. W.; BAESLACK, W.A.III. Investigation of arc force effects in subsurface GTA welding. **Welding Journal**, Miami, v. 71, n. 9, p. 321, 1992.
- AI, Y. et al. Investigation of the humping formation in the high power and high speed laser welding. **Optics and Lasers in Engineering**, Amsterdam, v. 107, p. 102–111, 2018.
- AKSELSEN, O.; REN, X.; AAS, S. K. Review of laser and hybrid laser-arc welding In: INTERNATIONAL OFFSHORE AND POLAR ENGINEERING CONFERENCE PROCEEDINGS, 24, 2014, Busan. **Proceedings...** Mountain View, California: ISOPE, 2014. p. 278-285.
- ARTINOV, A. et al. Weld pool shape observation in high power laser beam welding. In: CIRP CONFERENCE ON PHOTONIC TECHNOLOGIES, 10, 2018, Fürth. **Proceedings...** Amsterdam: Elsevier Procedia, 2018, v. 74. p. 683-686.
- BABA, H. et al. Single pass full penetration joining for heavy plate steel using high current GMA process. **Welding in the World**, Berlin, p. 1–7, 2017.
- BAGGER, C.; OLSEN, F. O. Review of laser hybrid welding. **Journal of Laser Applications**, Orlando, v. 17, n. 1, p. 2–14, 2005.
- BAKIR, N. et al. Numerical Simulation on the Origin of Solidification Cracking in Laser Welded Thick-Walled Structures. **Metals**, Basel, v. 8, n. 6, p. 406, 2018.
- BARBETTA, L. D. **Solidification flaw and porosity formation in hybrid laser: GMA welding of thick API 5L X70 steel plates**. 2014. Dissertation (Master) - Universidade Federal de Santa Catarina, Florianópolis, 2014.
- BARBIERI, B.; BEVERINI, N.; SASSO, A. Optogalvanic spectroscopy. **Reviews of Modern Physics**, College Park, Maryland, v. 62, n. 3, p. 603–644, 1990.
- BÄUERLE, D. W. **Laser Processing and Chemistry**. 4. ed. Berlin: Springer-Verlag, 2011. 851 p.
- BENGTSSON, P.; SKARIN, D. High speed welding with the A400 HSW robot system and the Rapid Arc and Rapid Melt Processes. **Svetsaren**, Gothenburg, v. 7, n. 2, p. 26–29, 1991.
- BERGER, P. et al. Zur Bedeutung von gleitenden Stufen an der Kapillarfront beim Schweißen und Schneiden mit Laserstrahlen—Teil 2. **Schweißen und Schneiden**, Essen, v. 63, n. 3, p. 100, 2011.
- BRADSTREET, B. Effect of Surface Tension and Metal Flow on Weld Bead Formation. **Welding Journal**, Miami, v. 47, n. 7, p. 314s-322s, 1968.
- BUDIG, B. **EWM-ForceArc: A powerful tool for MIG/MAG welding**. Mündersbach: EWM, 2005.

BUNAZIV, I. et al. Hybrid Welding Possibilities of Thick Sections for Arctic Applications. In: NORDIC LASER MATERIALS PROCESSING CONFERENCE, 15, 2015, Lappeenranta. **Proceedings...** Lappeenranta: Lappeenranta-Lahti University of Technology, 2015, v. 78. p. 74-83.

BUNAZIV, I. et al. Process stability during fiber laser-arc hybrid welding of thick steel plates. **Optics and Lasers in Engineering**, Amsterdam, v. 102, p. 34–44, 2018. a.

BUNAZIV, I. et al. The penetration efficiency of thick plate laser-arc hybrid welding. **The International Journal of Advanced Manufacturing Technology**, London, v. 97, n. 5–8, p. 2907–2919, 2018. b.

CAI, C. et al. Influence of laser on the droplet behavior in short-circuiting, globular, and spray modes of hybrid fiber laser-MIG welding. **Optics & Laser Technology**, Amsterdam, v. 83, p. 108-118, 2016.

CAI, M.; WU, C.; GAO, X. Research on Humping Tendency in High Speed Laser Welding of SUS304 Austenitic Stainless Steel. In: INTERNATIONAL CONFERENCE ON MATERIAL SCIENCE, ENERGY AND ENVIRONMENTAL ENGINEERING, 2017, Xi'an. **Proceedings...** Amsterdam: Atlantis, 2017, v. 125, p. 402-409.

CAMPANA, G. et al. The influence of arc transfer mode in hybrid laser-mig welding. **Journal of Materials Processing Technology**, Amsterdam, v. 191, n. 1, p. 111-113, 2007.

CAO, X. et al. Hybrid fiber laser – Arc welding of thick section high strength low alloy steel. **Materials & Design**, Amsterdam, v. 32, n. 6, p. 3399–3413, 2011.

CHEN, J. et al. Predicting the influence of groove angle on heat transfer and fluid flow for new gas metal arc welding processes. **International Journal of Heat and Mass Transfer**, Amsterdam, v. 55, p. 102-111, 2011.

CHEN, J.; WU, C. S. Numerical simulation of humping phenomenon in high speed gas metal arc welding. **Frontiers of Materials Science**, Berlin, v. 5, n. 2, p. 90–97, 2011.

CHEN, M. et al. Effect of laser pulse on alternative current arc discharge during laser-arc hybrid welding of magnesium alloy. **Optics and Lasers in Engineering**, Amsterdam, v. 100, p. 208–215, 2018.

CHEN, R. et al. Effect of magnetic field applied during laser-arc hybrid welding in improving the pitting resistance of the welded zone in austenitic stainless steel. **Corrosion Science**, Amsterdam, v. 126, p. 385–391, 2017.

CHEN, Y. B. et al. Experimental study on welding characteristics of CO2 laser TIG hybrid welding process. **Science and Technology of Welding and Joining**, Abingdon-on-Thames, v. 11, n. 4, p. 403–411, 2006.

CHO, M. H.; FARSON, D. F. Understanding Bead Hump Formation in Gas Metal Arc Welding Using a Numerical Simulation. **Metallurgical and Materials Transactions B**, New York, v. 38, n. 2, p. 305–319, 2007.

CHO, W. et al. Numerical study of alloying element distribution in CO₂ laser–GMA hybrid welding. **Computational Materials Science**, Amsterdam, v. 49, n. 4, p. 792–800, 2010.

CHOI, H. W.; FARSON, D. F.; CHO, M. H. Using a hybrid laser plus GMAW process for controlling the bead humping defect. **Welding Journal**, Miami, v. 85, n. 8, p. 174–179, 2006.

CLERICI, M. et al. Laser-assisted guiding of electric discharges around objects. **Science Advances**, Washington, DC, v. 1, n. 5, p. e1400111, 2015.

CRAMER, H.; BAUM, L.; POMMER, S. Überblick zu modernen lichtbogenprozessen und deren werkstoffübergängen beim MSG-schweißen. **DVS-Berichte**, Düsseldorf, v. 275., p. 232–237, 2011.

DELONE, N. B. **Basics of Interaction of Laser Radiation with Matter**. Gif-sur-Yvette: Frontières, 1993.

DILTHEY, U.; WIESCHEMANN, A. Prospects by combining and coupling laser beam and arc welding processes. **Welding in the World**, Berlin, v. 44, n. 3, p. 37–46, 2000.

DOMPABLO, M. New solutions in coldArc and forceArc welding technology. **Welding International**, Abingdon-on-Thames, v. 27, n. 1, p. 24–29, 2013.

DOWDEN, J.; SCHULZ, W.. **The Theory of Laser Materials Processing: Heat and Mass Transfer in Modern Technology**. 2. ed. Cham: Springer International Publishing, 2017. 432 p.

DVS. **Übersicht der Prozessregelvarianten des MSG-Schweißen**. Düsseldorf: Deutscher Verband für Schweißen und verwandte Verfahren, 2015. 1p.

DVS. **Laserstrahl-Lichtbogen-Hybridschweißverfahren**. Düsseldorf: Deutscher Verband für Schweißen und verwandte Verfahren e.V. 2005, 1 p. (3216)

EINSTEIN, A. Strahlungs-emission und -absorption nach der Quantentheorie. **Verhandlungen der Deutschen Physikalischen Gesellschaft**, Bad Honeff, v. 18, p. 318–323, 1916.

EL RAYES, M.; WALZ, C.; SEPOLD, G. The influence of various hybrid welding parameters on bead geometry. **Welding Journal**, Miami, v. 83, p. 147- S, 2004.

EMDE, B. et al. Influence of Welding Current and Focal Position on the Resonant Absorption of Laser Radiation in a TIG Welding Arc. In: INTERNATIONAL CONFERENCE ON LASER ASSISTED NET SHAPE ENGINEERING, 8, 2014, Fürth. **Proceedings...** Amsterdam: Elsevier Procedia, 2014, v. 56, p. 646-652.

EMDE, B. et al. Significance of the Resonance Condition for Controlling the Seam Position in Laser-assisted TIG Welding. In: CONFERENCE ON PHOTONIC TECHNOLOGIES, 9, 2016, Fürth. **Proceedings...** Amsterdam: Elsevier Procedia, 2016, v. 83, p. 568-576, 2016.

ERIKSSON, I.; POWELL, J.; KAPLAN, A. Guidelines in the Choice of Parameters for Hybrid Laser Arc Welding with Fiber Lasers. In: LASERS IN MANUFACTURING, 3, 2013, Munich. **Proceedings...** Amsterdam: Elsevier Procedia, 2014, v. 41, p. 119-127.

ERIKSSON, I.; POWELL, J.; KAPLAN, A. F. H. Measurements of fluid flow on keyhole front during laser welding. **Science and Technology of Welding and Joining**, Abingdon-on-Thames, v. 16, n. 7, p. 636–641, 2011.

FABBRO, R. Melt Pool and Keyhole Behavior Analysis for Deep Penetration Laser Welding. **Journal of Physics D: Applied Physics**, Bristol, v. 43, n. 44, p. 445501, 2010.

FAN, D.; USHIO, M.; MATSUDA, F. Numerical Computation of Arc Pressure Distribution (Welding Physics, Process & Instrument). **Transactions of JWRI**, Osaka, v. 15, n. 1, p. 1–5, 1986.

FAN, H. G.; SHI, Y. W. Numerical simulation of the arc pressure in gas tungsten arc welding. **Journal of Materials Processing Technology**, Amsterdam, v. 61, n. 3, p. 302–308, 1996.

FELLMAN, A.; SALMINEN, A. Study of the phenomena of fiber laser-MAG hybrid welding. In: INTERNATIONAL CONGRESS ON APPLICATIONS OF LASERS AND ELECTRO-OPTICS, 26, 2007, Orlando. **Proceedings...** Orlando: Laser Institute of America, 2007, p. 871–880.

FRITSCHÉ, H. et al. Direct diode lasers and their advantages for materials processing and other applications. In: HIGH-POWER LASER MATERIALS PROCESSING: LASERS, BEAM DELIVERY, DIAGNOSTICS AND APPLICATIONS, 4, 2015, San Francisco. **Proceedings...** Bellingham: SPIE, 2015, v. 9356, p. 935601.

FROSTEVARG, J. Comparison of three different arc modes for laser-arc hybrid welding steel. **Journal of Laser Applications**, Orlando, v. 28, n. 2, p. 022407, 2016.

FROSTEVARG, J. Factors affecting weld root morphology in laser keyhole welding. **Optics and lasers in engineering**, Amsterdam, v. 101, p. 89–98, 2018.

GAO, M. et al. Weld microstructure and shape of laser–arc hybrid welding. **Science and Technology of Welding and Joining**, Abingdon-on-Thames, v. 13, n. 2, p. 106–113, 2008.

GATZEN, M.; TANG, Z.; VOLLERTSEN, F. Effect of electromagnetic Stirring on the Element Distribution in Laser Beam Welding of Aluminium with Filler Wire. In: LASERS IN MANUFACTURING, 2, 2011, Munich. **Proceedings...** Amsterdam: Elsevier Procedia, 2011, v.12, p.56-65.

GEBHARDT, M. O.; GUMENYUK, A.; RETHMEIER, M. Solidification cracking in laser GMA hybrid welding of thick-walled parts. **Science and Technology of Welding and Joining**, Abingdon-on-Thames, v. 19, n. 3, p. 209–213, 2014.

GONDIM, A. et al. **Avaliação dos efeitos da indutância e da corrente pulsada no processo MIG buried arc**. Florianópolis: Universidade Federal de Santa Catarina, 2016.

GONG, M. et al. Stabilization effect of space constraint in narrow gap laser-arc hybrid welding analyzed by approximate entropy. **The International Journal of Advanced Manufacturing Technology**, London, v. 92, n. 9–12, p. 3093–3102, 2017.

GOOK, S.; GUMENYUK, A.; RETHMEIER, M. Hybrid laser arc welding of X80 and X120 steel grade. **Science and Technology of Welding and Joining**, Abingdon-on-Thames, v. 19, n. 1, p. 15–24, 2014.

GRATZKE, U. et al. Theoretical approach to the humping phenomenon in welding processes. **Journal of Physics D: Applied Physics**, Bristol, v. 25, n. 11, p. 1640–1647, 1992.

GRESES, J. et al. Plume attenuation under high power Nd:yttrium–aluminum–garnet laser welding. **Journal of Laser Applications**, Orlando, v. 16, n. 1, p. 9–15, 2004.

HAM, H. S.; OH, D. S.; CHO, Sang-Myung. Measurement of arc pressure and shield gas pressure effect on surface of molten pool in TIG welding. **Science and Technology of Welding and Joining**, Abingdon-on-Thames, v. 17, p. 594–600, 2012.

HANN, D. B.; IAMMI, J.; FOLKES, J. A simple methodology for predicting laser-weld properties from material and laser parameters. **Journal of Physics D: Applied Physics**, Bristol, v. 44, n. 44, p. 445401, 2011.

HAUG, P. et al. Influence of Laser Wavelength on Melt Bath Dynamics and Resulting Seam Quality at Welding of Thick Plates. In: **LASERS IN MANUFACTURING**, 3, 2013, Munich. **Proceedings...** Amsterdam: Elsevier Procedia, 2014, v.41, p. 49-58.

HEINZE, C. et al. Microcrack Formation During Gas Metal Arc Welding of High-Strength Fine-Grained Structural Steel. **Acta Metallurgica Sinica (English Letters)**, Beijing, v. 27, n. 1, p. 140–148, 2014.

HIRANO, K.; FABBRO, R.; MULLER, M. Experimental determination of temperature threshold for melt surface deformation during laser interaction on iron at atmospheric pressure. **Journal of Physics D: Applied Physics**, Bristol, v. 44, n. 43, p. 435402, 2011.

HOFFMAN, J.; SZYMANSKI, Z. Absorption of the laser beam during welding with CO₂ laser. **Optica Applicata**, Wrocław, v. 32, p. 129–145, 2002.

HU, B.; OUDEN, G. Den. Laser induced stabilisation of the welding arc. **Science and Technology of Welding and Joining**, Abingdon-on-Thames v. 10, n. 1, p. 76–81, 2005. a.

HU, B.; OUDEN, G. Den. Synergetic effects of hybrid laser/arc welding. **Science and Technology of Welding and Joining**, Abingdon-on-Thames, v. 10, n. 4, p. 427–431, 2005. b.

HU, J.; TSAI, H. L. Heat and mass transfer in gas metal arc welding. Part I: The arc. **International Journal of Heat and Mass Transfer**, Amsterdam, v. 50, p. 833–846, 2007.

ILAR, T. et al. Root Humping in Laser Welding – an Investigation based on High Speed Imaging. In: **INTERNATIONAL CONFERENCE & EXHIBITION ON PHOTONIC TECHNOLOGIES**, 7, 2012, Fürth. **Proceedings...** Amsterdam: Elsevier Procedia, 2012, v.39, p. 27-32.

IIW. **Classification of Metal Transfer**. Villepinte: International Institute of Welding, 1976. (IIW DOC XII-636-76).

ION, J. C.; SHERCLIFF, H. R.; ASHBY, M. F. Diagrams for laser materials processing. **Acta Metallurgica et Materialia**, [s. l.], v. 40, n. 7, p. 1539–1551, 1992.

ISHIDE, T.; TSUBOTA, S.; WATANABE, M. Latest MIG, TIG arc-YAG laser hybrid welding systems for various welding products. In: INTERNATIONAL SYMPOSIUM ON HIGH-POWER LASER MACROPROCESSING, 1, 2003, Osaka. **Proceedings...** Bellingham: SPIE, 2003, v. 4831, p. 347-352.

INTERNATIONAL ORGANIZATION FOR STANDARDIZATION. **ISO 15614-11:2002**. Specification and qualification of welding procedures for metallic materials — Welding procedure test — Part 11: Electron and laser beam welding. Geneva, 2002. 23 p.

JAESCHKE, B.; VOLLRATH, K. Speed Pulse - Eine Produktivitäts- und Effizienzsteigernde Weiterentwicklung des MSG-Impulsschweißens. **Schweissen und Schneiden**, Essen, v. 61, n. 9, p. 548–553, 2009.

JARVIS, B. **Keyhole gas tungsten arc welding: a new process variant**. 2001. 288 p. Thesis (Doctor of Philosophy) - University of Wollongong, Wollongong.

JORDAN, E. C.; BALMAIN, Keith George. **Electromagnetic waves and radiating systems**. 2. ed. Englewood Cliffs, N.J.: Prentice-Hall, 1968. 753 p.

KAH, P. Overview of the exploration status of laser-arc hybrid welding processes. **Reviews on Advanced Materials Science**, Moscow, v. 30, p. 112–132, 2012.

KATAYAMA, S. et al. Physical phenomena and porosity prevention mechanism in laser-arc hybrid welding. **Transactions of JWRI**, Osaka, v. 35, n. 1, p. 13–18, 2006.

KATAYAMA, S.; KAWAHITO, Y.; MIZUTANI, M. Elucidation of laser welding phenomena and factors affecting weld penetration and welding defects. In: INTERNATIONAL CONFERENCE ON PHOTONIC TECHNOLOGIES, 6, 2010, Fürth. **Proceedings...** Amsterdam: Elsevier Procedia, 2010, v. 5 (Part 2), p. 9-17.

KAWAHITO, Y. et al. Effect of weakly ionised plasma on penetration of stainless steel weld produced with ultra high power density fibre laser. **Science and Technology of Welding and Joining**, Abingdon-on-Thames, v. 13, n. 8, p. 749–753, 2008.

KESSLER, B. **Welding Results, 2006-2008**. Burbach: IPG-Photonics Marketing Materials, 2008.

KIM, J.; KI, H. Scaling law for penetration depth in laser welding. **Journal of Materials Processing Technology**, Amsterdam, v. 214, n. 12, p. 2908–2914, 2014.

KOZAKOV, R. et al. Change of electrical conductivity of Ar welding arc under resonant absorption of laser radiation. **Journal of Physics D: Applied Physics**, Bristol, v. 48, n. 9, p. 095502, 2015.

KUTSUNA, M.; CHEN, L. Interaction of both plasmas in CO₂ laser-MAG hybrid welding of carbon steel. In: INTERNATIONAL SYMPOSIUM ON HIGH-POWER LASER MACROPROCESSING, 1, 2003, Osaka. **Proceedings...** Bellingham: SPIE, 2003, v. 4831, p. 341-346.

- LANCASTER, J. F. **The Physics of Welding**. 2. ed. Oxford: Pergamon, 1984. 340 p.
- LE GUEN, E. et al. Analysis of hybrid Nd:Yag laser-MAG arc welding processes. **Optics & Laser Technology**, Amsterdam, v. 43, n. 7, p. 1155–1166, 2011.
- LEE, M. et al. Laser - mig hybrid weldability of high strength steel for car industry. In: INTERNATIONAL CONGRESS ON APPLICATIONS OF LASERS AND ELECTRO-OPTICS, 24, 2005, Miami. **Proceedings...** Orlando: Laser Institute of America, 2005, v. 98, p. 134-142.
- LEI, Z. et al. Numerical simulation of droplet shapes in laser-MIG hybrid welding. **Optics & Laser Technology**, Amsterdam, v. 88, p. 1–10, 2017.
- LESNEWICH, A. Control of Melting Rate and Metal Transfer in Gas Shielded Metal Arc Welding. **Welding Journal**, Miami, v. 37, p. 343s-353s, 1958.
- LIENERT, T. J. et al. **Welding Fundamentals and Processes**. 1 ed. Russell Township, Ohio: ASM International, 2011. 891 p. v. 06A.
- LIENHARD, J. H. IV; LIENHARD, J. H. V. **A heat transfer textbook**. 4. ed. Mineola, N.Y: Dover, 2011. 757 p.
- LIN, M. L.; EAGAR, T. W. Pressures produced by gas tungsten arcs. **Metallurgical Transactions B**, Berlin, v. 17, n. 3, p. 601–607, 1986.
- LIU, L.; CHEN, M. Interactions between laser and arc plasma during laser–arc hybrid welding of magnesium alloy. **Optics and Lasers in Engineering**, Amsterdam, v. 49, n. 9, p. 1224–1231, 2011.
- LIU, L.; HAO, X. Study of the effect of low-power pulse laser on arc plasma and magnesium alloy target in hybrid welding by spectral diagnosis technique. **Journal of Physics D: Applied Physics**, Bristol, v. 41, n. 20, p. 205202, 2008.
- LIU, S.; SIEWERT, T. A. Metal transfer in gas metal arc welding: droplet rate. **Welding Journal**, Miami, v. 68, n. 2, p. 52–58, 1989.
- LIU, S. et al. Analysis of droplet transfer mode and forming process of weld bead in CO2 laser–MAG hybrid welding process. **Optics & Laser Technology**, Amsterdam, v. 44, n. 4, p. 1019–1025, 2012.
- LIU, Z.; KUTSUNA, M.; XU, G. Microstructure and Mechanical Properties of CO2 Laser-MAG Hybrid Weld of High Strength Steel. **Quarterly Journal of the Japan Welding Society**, Tokyo, v. 24, n. 4, p. 344–349, 2006.
- LORCH. **Lorch SpeedArc and SpeedArc XT**. Auenwald: Lorch, 2019, 2p. Fact Sheet.
- MAHRLE, A.; BEYER, E. Hybrid laser beam welding—Classification, characteristics, and applications. **Journal of Laser Applications**, Orlando, v. 18, n. 3, p. 169–180, 2006.
- MAIMAN, T. H. Stimulated Optical Radiation in Ruby. **Nature**, London, v. 187, n. 4736, p. 493–494, 1960.

MASHIKO, Y. et al. 2 kW single-mode fiber laser with 20-m long delivery fiber and high SRS suppression. In: FIBER LASERS XIII: TECHNOLOGY, SYSTEMS AND APPLICATIONS, 2016, San Francisco. **Proceedings...** Bellingham: SPIE, 2016, v. 9728, p. 972805.

MATSUDA, J. et al. TIG or MIG arc augmented laser welding of thick mild steel plate. **Joining and Materials**, Great Abington, Cambridgeshire, v. 1, p. 31–34, 1988.

MATSUNAWA, A. et al. Porosity formation mechanism and its prevention in laser welding. **Welding International**, Abingdon-on-Thames, v. 17, n. 6, p. 431–437, 2003.

MATSUNAWA, A. Science of laser welding - Mechanisms of keyhole and pool dynamics. In: INTERNATIONAL CONGRESS ON APPLICATIONS OF LASERS AND ELECTRO-OPTICS, 21, 2002, Scottsdale. **Proceedings...** Orlando: Laser Institute of America, 2002, p. 290.

MATUSIAK, J.; PFEIFER, T. Alternative methods of productivity increasing at MAG welding process of unalloyed steels. **Hutnik, Wiadomości Hutnicze**, warshaw, v. 75, n. 3, p. 110–115, 2008.

MENDEZ, P. F.; EAGAR, T. W. In: MATHEMATICAL MODELLING OF WELD PHENOMENA. **Estimation of the characteristic properties of the weld pool during high productivity arc welding**. London, 2000, v. 5, 28 p.

MENDEZ, P. F.; EAGAR, T. W. Penetration and defect formation in high-current arc welding. **Welding Journal**, Miami, v. 82, n. 10, p. 296, 2003.

MENDEZ, P.; GÖTT, G.; D GUEST, S. High Speed Video of Metal Transfer in Submerged Arc Welding. **Welding journal**, Miami, v. 94, 2015.

MENG, X. et al. Numerical analysis of undercut defect mechanism in high speed gas tungsten arc welding. **Journal of Materials Processing Technology**, Amsterdam, v. 236, p. 225–234, 2016.

MENG, X.; QIN, G. A theoretical study of molten pool behavior and humping formation in full penetration high-speed gas tungsten arc welding. **International Journal of Heat and Mass Transfer**, Amsterdam, v. 132, p. 143–153, 2019.

MENG, X.; QIN, G.; ZOU, Z. Investigation of humping defect in high speed gas tungsten arc welding by numerical modelling. **Materials & Design**, Amsterdam, v. 94, p. 69–78, 2016.

MONTGOMERY, D. C. **Design and analysis of experiments**. 8. ed. Hoboken: John Wiley & Sons, Inc, 2013. 724 p.

MULDERS, M. A. In: DEVELOPMENTS IN SOIL SCIENCE. **Interaction of Electromagnetic Radiation with Matter**. Amsterdam: Elsevier, 1987. v. 15 p. 12–54.

MURAKAMI, T.; SHIN, M.; NAKATA, K. Effect of welding direction on weld bead formation in high power fiber laser and MAG arc hybrid welding. **Transactions of JWRI**, Osaka, v. 39, n. 2, p. 175–177, 2010.

MVOLA BELINGA, E. M. **Applications and Benefits of Adaptive Pulsed GMAW**. 2012. 124 p. Thesis (Master). Faculty of Technology, Lappeenranta University of Technology, Lappeenranta.

NAITO, Y.; KATAYAMA, S.; MATSUNAWA, A. Keyhole behavior and liquid flow in molten pool during laser-arc hybrid welding. In: INTERNATIONAL SYMPOSIUM ON HIGH-POWER LASER MACROPROCESSING, 1, 2003, Osaka. **Proceedings...** Bellingham: SPIE, 2003, v. 4831, p. 357-362.

NILSSON, K. et al. Parameter Influence in CO₂-laser/MIG Hybrid Welding. In: ANNUAL ASSEMBLY OF INTERNATIONAL INSTITUTE OF WELDING, 56, 2003, Bucharest. **Proceedings...** Villepinte: International Institute of Welding, 2003, v.56, 11 p.

NORRISH, J. **Advanced Welding Processes: Technologies and Process Control**. Cambridge: Woodhead, 2006. 304 p.

OHNISHI, T. et al. Butt welding of thick, high strength steel plate with a high power laser and hot wire to improve tolerance to gap variance and control weld metal oxygen content. **Science and Technology of Welding and Joining**, Abingdon-on-Thames, v. 18, n. 4, p. 314–322, 2013.

OLIVARES, E. A. G. et al. Study of the Tig Keyhole Technique Through Comparative Analysis Between Two High Productivity Torches in Joints of the Middle Thickness Carbon Steel Plates. **Soldagem & Inspeção**, Moema, v. 20, n. 3, p. 262–274, 2015.

OLSEN, F. O. **Hybrid Laser-Arc Welding**. 1. ed. Cambridge: Woodhead, 2009. 323 p.

ONO, M. et al. Development of Laser-arc Hybrid Welding. **NKK Technical Review**. Fukuyama, v. 86, p. 8-12, 2002.

ONO, M. et al. Welding properties of thin steel sheets by laser-arc hybrid welding: laser-focused arc welding. In: INTERNATIONAL SYMPOSIUM ON HIGH-POWER LASER MACROPROCESSING, 1, 2003, Osaka. **Proceedings...** Bellingham: SPIE, 2003, v. 4831, p. 369-374.

PAN, Q. et al. Effect of shielding gas on laser–MAG arc hybrid welding results of thick high-tensile-strength steel plates. **Welding in the World**, Berlin, v. 60, n. 4, p. 653–664, 2016. a.

PASCHOTTA, R. **RP Photonics Encyclopedia: Beam Parameter Product**. Bad Dürkheim: RP Photonics Consulting, [s. d.]. Available at: <https://www.rp-photonics.com/beam_parameter_product.html>. Accessed in: 25 mar. 2018.

PENNING, F. M. **Physica**, Amsterdam, v. 8, p. 137, 1928.

PETRING, D.; FUHRMANN, C. Recent progress and innovative solutions for laser-arc hybrid welding. In: PACIFIC INTERNATIONAL CONFERENCE ON APPLICATIONS OF LASERS AND OPTICS, 1, 2004, Melbourne. **Proceedings...** Orlando: Laser Institute of America, 2004, v.1, p. 7-10.

PETRING, D. et al. Progress in laser-MAG hybrid welding of high-strength steels up to 30 mm thickness. In: INTERNATIONAL CONGRESS ON APPLICATIONS OF LASERS AND ELECTRO-OPTICS, 26, 2007, Orlando. **Proceedings...** Orlando: Laser Institute of America, 2007, p. 300-307.

POPRAWA, Reinhart. **Tailored Light 2: Laser Application Technology**. 1. ed. Berlin: Springer, 2011. 605 p.

PORT, P. Le et al. K-GTAW process: A new welding technology combining quality and productivity. **Welding International**, Abingdon-on-Thames, v. 21, n. 6, p. 430–441, 2007.

POWELL, J. et al. Weld root instabilities in fiber laser welding. **Journal of Laser Applications**, Orlando, v. 27, n. S2, p. S29008, 2015.

QUINTINO, L.; ASSUNÇÃO, E. In: HANDBOOK OF LASER WELDING TECHNOLOGIES. **Conduction laser welding**. Cambridge: Woodhead. 2013. p. 139-162.

RAI, R. et al. Heat transfer and fluid flow during keyhole mode laser welding of tantalum, Ti-6Al-4V, 304L stainless steel and vanadium. **Journal of Physics D: Applied Physics**, Bristol, v. 40, n. 18, p. 5753, 2007.

RAI, R. et al. A Convective Heat-Transfer Model for Partial and Full Penetration Keyhole Mode Laser Welding of a Structural Steel. **Metallurgical and Materials Transactions A**, New York, v. 39, n. 1, p. 98–112, 2008.

RASBAND, W. **ImageJ**. Bethesda, EUA: National Institute of Mental Health, [s.d.].

REISGEN, Uwe et al. Laser Beam Submerged Arc Hybrid Welding. In: INTERNATIONAL CONFERENCE & EXHIBITION ON PHOTONIC TECHNOLOGIES, 7, 2012, Fürth. **Proceedings...** Amsterdam: Elsevier Procedia, 2012, v.39, p. 75-83.

RHEE, S.; KANNATEY-ASIBU JR., E. Observation of Metal Transfer During Gas Metal Arc Welding. **Welding Journal**, Miami, v. 23, p. 381s-386s, 1992.

RIBIC, B.; BURGARDT, P.; DEBROY, T. Optical emission spectroscopy of metal vapor dominated laser-arc hybrid welding plasma. **Journal of Applied Physics**, College Park, Maryland, v. 109, n. 8, p. 083301, 2011.

RIBIC, B.; PALMER, T. A.; DEBROY, T. Problems and issues in laser-arc hybrid welding. **International Materials Reviews**, Abingdon-on-Thames, v. 54, n. 4, p. 223–244, 2009.

RIBIC, B.; RAI, R.; DEBROY, T. Numerical simulation of heat transfer and fluid flow in GTA/Laser hybrid welding. **Science and Technology of Welding and Joining**, Abingdon-on-Thames, v. 13, n. 8, p. 683–693, 2008.

ROHSENOW, W. M.; HARTNETT, J. P.; CHO, Y. I. (EDS.). **Handbook of heat transfer**. 3. ed. New York: McGraw-Hill, 1998. 1344 p.

ROKHLIN, S.; GUU, A. C. A study of arc force, pool depression and weld penetration during gas tungsten arc welding. **Welding Journal**, Miami, v. 72, n. 8, p. 381s-390s, 1993.

ROMINGER, V. et al. Prozessuntersuchungen beim Laserstrahl-tiefschweißen - Festkörperlaser hoher Brillanz im Vergleich zu CO₂-Lasern. In: DVS CONGRESS, 2010, Nuremberg. **Proceedings...** Düsseldorf: Deutscher Verband für Schweißen und verwandte Verfahren, v. 267, 2010, p. 188-193.

SALMINEN, A.; PIILI, H.; PURTONEN, T. The characteristics of high power fibre laser welding. **Proceedings of the Institution of Mechanical Engineers, Part C: Journal of Mechanical Engineering Science**, Thousand Oaks, California, v. 224, n. 5, p. 1019–1029, 2010.

SAVAGE, W. F.; NIPPES, E. F.; AGUSA, K. Effect of arc force on defect formation in GTA welding. **Welding journal**, Miami, v. 58, n. 7, p. 212, 1979.

ŠČEGLOV, P. **Study of vapour-plasma plume during high power fiber laser beam influence on metals**. 2012. 109 p. Dissertation (Doctor of Philosophy) - Faculty of Experimental and Theoretical Physics, National Research Nuclear University, Moscow.

SCHAUPP, T.; RHODE, M.; KANNENGIESSER, T. Influence of welding parameters on diffusible hydrogen content in high-strength steel welds using modified spray arc process. **Welding in the World**, Berlin, v. 62, n. 1, p. 9–18, 2018.

SCHROEPFER, D.; KROMM, A.; KANNENGIESSER, T.. Optimization of welding loads with narrow groove and application of modified spray arc process. **Welding in the World**, Berlin, v. 61, n. 6, p. 1077–1087, 2017.

SCOTTI, A. Mapping transfer modes for stainless steel gas metal arc welding. **Science and Technology of Welding and Joining**, Abingdon-on-Thames, v. 5, p. 227–234, 2000.

SCOTTI, A.; RODRIGUES, C. E. A. L. Determination of the momentum of droplets impinging on the pool during aluminium GMAW. **Soldagem & Inspeção**, Moema, v. 14, n. 4, p. 336–343, 2009.

SEYFFARTH, P.; KRIVTSUN, I. **Laser-Arc Processes and Their Applications in Welding and Material Treatment**. 1. ed. Boca Raton, Florida: CRC, 2002. v. 1. 200 p.

SHINN, B. W.; FARSON, D. F.; DENNEY, P. E. Laser stabilisation of arc cathode spots in titanium welding. **Science and Technology of Welding and Joining**, Abingdon-on-Thames, v. 10, n. 4, p. 475–481, 2005.

SODERSTROM, E.; MENDEZ, P. Humping mechanisms present in high speed welding. **Science and Technology of Welding and Joining**, Abingdon-on-Thames, v. 11, n. 5, p. 572–579, 2006.

SPROESSER, G. et al. Life Cycle Assessment of welding technologies for thick metal plate welds. **Journal of Cleaner Production**, Amsterdam, v. 108, p. 46–53, 2015.

STARTSEV, V. N.; MARTYNENKO, D. P.; LEONOV, A. F. Investigation of characteristics of an arc column in laser arc welding using numerical simulation. **High Temperature**, Road Town, British Virgin Islands, v. 38, n. 1, p. 20–25, 2000.

STEEL MARKET DEVELOPMENT INSTITUTE. **Guide Specification for Highway Bridge Fabrication with High Performance Steel**. 3. ed. Washington: Steel Market Development Institute, 2011. 22 p.

STEEN, W. M. Arc augmented laser processing of materials. **Journal of Applied Physics**, College Park, Maryland, v. 51, n. 11, p. 5636–5641, 1980.

STEEN, W. M.; EBOO, M. Arc augmented laser welding. **Metal Construction**, Great Abington, Cambridgeshire, v. 21, n. 7, p. 332–335, 1979.

STEEN, W. M.; MAZUMDER, J. **Laser Material Processing**. 4. ed. London: Springer, 2010. 558 p.

STOL, I.; WILLIAMS, K. L.; GAYDOS, D. W. Back to Basics: Using a Buried Gas Metal Arc for Seam Welds. **Welding Journal**, Miami, v. 85, n. 4, p. 28–36, 2006.

STUTE, U.; KLING, R.; HERMSDORF, J. Interaction between Electrical Arc and Nd: YAG Laser Radiation. **CIRP Annals**, Paris, v. 56, n. 1, p. 197–200, 2007.

SUDER, W. J.; WILLIAMS, S. Power factor model for selection of welding parameters in CW laser welding. **Optics & Laser Technology**, Amsterdam, v. 56, p. 223–229, 2014.

SUDER, W. J.; WILLIAMS, S. W. Investigation of the effects of basic laser material interaction parameters in laser welding. **Journal of Laser Applications**, Orlando, v. 24, n. 3, p. 032009, 2012.

SUDER, W. J. et al. Root stability in hybrid laser welding. **Journal of Laser Applications**, Orlando, v. 29, n. 2, p. 022410, 2017.

SUGINO, T. et al. Fundamental study on welding phenomena in pulsed laser-gma hybrid welding. In: INTERNATIONAL CONGRESS ON APPLICATIONS OF LASERS AND ELECTRO-OPTICS, 24, 2005, Miami. **Proceedings...** Orlando: Laser Institute of America, 2005, v. 98, p. 108-116.

THE LINCOLN ELECTRIC COMPANY. **RapidArc™ — High Speed GMAW Welding**. Cleveland: The Lincoln Electric Company, 2005. 6 p.

UCHIUMI, S. et al. Penetration and welding phenomena in YAG laser-mig hybrid welding of aluminum alloy. In: INTERNATIONAL CONGRESS ON APPLICATIONS OF LASERS AND ELECTRO-OPTICS, 23, 2004, San Francisco. **Proceedings...** Orlando: Laser Institute of America, 2004, v. 98, p. P530.

VOLLERTSEN, F.; THOMY, C. Magnetic stirring during laser welding of aluminum. **Journal of Laser Applications**, Orlando, v. 18, n. 1, p. 28–34, 2006.

WAHBA, M.; MIZUTANI, M.; KATAYAMA, S. Hybrid welding with fiber laser and CO2 gas shielded arc. **Journal of Materials Processing Technology**, Amsterdam, v. 221, p. 146–153, 2015.

- WANG, Lei et al. Stabilization mechanism and weld morphological features of fiber laser-arc hybrid welding of pure copper. **Journal of Manufacturing Processes**, Southfield, Michigan, v. 27, p. 207–213, 2017.
- WANG, Y.; TSAI, H. Impingement of filler droplets and weld pool dynamics during gas metal arc welding process. **International Journal of Heat and Mass Transfer**, Amsterdam, v. 44, n. 11, p. 2067–2080, 2001.
- WANG, Yi et al. Generalised Hermite-Gaussian beams and mode transformations. **Journal of Optics**, Bristol, v. 18, n. 5, p. 055001, 2016.
- WEI, P. S. Thermal Science of Weld Bead Defects: A Review. **Journal of Heat Transfer**, New York, v. 133, n. 3, p. 031005, 2010.
- WEMAN, K.; LINDEN, G. **MIG Welding Guide**. 1. ed. Cambridge: Woodhead, 2006. 303 p.
- YAMAMOTO, T.; SHIMADA, W. A study on bead formation in high speed TIG arc welding at low gas pressure. In: INTERNATIONAL SYMPOSIUM OF THE JAPAN WELDING SOCIETY ON ADVANCED WELDING TECHNOLOGY, 2, 1975, Osaka. **Proceedings...** Tokyo: Japan Welding Society, 1975, v. 2, 7 p.
- YANG, M. et al. Arc force and shapes with high-frequency pulsed-arc welding. **Science and Technology of Welding and Joining**, Abingdon-on-Thames, v. 22, n. 7, p. 580–586, 2017.
- YASUI, K. Efficient and stable operation of a high-brightness cw 500-W Nd:YAG rod laser. **Applied Optics**, Bristol, v. 35, n. 15, p. 2566–2569, 1996.
- YOUSUKE, K. et al. Visualization of interaction between laser beam and YAG-laser-induced plume. In: INTERNATIONAL CONGRESS ON APPLICATIONS OF LASERS AND ELECTRO-OPTICS, 24, 2005, San Francisco. **Proceedings...** Orlando: Laser Institute of America, 2005, v. 98, p. P530.
- YUAN, Y.; YAMAZAKI, K.; SUZUKI, R. Relationship between penetration and porosity in horizontal fillet welding by a new process “hybrid tandem MAG welding process”. **Welding in the World**, Berlin, v. 60, n. 3, p. 515–524, 2016.
- ZHANG, L. et al. Effect of cooling rate on microstructure and properties of microalloyed HSLA steel weld metals. **Science and Technology of Welding and Joining**, Abingdon-on-Thames, v. 20, n. 5, p. 371–377, 2015.
- ZHAO, L. et al. Influence of welding parameters on distribution of wire feeding elements in CO₂ laser GMA hybrid welding. **Science and Technology of Welding and Joining**, Abingdon-on-Thames, v. 14, n. 5, p. 457–467, 2009.
- ZOU, J. L. et al. Experimental and theoretical characterization of deep penetration welding threshold induced by 1- μ m laser. **Applied Surface Science**, Amsterdam, v. 357, p. 1522–1527, 2015.
- ZOU, J. et al. Effect of plume on weld penetration during high-power fiber laser welding. **Journal of Laser Applications**, Orlando, v. 28, n. 2, p. 022003, 2016.